

# **Optically induced orientational transitions in nematic liquid crystals**

Von der Universität Bayreuth  
zur Erlangung des Grades eines  
Doktors der Naturwissenschaften (Dr. rer. nat.)  
genehmigte Abhandlung

vorgelegt von

**Dmitry Krimer**

geboren am 5. January 1975 in Brest, Weissrussland

1. Gutachter: Prof. L. Kramer Ph. D.  
2. Gutachter: Prof. Dr. H. Brand

Tag der Einreichung: 25. Mai 2004  
Tag des Kolloquiums: 15. Juli 2004



# Zusammenfassung

Diese Arbeit behandelt dynamische Phänomene und Orientierungsübergänge, die durch intensives Licht in homeotrop orientierten nematischen Schichten induziert werden. In vielen Experimenten, an solchen Systemen, konnten zahlreiche interessante dynamische Bereiche identifiziert werden. Jedoch wurden nur für einige Fälle systematische Theorien entwickelt, die die beobachteten Phänomene beschreiben können. In anderen Fällen gibt es nur vereinfachte Modelle mit begrenztem Anwendungsbereich.

In Kapitel 2 betrachte ich den Fall einer senkrecht einfallenden, zirkular polarisierten, ebenen Lichtwelle. Ich habe eine Theorie aufgestellt, die die detaillierte Beschreibung der beobachteten Bereiche der Direktordynamik und ihrer Übergänge ermöglicht. Die erste Instabilität ist der Fréederickszübergang vom homeotropen zu einem reorientierten Zustand mit kleiner Amplitude und gleichmäßiger Direktorpräzession um die Schichtnormale. Mit zunehmender Lichtintensität verliert dieser Zustand seine Stabilität in einer superkritischen Hopfbifurkation und eine neue Frequenz tritt im zeitlichen Fourierspektrum auf. Dieses quasiperiodische Regime entspricht einer Kombination aus Präzession und Nutation. Mit weiterer Erhöhung der Intensität verschwindet dieser Zustand bei einem kritischen Wert, bei dem die Nutationsperiode unendlich wird. An diesem Punkt gibt es über eine homokline Bifurkation einen stark hysteretischen Übergang zu einem Zustand mit starker Reorientierung. Der homokline Orbit ist vom einfachsten Typ, bei dem ein Grenzyklus mit einem Sattelpunkt kollidiert, der eine instabile Richtung aufweist. Der neue Zustand entspricht einer gleichmäßigen Präzession des Direktors, nun jedoch mit einer sehr langen Periode und großer Reorientierung. Ich habe auch den Einfluss eines zusätzlichen statischen elektrischen Feldes auf das dynamische Szenario untersucht.

In Kapitel 3 wird die Untersuchung auf elliptisch polarisiertes Licht verallgemeinert. Das vollständige Bifurkationsdiagramm mit Lichtintensität und Elliptizität als Bifurkationsparameter wurde in den Bereichen berechnet, in der der rotierende Zustand existiert. Ich habe gezeigt, daß für einen ziemlich kleinen Bereich der Elliptizität in der Nähe vom zirkularen Fall der erste periodisch rotierende Zustand seine Stabilität in

einer superkritischen Hopfbifurkation verliert. Mit zunehmender Lichtintensität führen bei festgehaltener Elliptizität verschiedene Übergangssequenzen schließlich zu einem Zustand mit großer Direktorreorientierung. Die Natur dieses stark reorientierten Zustandes wie auch die der Zwischenregimes hängt von der Elliptizität ab. Einige dieser Bereiche, die bei geringeren Intensitäten erscheinen, wurden schon früher experimentell und theoretisch untersucht. Eine vollständige Beschreibung, bis hin zum stark reorientierten Regime, stand aber aus.

In der in den obigen Kapiteln entwickelten theoretischen Behandlung, wie auch in allen anderen Studien, wurde das durch die Bewegung des Direktors erzeugte Geschwindigkeitsfeld ("backflow") vernachlässigt. In Kapitel 4 habe ich den Einfluss des backflows auf das in Kapitel 2 beschriebene dynamische Szenario untersucht und dabei substantielle quantitative Änderungen gefunden. Es stellt sich heraus, daß das quasiperiodische Regime zu höheren Lichtintensitäten verschoben wird und außerdem in einem größeren Bereich existiert. Für den Zustand mit großer Direktorreorientierung habe ich eine unerwartete räumliche Oszillation des backflows senkrecht durch die Schicht gefunden. Dies ist eine Folge der Interferenzmuster des Lichts in der Schicht. Tatsächlich werden in der entwickelten Theorie erstmalig lichtinduzierte dynamische Phänomene aus den vollständigen nematodynamischen Gleichungen abgeleitet. Damit könnte man erstmals einen quantitativen Vergleich mit Experimenten mit transversal ausgedehntem Laserstrahl durchführen.

Weiterhin wurde in allen früheren Untersuchungen mit eingestrahltm Licht in Form einer ebenen Welle angenommen, daß die Direktorreorientierung nicht von den Koordinaten parallel zur Schicht abhängt, d.h., man hat ein eindimensionales Problem betrachtet. In Kapitel 5 habe ich die von einer schräg einfallenden, linear polarisierten ordentlichen Welle erzeugten Instabilitäten untersucht unter Zulassung von räumlichen Variationen des Direktors in der Schichtebene und unter Einschluss des Falles eines farbstoffdotierten Nematens. Wie schon vorher bekannt war, verliert der homeotrope Zustand seine Stabilität für ausreichend kleine Einfallswinkel in einer stationären homogenen Pitchforkbifurkation. Ich habe gezeigt, daß der resultierende stationäre reorientierte Zustand seine Stabilität in einer inhomogenen, sekundären Hopfbifurkation mit endlicher kritischer Wellenzahl verliert. Dies führt zur Bildung von laufenden Wellen in der Schichtebene. Ihre Wellenlänge hängt vom Einfallswinkel und dem Verhältnis der elastischen Konstanten ab und ist typischerweise mehrfach größer als die Breite der Schicht.

Abschließend kann gesagt werden, daß, obwohl es systematische Theorien gibt, die qualitative Voraussagen für Experimente machen, es noch an quantitativer Übereinstimmung fehlt. Der wichtigste Grund dafür ist wahrscheinlich, daß die in den Experimenten

benutzte Strahlbreite von der Ordnung der Schichtdicke ist, wohingegen in der theoretischen Behandlung eine unendliche ebene Welle angenommen wird. Also sollte entweder in der Theorie die endliche Ausdehnung des Laserstrahls Berücksichtigung finden oder in den Experimenten sollten transversal ausgedehnte Laser verwendet werden. Ersteres ist schwierig, insbesondere wenn auch noch der backflow einbezogen wird. Für das letztere werden sehr leistungsstarke Laser benötigt, ausser man verwendet geeignet farbstoffdotierte nematische Flüssigkristalle. Ein weiteres interessantes Probleme, das in Zukunft angegangen werden könnte, betrifft den Fall, wo periodisch moduliert wird.



# Contents

<b>1</b>	<b>Introduction</b>	<b>1</b>
1.1	Light induced orientational instabilities in nematics . . . . .	1
1.2	Theoretical model . . . . .	6
1.2.1	Director equations . . . . .	6
1.2.2	Equations for the light propagation . . . . .	7
<b>2</b>	<b>Nonlinear reorientation dynamics induced by circularly polarized light in nematics</b>	<b>11</b>
2.1	Theoretical model . . . . .	11
2.2	Linear stability analysis of the basic state . . . . .	14
2.3	Simulations . . . . .	15
2.4	Classification of the dynamical regimes . . . . .	16
2.5	First regime of uniform director precession . . . . .	19
2.6	Secondary supercritical Hopf bifurcation ( $\rho \simeq \rho_2$ ) . . . . .	23
2.7	Regime of nonuniform director precession . . . . .	26
2.8	Homoclinic bifurcation ( $\rho \simeq \rho_3$ ) . . . . .	30
2.9	Second regime of uniform director precession . . . . .	30
2.10	Approximate model for the uniform precession regimes . . . . .	35
2.11	Additional static fields . . . . .	37
2.12	Discussion . . . . .	39

<b>3</b>	<b>Symmetry breaking effects in reorientation dynamics induced by elliptically polarized light in nematics</b>	<b>43</b>
3.1	Theoretical model . . . . .	43
3.2	Bifurcation scenario . . . . .	44
3.3	Periodic rotating regime . . . . .	50
3.4	Transition from periodic to quasi-periodic rotating regime . . . . .	51
3.5	Quasi-periodic rotating regime . . . . .	54
3.6	Discussion . . . . .	54
<b>4</b>	<b>Influence of the backflow effect on the orientational dynamics in nematics</b>	<b>57</b>
4.1	Basic equations . . . . .	57
4.2	Adiabatic elimination of the flow field . . . . .	58
4.3	Linear stability analysis of the basic state . . . . .	63
4.4	Simulations . . . . .	66
4.5	Discussion . . . . .	68
<b>5</b>	<b>Pattern forming instability induced by light in pure and dye-doped nematics</b>	<b>69</b>
5.1	Basic state . . . . .	69
5.2	Linearization of the equations around the basic state . . . . .	70
5.3	Approximate stability analysis of the basic state . . . . .	73
5.4	The stationary distorted state . . . . .	76
5.5	Stability analysis of the stationary distorted state . . . . .	77
5.6	Heating of the nematic due to the dye . . . . .	86
5.7	Discussion . . . . .	87
	<b>Summary</b>	<b>89</b>
<b>A</b>	<b>Representation of the light propagation in terms of ordinary and extraordinary waves</b>	<b>91</b>

<b>B</b>	<b>Director equations in <math>(\theta, \varphi)</math> representation</b>	<b>97</b>
<b>C</b>	<b>Matrix elements <math>\Lambda_{ij}</math> for the linear stability analysis of the basic state</b>	<b>99</b>
<b>D</b>	<b>Matrix representation for the light propagation (Oldano formalism)</b>	<b>101</b>



# Chapter 1

## Introduction

### 1.1 Light induced orientational instabilities in nematics

Liquid crystals (LCs) demonstrate a rich variety of interesting optical phenomena which have been studied intensively during the last two decades. A nematic LC behaves optically as a uniaxial anisotropic medium with the optical axis along the local molecular orientation described by the director  $\mathbf{n}(\mathbf{r}, t)$  (note that  $\mathbf{n}$  and  $-\mathbf{n}$  are indistinguishable). Moreover, when light propagates through the nematic, its electric field exerts a torque on the molecules which can induce molecular reorientation. The director reorientation leads to a change of the optical properties of the LC and, as a consequence, the light polarization is changed as it propagates through the layer. Such a feedback between the light and the nematic gives rise to interesting nonlinear dynamical phenomena [1,2]. The optical electric field can be written as  $\mathbf{E}_{\text{real}}(\mathbf{r}, t) = 1/2[\mathbf{E}(\mathbf{r}, t)e^{-i\omega t} + \text{c.c.}]$ , where  $\omega$  is the frequency of light and the complex amplitude  $\mathbf{E}(\mathbf{r}, t)$  varies slowly in time on the scale  $1/\omega$ . Averaging over a time that is long compared with the period of the light wave, the optical torque acting on the director can be written as [2]

$$\boldsymbol{\tau} = \frac{\varepsilon_a}{16\pi}(\mathbf{n} \cdot \mathbf{E}^*)(\mathbf{n} \times \mathbf{E}) + \text{c.c.} , \quad (1.1)$$

where  $\varepsilon_a = \varepsilon_{\parallel} - \varepsilon_{\perp}$  is the dielectric anisotropy and  $\varepsilon_{\perp}$  ( $\varepsilon_{\parallel}$ ) is the dielectric permittivity (at optical frequency) perpendicular (parallel) to  $\mathbf{n}$ .

One can distinguish between different cases where the initial torque  $\boldsymbol{\tau}$  is nonzero or zero. This is determined by the mutual alignment of the polarization of the incident light and the initial director orientation (geometry of setup). One can see from Eq.

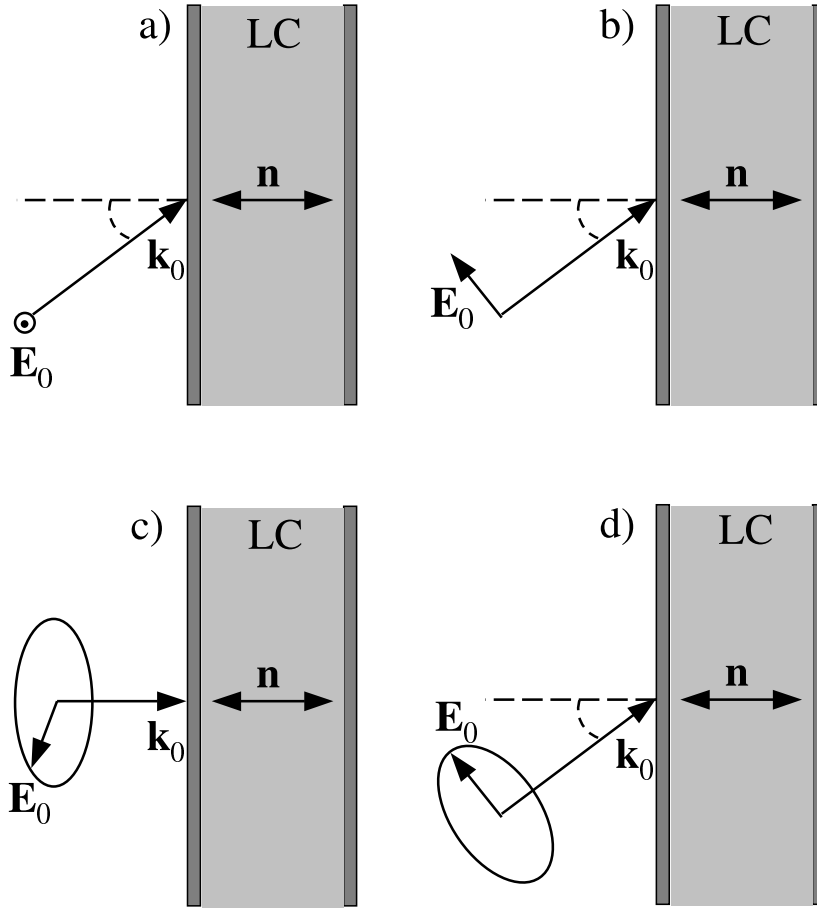


**Figure 1.1.** Different geometries of setups with a threshold [a),c)] and without threshold [b),d)]: a) [ b)]: linearly polarized incident light with ordinary (extraordinary) wave only; c), d): elliptically (or circularly) polarized incident light. The director  $\mathbf{n}$  is perpendicular to the substrates (homeotropic alignment).  $\mathbf{k}_0$  is the incident wavevector.

(1.1) that the initial torque is zero,  $\boldsymbol{\tau} = 0$ , if  $\mathbf{n} \parallel \mathbf{E}$  or  $\mathbf{n} \perp \mathbf{E}$  and, at first sight, it might seem that such a field cannot lead to director reorientation. However, it turns out that above a certain light intensity the initial state can become unstable and due to thermal fluctuations the director reorients. This is the so-called Light Induced Fréedericksz Transition (LIFT). Obviously, if initially  $\boldsymbol{\tau} \neq 0$ , the director will change its initial orientation for any arbitrarily small light intensity and there is no threshold.

In Fig. 1.1 some different geometries of light incident on a nematic layer that has homeotropic alignment (the director is perpendicular to the plane of the layer) are shown. A cell consists of a nematic LC sandwiched between two substrates (typically glass plates). In both cases shown in Fig. 1.1 a), b) the incident light is linearly polarized, but in the first case the polarization is perpendicular to the plane containing the optical axis defined by the director  $\mathbf{n}$  and the wavevector  $\mathbf{k}_0$  (ordinary wave) and

in the second case the polarization lies in this plane (extraordinary wave). In Fig. 1.1 c), d) the light is incident perpendicularly [c)] or at a small oblique angle [d)] on a layer and has circular (or elliptical) polarization. As is seen from Figs. 1.1 a), c) the initial torque  $\boldsymbol{\tau} = 0$  (since  $\mathbf{n} \cdot \mathbf{E} = 0$ ). Thus one may expect a LIFT. In contrast, for the geometries depicted in Figs. 1.1 b), d) the initial torque  $\boldsymbol{\tau} \neq 0$  and thus, there is no LIFT (the director will be distorted for any arbitrary small field). The two geometries depicted in Fig. 1.1a), c) are of particular interest and have been studied very intensively, both experimentally and theoretically. They will be considered at length in this thesis.

In Fig. 1.1c) a circularly polarized light wave incident perpendicularly on a thin layer of nematic LC (with a homeotropic orientation) is shown. This geometry will be considered in **Chapter 2**. In this case the LIFT is observed to be weakly hysteretic, and above threshold the molecules undergo a collective rotation [3] (that corresponds to a uniform precession of the director). This effect is well understood in the frame of a purely classical (hydrodynamic) approach [3]. It also can be interpreted in a quantum picture as spin angular momentum transfer from the light to the medium and is called self-induced stimulated light scattering . Since collective molecular rotation dissipates energy, the light beam has to transmit part of its energy to the medium. As the pure nematic LC is a transparent medium (no absorption) this energy loss leads to a red shift of a part of the light beam [4]. The mechanism can be described as follows: each scattered photon has its helicity reversed and thus transfers an angular momentum of  $2\hbar$  (that is perpendicular to the layer) to the medium. Moreover its energy is lowered by an amount  $\hbar\Delta\omega$ . Thus  $p$  photons per unit time produce a constant torque  $\tau_z = 2\hbar p$ , acting on the medium, which induces a collective molecular precession. This torque is balanced by the viscous torque. The angular velocity of the uniform precession  $\Omega$  is related to a red shift  $\Delta\omega$  by the simple formula  $\Delta\omega = 2\Omega$ . This formula can be derived from energy conservation using that i)  $p$  photons loose per unit time the amount of energy  $\hbar\Delta\omega p$ ; ii) the work made by the torque  $\tau_z$  on the director is  $\tau_z\Omega = 2\hbar p\Omega = \hbar\Delta\omega p$ . The fact that in the final relation  $\hbar$  disappears, shows that one can obtain this formula through a classical approach [5].

In general the angular momentum of the light beam consists of two parts: a spin part associated with polarization [6] and an orbital part associated with spatial distribution [7]. However, if the spatial distribution in the plane of the layer is supposed to be homogeneous i. e. when one deals with a plane wave approximation, as will be done in this thesis, then the orbital part is zero. In this context it may be interesting to note that laser light with a Laguerre-Gaussian amplitude distribution can be shown to have a well-defined orbital momentum [8]. In recent publications the influence of a

finite beam diameter (playing the role of an additional control parameter) [9] and of a nontrivial beam profile [10, 11] were studied. Both of these factors lead to new and distinct regimes of complex behavior.

In [5] a theoretical and experimental investigation of the dynamical behavior of the system for the region of higher intensities was reported. The authors of [5] observed a further discontinuous transition with large hysteresis from a precession regime with small reorientation amplitude occurring above the LIFT to one with large reorientation. The frequency of the large amplitude precession was found to be much smaller than the one just above the LIFT and to exhibit rapid variations with the incident intensity reaching zero at roughly periodic intervals. In this work the authors presented an approximate model that can describe qualitatively both regimes of uniform director precession and also presented clear experimental evidence of the frequency reduction in the second regime. The nature of the transition from one regime to the other was, however, not understood in the framework of this model. More recently, the authors [12, 13], identified experimentally a new continuous transition from the small-amplitude uniform precession state to a more complex state with a precession-nutation type motion of the director. This intermediate regime with a more complex director motion and a sequence of transitions between different regimes will be a subject of **Chapter 2**.

If the incident light is elliptically polarized, the dynamics of the director become even more complex compared to the circular case [14, 15]. It turns out that the regime with a precession-nutation type motion of the director can also be realized in the elliptic case and this is the subject of **Chapter 3**.

A simplification used in all previous theoretical studies is the assumption that the flow velocity  $\mathbf{v}$  in the LC is zero. Actually one has to include the equation for the velocity  $\mathbf{v}$  and consider the coupled director-velocity equations in the framework of the well-established hydrodynamic approach (see e. g. H. Pleiner and H. Brand in [16]). Indeed, director reorientation itself generates flow, even in the absence of external forces acting on  $\mathbf{v}$ . This is the so-called backflow effect. In some simple situations where the director does not deviate strongly from the initial alignment, backflow can be taken into account approximately by renormalization of the rotational viscosity  $\gamma_1$  in the director equations. I will consider the influence of the backflow effect on the director dynamics properly in **Chapter 4**. To our knowledge this is the first time that backflow is explicitly included for a nematic driven by light.

One of the assumptions made in all theoretical models mentioned above is, that the cell is illuminated homogeneously over an area whose linear extension is much larger than

the thickness of the layer. In this case we can also assume that the director depends only on the coordinate across the cell and the light inside the nematic can be treated as a plane wave. However, it is quite difficult to realize such conditions in experiments because one needs powerful lasers, since the LIFT occurs at an intensity level of a few  $kW/cm^2$ . On the other hand, the threshold for the LIFT in *dye-doped* nematic LCs turns out to be up to more than two orders of magnitude lower than in a pure nematic [17]. This allows the spot diameter of the light to be increased and to become much larger than the thickness of the layer. Thus a large aspect ratio system can be realized. Now, the light absorption of the dye becomes significant at optical frequencies, which can lead to considerable heating and even melting of the nematic [18].

The nature of this enormous threshold reduction by doping with dyes was the subject of numerous studies [19–22]. From a macroscopic point of view, the dye leads to an enhancement of the optical torque acting on the molecules that can be written as [compare with Eq. (1.1)]:

$$\boldsymbol{\tau} = \frac{\xi_{eff}}{16\pi} (\mathbf{n} \cdot \mathbf{E}^*) (\mathbf{n} \times \mathbf{E}) + c.c. , \quad (1.2)$$

where  $\xi_{eff} = \varepsilon_a + \zeta$ . Here  $\zeta$  describes phenomenologically the effect of certain dye dopants ( $\xi_{eff} = \varepsilon_a$  in a pure LC) and can be both positive and negative depending on dye concentration, molecular structures of both host and dye materials, on the wavelength of light, and on temperature [19,22]. The microscopic origin of the enhancement is not yet completely clarified. A model has been proposed in [22].

The dye-doped case is emphasized when studying in **Chapter 5** the geometry where a linearly polarized ordinary light wave is incident at a small oblique angle on a thin layer of homeotropically oriented nematic LC [see Fig. 1.1a)]. In this case the LIFT can be shown to be continuous [23,24]. With further increase of the intensity, periodic and irregular motion of the director was found in early experiments [25–27]. Subsequent experiments were devoted to an exploration of this irregular regime [27–32]. Observations show that the initial oscillations grow and become more complex as the intensity of the incident light increases, eventually turning chaotic [27,29,31]. A theoretical model involving a few discrete reorientation modes actually predicts a complex route to chaos via gluing bifurcations [33,34]. Clear experimental evidence for the occurrence of the first gluing bifurcation was presented in [35,36]. In these theoretical studies all dynamical quantities were assumed to be spatially independent along the layer plane. However, since our system is spatially extended in the plane of the layer and has broken reflection symmetry one actually expects the appearance of travelling waves that alter the bifurcation scenario. This problem is studied in **Chapter 5** with special emphasis on the dye-doped case.

## 1.2 Theoretical model

### 1.2.1 Director equations

The director equations for the steady state can be derived using the variational principle according to which the free energy has a minimum at equilibrium with respect to all variations of the director  $\mathbf{n}$ . When the transient behavior is studied then the equations for the director are obtained using the fact that the dissipation is equal to the decrease in free energy [37].

We consider strong anchoring of the nematic at the boundaries (i. e. the orientation of the director is fixed at the boundaries). Since we deal with light the magnetic anisotropy can be neglected. Thus the expression for the density of the free energy of the dye-doped nematic LC consists only of elastic and electrical parts:

$$F = \frac{K_1}{2} (\nabla \cdot \mathbf{n})^2 + \frac{K_2}{2} (\mathbf{n} \cdot \nabla \times \mathbf{n})^2 + \frac{K_3}{2} (\mathbf{n} \times \nabla \times \mathbf{n})^2 - \frac{\xi_{eff}}{16\pi} |\mathbf{n} \cdot \mathbf{E}|^2, \quad (1.3)$$

where  $K_1$ ,  $K_2$ ,  $K_3$  are respectively the splay, twist and bend elastic constants of the LC [37].  $\xi_{eff}$  is the same enhancement factor that appears in the optical torque acting on the director due to dye dopants [see Eq. (1.2)]. Note that  $\xi_{eff} = \varepsilon_a$  in pure LC. In the absence of a velocity field the dynamical equations of motion for the director are given by:

$$\gamma_1 \partial_t \mathbf{n} = -\underline{\underline{\delta}}^\perp \mathbf{h}, \quad (1.4)$$

where  $\gamma_1$  is a rotational viscosity and  $\mathbf{h}$  is the molecular field obtained by calculating the variational derivatives of the free energy density  $F$ :

$$h_i = \frac{\delta F}{\delta n_i} = \frac{\partial F}{\partial n_i} - \partial_j \left( \frac{\partial F}{\partial n_{i,j}} \right), \quad i = x, y, z. \quad (1.5)$$

It should be noted that the variational derivatives are carried out by considering the electric field  $\mathbf{E}$  as fixed. Since the relation  $\mathbf{n}^2 = 1$  has to be fulfilled at all times, the molecular field has to be projected onto the plane perpendicular to the director by using of  $\delta_{ij}^\perp = \delta_{ij} - n_i n_j$  introduced in Eq. (1.4). Eqs. (1.4) can also be interpreted as a torque balance among the elastic, electric and viscous torques [1].

We consider a plane wave incident perpendicularly or at a small oblique angle  $\beta_0$  on a layer of pure or dye-doped nematic LC which has initially homeotropic alignment [see Fig. 1.1a),c)]. We choose the Cartesian coordinates in such a way that  $(\mathbf{x}, \mathbf{y})$  lies in the plane of the layer and  $\mathbf{z}$  is perpendicular to it. We first assume that the director

components depend only on  $z, t$ . In this case the partial differential equations for  $n_x$  and  $n_y$  following from Eq. (1.4) have the form:

$$\begin{aligned} \gamma_1 \partial_t n_x &= (K_2 n_y^2 + K_3 n_z^2) [\partial_z^2 n_x + 2n_x (\partial_z n_x)^2] - n_x [K_2 n_y \partial_z^2 n_y + K_1 n_z \partial_z^2 n_z] + \\ &2n_x [K_3 n_z^2 - K_2 (1 - n_x^2)] (\partial_z n_y)^2 + 2n_y [K_2 (1 - 2n_x^2) \partial_z n_x - K_3 n_x n_z \partial_z n_z] \partial_z n_y + \\ &2K_3 n_z (1 - n_x^2) \partial_z n_x \partial_z n_z + \frac{\xi_{eff}}{16\pi} \{ 2n_x [(1 - n_x^2) E_x E_x^* - n_y n_z (E_y^* E_z + E_y E_z^*)] + \\ &(1 - 2n_x^2) [n_y (E_x^* E_y + E_x E_y^*) + n_z (E_x^* E_z + E_x E_z^*)] - 2n_x (n_y^2 E_y E_y^* + n_z^2 E_z E_z^*) \} , \end{aligned} \quad (1.6)$$

$$\begin{aligned} \gamma_1 \partial_t n_y &= (K_2 n_x^2 + K_3 n_z^2) [\partial_z^2 n_y + 2n_y (\partial_z n_y)^2] - n_y [K_2 n_x \partial_z^2 n_x + K_1 n_z \partial_z^2 n_z] + \\ &2n_y [K_3 n_z^2 - K_2 (1 - n_y^2)] (\partial_z n_x)^2 + 2n_x [K_2 (1 - 2n_y^2) \partial_z n_y - K_3 n_y n_z \partial_z n_z] \partial_z n_x + \\ &2K_3 n_z (1 - n_y^2) \partial_z n_y \partial_z n_z + \frac{\xi_{eff}}{16\pi} \{ 2n_y [(1 - n_y^2) E_y E_y^* - n_x n_z (E_x^* E_z + E_x E_z^*)] + \\ &(1 - 2n_y^2) [n_x (E_x^* E_y + E_x E_y^*) + n_z (E_y^* E_z + E_y E_z^*)] - 2n_y (n_x^2 E_x E_x^* + n_z^2 E_z E_z^*) \} . \end{aligned} \quad (1.7)$$

Note that the equation for  $n_y$  can be obtained from the one for  $n_x$  by interchanging the indices  $x$  and  $y$ . The  $z$  component of the director  $n_z$  can then be obtained from the condition  $\mathbf{n}^2 = 1$ . The strong homeotropic anchoring at the boundaries yield the following conditions:

$$n_x(0) = n_x(L) = n_y(0) = n_y(L) = 0. \quad (1.8)$$

## 1.2.2 Equations for the light propagation

In order to solve Eqs. (1.6,1.7) for the director we have to determine the electric field which is governed by Maxwell's equations. These equations contain the dielectric permittivity tensor which depends on the director components. It should be noted that the characteristic time of the director motion is many orders of magnitude longer than the period of the light wave ( $\sim 10^{15} - 10^{16}$ ). This fact allows one to consider the instantaneous profile of the director as constant with respect to the light.

Maxwell's equations can be written for a nonmagnetic material in the absence of any currents and charges as:

$$\nabla \times \mathbf{H} = \frac{1}{c} \frac{\partial \mathbf{E}}{\partial t}, \quad \nabla \cdot (\underline{\underline{\varepsilon}} \mathbf{E}) = 0 \quad (1.9)$$

$$\nabla \times \mathbf{E} = -\frac{1}{c} \frac{\partial \mathbf{H}}{\partial t}, \quad \nabla \cdot \mathbf{H} = 0 \quad (1.10)$$

with the complex dielectric tensor

$$\varepsilon_{ij} = (\varepsilon_{\perp} + i\gamma_{\perp}) \delta_{ij} + (\varepsilon_a + i\gamma_a) n_i n_j, \quad (1.11)$$

where  $\varepsilon_a = \varepsilon_{\parallel} - \varepsilon_{\perp}$  is the real part of the dielectric anisotropy and  $\varepsilon_{\perp}$  ( $\varepsilon_{\parallel}$ ) is the dielectric permittivity (at optical frequency) perpendicular (parallel) to  $\mathbf{n}$ .

In Eq. (1.11)  $\gamma_a = \gamma_{\parallel} - \gamma_{\perp}$ , where  $\gamma_{\perp}$  and  $\gamma_{\parallel}$  are the imaginary parts of the dielectric permittivity for  $\mathbf{E}$  perpendicular and parallel to  $\mathbf{n}$ , respectively. They are usually negligible in pure LCs and describe the absorption effect by the dye.

We assume that the diameter of the laser beam is much larger than the thickness of the layer and consider the case when the director depends only on  $z, t$ . This means that also the components of the dielectric tensor depend only on  $z$  and the light inside the nematic can be treated as a plane wave. We write the electric and magnetic fields in the form:

$$\begin{aligned} \mathbf{E}(\mathbf{r}, t) &= \frac{1}{2} (\mathbf{E}(z, t) e^{i(k_x x + k_y y)} e^{-i\omega t} + c.c.), \\ \mathbf{H}(\mathbf{r}, t) &= \frac{1}{2} (\mathbf{H}(z, t) e^{i(k_x x + k_y y)} e^{-i\omega t} + c.c.) \end{aligned} \quad (1.12)$$

and choose the  $(\mathbf{x}, \mathbf{z})$  plane as the plane of incidence (it contains the surface normal and the incident wavevector). Thus we have for the components of the wavevector  $k_x, k_y$ :

$$k_x = s_0 k_0, \quad k_y = 0, \quad (1.13)$$

where  $k_0 = \omega/c$  is the wavenumber in vacuum and  $s_0 = \sin(\beta_0)$  with  $\beta_0$  the angle of incidence. Note that  $\mathbf{E}(z, t), \mathbf{H}(z, t)$  in (1.12) are complex amplitudes which vary slowly in time compared to  $\omega^{-1}$ , as a result of slow director motion. Eventually the first equation (1.9) becomes:

$$\begin{pmatrix} 0 & -\partial_z & 0 \\ \partial_z & 0 & -ik_x \\ 0 & ik_x & 0 \end{pmatrix} \begin{pmatrix} H_x \\ H_y \\ H_z \end{pmatrix} = -i \frac{\omega}{c} \underline{\underline{\varepsilon}} \begin{pmatrix} E_x \\ E_y \\ E_z \end{pmatrix}. \quad (1.14)$$

Analogously for the first equation (1.10):

$$\begin{pmatrix} 0 & -\partial_z & 0 \\ \partial_z & 0 & -ik_x \\ 0 & ik_x & 0 \end{pmatrix} \begin{pmatrix} E_x \\ E_y \\ E_z \end{pmatrix} = i\frac{\omega}{c} \begin{pmatrix} H_x \\ H_y \\ H_z \end{pmatrix}. \quad (1.15)$$

$H_z$  and  $E_z$  can be straightforwardly expressed by the other components using the last equation given by Eqs. (1.14) and Eqs. (1.15):

$$H_z = s_0 E_y, \quad E_z = -\frac{s_0}{\varepsilon_{zz}} H_y - \frac{\varepsilon_{xz}}{\varepsilon_{zz}} E_x - \frac{\varepsilon_{yz}}{\varepsilon_{zz}} E_y. \quad (1.16)$$

It can now be shown that the divergence equations in Eqs. (1.9) and Eqs. (1.10) are automatically fulfilled.

Finally, Eq. (1.16) is used in Eqs. (1.14,1.15) to write the differential equations for the other components of the fields in the so-called Berreman formalism [38]:

$$\frac{d\bar{\Psi}}{dz} = ik_0 D \bar{\Psi}, \quad (1.17)$$

where

$$\bar{\Psi} = \begin{pmatrix} E_x \\ H_y \\ E_y \\ -H_x \end{pmatrix} \quad (1.18)$$

and

$$D = \begin{pmatrix} -\frac{\varepsilon_{xz}s_0}{\varepsilon_{zz}} & 1 - \frac{s_0^2}{\varepsilon_{zz}} & -\frac{\varepsilon_{yz}s_0}{\varepsilon_{zz}} & 0 \\ \varepsilon_{xx} - \frac{\varepsilon_{xz}^2}{\varepsilon_{zz}} & -\frac{\varepsilon_{xz}s_0}{\varepsilon_{zz}} & \varepsilon_{xy} - \frac{\varepsilon_{xz}\varepsilon_{yz}}{\varepsilon_{zz}} & 0 \\ 0 & 0 & 0 & 1 \\ \varepsilon_{xy} - \frac{\varepsilon_{xz}\varepsilon_{yz}}{\varepsilon_{zz}} & -\frac{\varepsilon_{yz}s_0}{\varepsilon_{zz}} & \varepsilon_{yy} - \frac{\varepsilon_{yz}^2}{\varepsilon_{zz}} - s_0^2 & 0 \end{pmatrix}. \quad (1.19)$$

The experimentally measurable ordinary and extraordinary indices  $n_o, n_e$  and absorption coefficients  $\alpha_o, \alpha_e$  are related with the dielectric permittivities in Eq. (1.11) as follows (see also Appendix A):

$$n_o = \text{Re}\sqrt{\varepsilon_{\perp} + i\gamma_{\perp}}, \quad n_e = \text{Re}\sqrt{\varepsilon_{\parallel} + i\gamma_{\parallel}} \quad (1.20)$$

$$\alpha_{\perp} = 2k_0 \text{Im}\sqrt{\varepsilon_{\perp} + i\gamma_{\perp}}, \quad \alpha_{\parallel} = 2k_0 \text{Im}\sqrt{\varepsilon_{\parallel} + i\gamma_{\parallel}}.$$

Assuming that  $\gamma_{\perp}/\varepsilon_{\perp}, \gamma_{\parallel}/\varepsilon_{\parallel} \ll 1$  and neglecting the terms of the order of  $(\gamma_{\perp}/\varepsilon_{\perp})^2, (\gamma_{\parallel}/\varepsilon_{\parallel})^2$  the following inverse relations can be obtained:

$$\varepsilon_{\perp} = n_o^2, \varepsilon_a = n_e^2 - n_o^2, \gamma_{\perp} = \frac{\alpha_{\perp} n_o}{k_0}, \gamma_a = \frac{\alpha_{\parallel} n_e - \alpha_{\perp} n_o}{k_0}. \quad (1.21)$$

Finally we have a set of four first-order ordinary differential equations (ODEs) Eqs. (1.17) for the light propagation inside the LC that are equivalent to a set of two second-order ODEs for the components of the electric field  $E_x, E_y$ . The initial conditions at  $z = 0$  are defined by the intensity and polarization of the incident light.

# Chapter 2

## Nonlinear reorientation dynamics induced by circularly polarized light in nematics

The reorientation dynamics of a homeotropically aligned nematic liquid crystal film excited by a circularly polarized beam at normal incidence is investigated with the intensity of the incident light regarded as the control parameter. The secondary instability above the optical Fréedericksz transition threshold is shown to be a supercritical Hopf bifurcation leading to quasi-periodicity while the discontinuous transition from the quasi-periodic regime to a uniform precession regime with large reorientation is identified as a homoclinic bifurcation.

### 2.1 Theoretical model

We consider a circularly polarized plane wave incident perpendicularly on a layer of nematic LC that has initially homeotropic alignment (with strong homeotropic anchoring at the boundaries). The light is polarized in the plane of the layer [the  $(\mathbf{x}, \mathbf{y})$  plane] and propagates along the positive  $\mathbf{z}$ -axis (see Fig. 2.1). We assume that the diameter of the laser beam is much larger than the thickness of the layer, and consider the case when the director depends only on  $z, t$ . Then the light inside the nematic can be treated as a plane wave. We introduce the spherical angles  $\Theta(z, t)$  and  $\Phi(z, t)$  to describe the director

$$\mathbf{n} = (\sin \Theta \cos \Phi, \sin \Theta \sin \Phi, \cos \Theta). \quad (2.1)$$

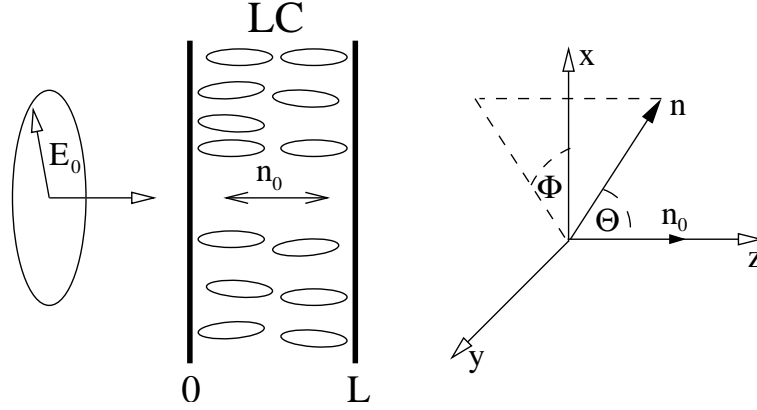


**Figure 2.1.** Geometry of the setup: circularly polarized light incident perpendicularly on a nematic layer with the director  $\mathbf{n}_0 \parallel \mathbf{z}$  (homeotropic state). The components of the director  $\mathbf{n}$  are described in terms of the angles  $\Theta, \Phi$  ( $\Theta = 0$  in the homeotropic state).

To obtain the electric field, we use the approach when the light propagation inside LC is described in terms of ordinary and extraordinary waves (see Appendix A). In this case the electric field is governed by Eqs. (A.15) for the amplitudes  $A_o, A_e$  that are related with  $E_x, E_y$  by (A.19). Note that Eqs. (A.15) remain unchanged after introducing the dimensionless length  $z \rightarrow z\pi/L$  except  $k_0$  is transformed to dimensionless wavevector  $k_0 \rightarrow k_0L/\pi$ .

The boundary conditions for the amplitudes  $A_o, A_e$  (normalized to the amplitude of the incoming light) at  $z = 0$  are given by Eqs. (A.17) when substituting  $\chi = \pi/4$  (circular polarization):

$$|A_{e0}|^2 = |A_{o0}|^2 = \frac{1}{2}, \quad A_{e0}A_{o0}^* = -\frac{i}{2}. \quad (2.2)$$

We introduce the phase delay induced by the nematic up to a certain distance:

$$\alpha(z) = k_0 \int_0^z (\sqrt{\lambda_e} - \sqrt{\lambda_o}) dz \equiv k_0 \sqrt{\varepsilon_\perp} \int_0^z \left[ \sqrt{\frac{(\varepsilon_a + \varepsilon_\perp)}{\varepsilon_\perp + \varepsilon_a \cos^2 \Theta}} - 1 \right] dz \quad (2.3)$$

and the phase delay induced by the whole layer  $\Delta \equiv \alpha(z = \pi)$  defined in normalized  $z$  [see Eqs. (A.10,A.16)]. As is seen from (2.3)  $\Delta$  depends on  $\Theta$  only. Note that  $\Delta$  has a direct experimental interpretation since the quantity  $\Delta/2\pi$  represents roughly the number of self diffraction rings in the far field [24].

We may substitute now the expression of the director (2.1) into Eqs. (1.6,1.7) to derive a set of two PDEs in terms of  $\Theta$  and  $\Phi$ . At this step it is convenient to separate the time derivatives on  $\Theta$  and  $\Phi$  that appear in these equations. Multiplying the equation that comes from Eq. (1.6) by  $\cos \Phi$  and that from Eq. (1.7) by  $\sin \Phi$  and then adding

them the PDE for  $\Theta$  can be derived. In order to get the PDE for  $\Phi$  one has to multiply Eq. (1.7) by  $\cos \Phi$  and Eq. (1.6) by  $\sin \Phi$  and then subtract them. We then introduce the amplitudes  $A_o, A_e$  and the phase factor  $\alpha(z)$  into the electric terms of the equations according to Eqs. (A.19) and also make use of Eq. (A.5). Finally the equations for  $\Theta$  and  $\Phi$  are given by:

$$\begin{cases} \partial_t \Phi = \mathcal{L}_\Phi \\ \partial_t \Theta = \mathcal{L}_\Theta \end{cases} \quad (2.4)$$

with

$$\begin{aligned} \mathcal{L}_\Phi &= \frac{1}{\sin^2 \Theta} \frac{\partial}{\partial z} [(1 - (1 - k_2) \sin^2 \Theta) \sin^2 \Theta \partial_z \Phi] + 2\rho \frac{\lambda_e}{\lambda_o} \text{Re} [A_e A_o^* e^{i\alpha(z)}] \\ \mathcal{L}_\Theta &= (1 - (1 - k_1) \sin^2 \Theta) \partial_z^2 \Theta - \end{aligned} \quad (2.5)$$

$$\frac{\sin 2\Theta}{2} [(1 - k_1)(\partial_z \Theta)^2 + (1 - 2(1 - k_2) \sin^2 \Theta) (\partial_z \Phi)^2 - 2\rho \left(\frac{\lambda_e}{\lambda_o}\right)^2 |A_e|^2],$$

where  $k_1 = K_1/K_3$  and  $k_2 = K_2/K_3$ . In Eq. (2.4), time  $t$  is normalized to the characteristic relaxation time  $\tau$  of the director and  $\rho = I/I_c$  is the dimensionless incident light intensity, with

$$\tau = \frac{\gamma_1 L^2}{\pi^2 K_3}, \quad I_c = \frac{2\pi^2 c(\varepsilon_\perp + \varepsilon_a) K_3}{L^2 \varepsilon_a \sqrt{\varepsilon_\perp}}, \quad (2.6)$$

where  $\gamma_1$  is the rotational viscosity<sup>1</sup> and  $c$  is the velocity of light in vacuum. It will be demonstrated in Sec. 2.2 that  $I_c$  has a meaning of the threshold intensity of the light induced Fréedericksz transition (LIFT) for circularly polarized light at perpendicular incidence. Note that in this case the homeotropic state loses its stability at an intensity two times higher than that for linearly polarized light.

Alternatively, Eqs. (2.4) can be obtained by direct substitution of the representation (2.1) into the free energy (1.3) and taking the variational derivatives with respect to  $\Theta$  and  $\Phi$ . In that case the projection operator will not be needed in Eq. (1.4).

The boundary conditions for  $\Theta$  and  $\Phi$  are (strong homeotropic anchoring):

$$\partial_z \Phi_{z=0,\pi}(t) = 0, \quad \Theta_{z=0,\pi}(t) = 0. \quad (2.7)$$

It should be noted that the coupled director and field equations (2.4), (A.15) together with the boundary conditions (2.2), (2.7) are invariant with respect to rotations around

---

<sup>1</sup>In a more elaborate treatment the velocity field has to be included, see Chapter 4.

the  $z$ -axis, namely to the change

$$\Phi \rightarrow \Phi + \delta\Phi \quad (2.8)$$

as a consequence of isotropy in  $(x, y)$  plane.

## 2.2 Linear stability analysis of the basic state

We performed a linear stability analysis around the homeotropic state for which  $\Theta = 0$  and  $\Phi$  is some undefined constant.  $\Phi$  is undefined because in this representation  $\partial_z\Phi$  is zero at the boundaries [see Eqs. (2.7)] but not the angle itself. When the light propagates through the LC its polarization remains unchanged and the phase delay  $\Delta$  induced by the layer is zero. The amplitudes  $A_o$ ,  $A_e$  coincide with the boundary conditions (2.2).

We linearize the equation for  $\Theta$  [see Eqs. (2.4)] around the homeotropic state. Straightforward calculations give:

$$\partial_t\Theta = \partial_z^2\Theta + 2\rho\Theta|A_{e0}|^2 \equiv \partial_z^2\Theta + \rho\Theta. \quad (2.9)$$

We look for solutions satisfying the boundary conditions  $\Theta|_{z=0,\pi} = 0$  in the form

$$\Theta(z, t) = \sum_{n=1} \Theta_n e^{\sigma_n t} \sin nz \quad (2.10)$$

and get the classical result for the growth rate  $\tilde{\sigma}_n = \sigma_n/\tau$

$$\tilde{\sigma}_n = \frac{\rho - n^2}{\tau}. \quad (2.11)$$

One can make two important conclusions from Eq. (2.11), namely i) the damping factor is  $\tau$ ; ii) if the field overcomes the value  $\rho = 1$  the homeotropic state becomes unstable.

The angle  $\Phi$  is of arbitrary value for the homeotropic state and, as a consequence, drops out from the equation for  $\Theta$  in linear approximation.

## 2.3 Simulations

We may expand  $\Theta$  and  $\Phi$  with respect to  $z$  in systems of orthogonal functions which satisfy the boundary conditions (2.7):

$$\begin{aligned}\Theta &= \sum_{n=1}^{\infty} \Theta_n(t) V_n(z) \\ \Phi &\equiv \Phi_0(t) + \Phi_d(z, t) = \Phi_0(t) + \sum_{n=1}^{\infty} \Phi_n(t) U_n(\cos z),\end{aligned}\tag{2.12}$$

where  $V_n(z)$  and  $U_n(\cos z)$  are the Chebyshev polynomials of the second kind [39]

$$V_n(z) = \sin nz, \quad U_n(\cos z) = \frac{\sin(n+1)z}{\sin z}\tag{2.13}$$

and are normalized as:

$$\int_0^{\pi} dz V_m(z) V_n(z) = \int_0^{\pi} dz U_m(\cos z) U_n(\cos z) \sin^2 z = \frac{\pi}{2} \delta_{mn}.\tag{2.14}$$

The zeroth mode  $\Phi_0(t)$  in Eq. (2.12) does not depend on  $z$  and describes a pure rotation of the director (without elastic distortion) around the  $z$ -axis while  $\Phi_d(z, t)$  corresponds to the twist distortion. After substituting the expansions (2.12) into Eqs. (2.4) and projecting on the modes of expansion (Galerkin method), a set of coupled nonlinear ODEs for the modes  $\Theta_n(t), \Phi_n(t)$  is obtained:

$$\begin{cases} \frac{d\Phi_n}{dt} = \mathcal{G}_n(\Theta_1, \Theta_2, \dots; \Phi_1, \Phi_2, \dots), \\ \frac{d\Theta_n}{dt} = \mathcal{F}_n(\Theta_1, \Theta_2, \dots; \Phi_1, \Phi_2, \dots) \end{cases} \quad n = 1, 2, \dots\tag{2.15}$$

As a result of isotropy, the ODE for  $\Phi_0(t)$  is decoupled from the rest and from the boundary conditions Eqs. (2.2), (2.7) [only  $\partial_z \Phi$  appears in these equations]:

$$\frac{d\Phi_0}{dt} = \mathcal{G}_0(\Theta_1, \Theta_2, \dots; \Phi_1, \Phi_2, \dots).\tag{2.16}$$

The infinite set of ODEs given by Eqs. (2.15) is reduced to a finite one by truncating the mode expansion for  $\Theta$  and  $\Phi$ . We then solved it using the standard Runge-Kutta method and chose the number of modes such that the accuracy of the calculated director components was better than 1%. Note that the ODEs for  $A_o, A_e$  [see Eqs. (A.15)] have to be solved dynamically at each step of numerical integration for time  $t$ .

When  $\Theta_n$  and  $\Phi_n$  do not depend on  $t$  [ $d\Phi_n/dt = d\Theta_n/dt = 0$ ], the angular velocity  $d\Phi_0/dt$  has a constant value and the director precesses uniformly around the  $z$ -axis with a frequency  $f_0$  defined as

$$f_0 = \frac{1}{2\pi} \frac{d\Phi_0}{dt}. \quad (2.17)$$

In this case, the problem is significantly simplified. In fact, instead of solving a system of evolution equations for  $\Phi_n(t)$  and  $\Theta_n(t)$ , we are now faced with a set of nonlinear algebraic equations. After solving them numerically and substituting  $\Phi_n$  and  $\Theta_n$  into Eq. (2.16), the frequency  $f_0$  of the uniform precession can be found.

The preceding discussion holds only for circularly polarized light since for an elliptically polarized light the rotational invariance given by Eq. (2.8) is broken. This however considerably enriches the dynamics [14, 15, 40].

In the calculations, we used the material parameters for the nematic *E7* (at room temperature):  $K_1 = 11.09 \times 10^{-7}$  dyn,  $K_2 = 5.82 \times 10^{-7}$  dyn,  $K_3 = 15.97 \times 10^{-7}$  dyn [15],  $n_e = 1.746$ ,  $n_o = 1.522$  [41] (refractive indices of the ordinary and extraordinary light, respectively),  $\lambda = 532$  nm (wavelength of laser),  $\gamma_1/K_3 = 10^6$  s cm $^{-2}$  [42]. The calculations were made for a layer of 100  $\mu$ m thickness. For these parameters  $I_c \simeq 2.6$  kW/cm $^2$ ,  $\tau \simeq 10$  s.

## 2.4 Classification of the dynamical regimes

This section gives a brief overview of the dynamical regimes occurring in the system, and they will be discussed in detail in subsequent sections. In Fig. 2.2, the phase delay  $\Delta/2\pi$  (a measure of the amplitude of reorientation) is plotted versus the normalized intensity  $\rho$ . The solid lines represent stable uniform precession (UP) states, i.e.  $f_0 = \text{const}$  [see Eq. (2.17)], while the dashed lines correspond to precession states that are unstable. The region in gray corresponds to a nonuniform precession (NUP) where nutation ( $d\Delta/dt \neq 0$ ) is coupled to precession. In this regime, the lower and the upper lines that define the region in gray correspond to the minimum and maximum values taken by  $\Delta$  during its oscillation.

The optical Fréedericksz transition occurs at  $\rho = 1$  where the system settles to a uniform precession state with a small reorientation amplitude ( $\Delta \sim \pi$  or equivalently  $\Theta^2 \ll 1$ ) labeled UP1. Decreasing the intensity from the UP1 regime, the system switches back to the unperturbed state at  $\rho = \rho_1^* \simeq 0.88$ . When the intensity is increased above the LIFT threshold, the UP1 loses its stability at  $\rho = \rho_2 \simeq 1.45$

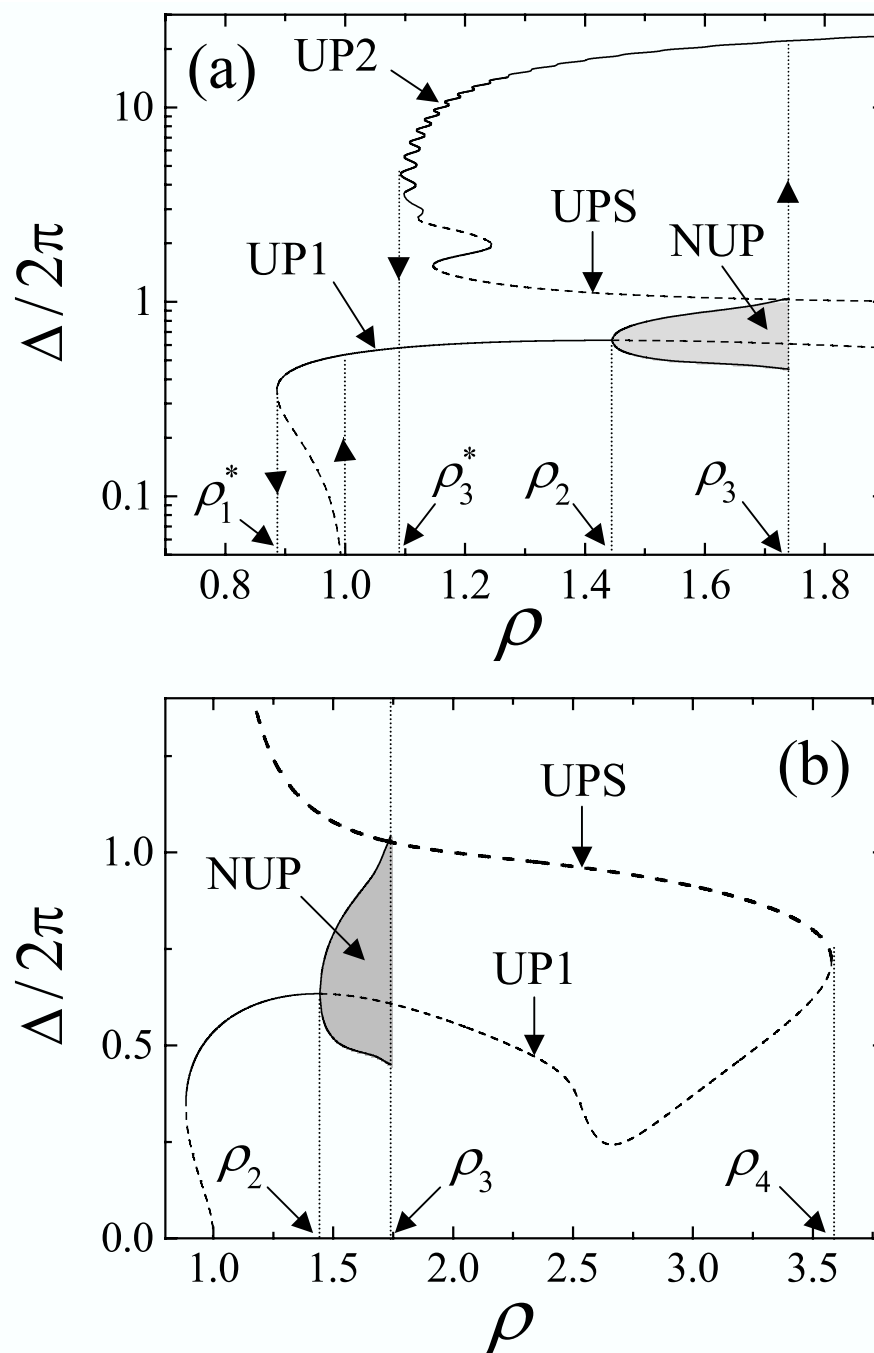


**Figure 2.2.** (a)  $\Delta/2\pi$  versus  $\rho$  in a logarithmic scale for  $\rho < 2$  and  $\Delta < 50\pi$ . (b)  $\Delta/2\pi$  versus  $\rho$  in a linear scale for  $\rho < 4$  and  $\Delta < 3\pi$ . Solid (dashed) curves correspond to stable (unstable) solutions.

**Table 2.1.** Calculated values of the thresholds  $\rho_2$  versus modes number  $N_\Theta$  and  $M_\Phi$ .

	$N_\Theta = 1$	$N_\Theta = 2$	$N_\Theta = 3$	$N_\Theta = 4$	$N_\Theta = 5$
$M_\Phi = 1$	—	—	—	—	—
$M_\Phi = 2$	—	—	—	—	1.52
$M_\Phi = 3$	1.66	—	1.46	1.46	1.45
$M_\Phi = 4$	1.63	—	1.45	1.45	1.45
$M_\Phi = 5$	1.63	—	1.45	1.45	1.45

**Table 2.2.** Calculated values of the thresholds  $\rho_3$  versus modes number  $N_\Theta$  and  $M_\Phi$ .

	$N_\Theta = 1$	$N_\Theta = 2$	$N_\Theta = 3$	$N_\Theta = 4$	$N_\Theta = 5$
$M_\Phi = 1$	—	—	—	—	—
$M_\Phi = 2$	—	—	—	—	2.35
$M_\Phi = 3$	2.07	—	1.76	1.78	1.77
$M_\Phi = 4$	2.07	—	1.75	1.79	1.77
$M_\Phi = 5$	2.02	—	1.74	1.77	1.75

where the NUP regime takes over. Subsequently the NUP state loses stability at  $\rho = \rho_3 \simeq 1.75$  where the system abruptly switches to a uniform precession with a large reorientation amplitude ( $\Delta \gg 1$  or equivalently  $\Theta^2 \sim 1$ ) labeled UP2. Decreasing the intensity in the UP2 regime, the system switches back to the UP1 regime at  $\rho = \rho_3^* \simeq 1.09$ . From Fig. 2.2 b), which shows the entire UP1 regime, we see that the unstable branch makes a loop and connects with the other unstable uniform precession branch, which we will call UPS and which is connected with UP2. Thus, for  $\rho > \rho_4 \simeq 3.58$  one is left with only UP2.

For different orders of expansion  $(N_\Theta, M_\Phi)$ , we have calculated the threshold for the continuous transition  $\rho = \rho_2$  where nutation appears ( $\partial_t \Theta \neq 0$ ), and the threshold for the discontinuous transition  $\rho = \rho_3$  where the system abruptly bifurcates towards a large reorientation regime (see Sec. 2.9). The corresponding calculations are summarized in Tables 2.1 and 2.2 for different numbers of modes  $(N_\Theta, M_\Phi)$ . The values for  $\rho_2$  and  $\rho_3$  converge as  $N_\Theta$  and  $M_\Phi$  become large enough. An empty entry indicates that the transition is missing in the bifurcation scenario calculated with  $(N_\Theta, M_\Phi)$ . One can see that it is enough to retain only a few modes for each pair of angles to describe the sequence of bifurcations accurately. All the calculations have been done with six modes for both angles  $\Theta$  and  $\Phi$ .

A comparison between theory and experiment will be presented in the next sections<sup>2</sup>. In the experiment the total intensity of the central part of the beam emerging from the sample,  $I_{\text{center}}$ , and the intensities corresponding to the vertical and horizontal components of the electric field,  $I_x$  and  $I_y$  ( $I_{\text{center}} = I_x + I_y$ ) were measured [43]. As explained in Ref. [9], the behavior of the signal  $I_{\text{center}}(t)$  is qualitatively similar to that of the phase delay  $\Delta(t)$  [see Eq. (2.3)] whereas the behavior of the signal  $i_x(t) \equiv I_x/I_{\text{center}}$  and  $i_y(t) \equiv I_y/I_{\text{center}}$  can be compared to that of the calculated intensity of the  $x$  and  $y$ -component of the electric field of the light at the output of the sample,  $I_x(t) = |E_x(z = L, t)|^2$  and  $I_y(t) = |E_y(z = L, t)|^2$  respectively. Since  $i_x(t) = 1 - i_y(t)$  these time series possess the same dynamical information and we shall refer to any of these quantities as  $i(t)$ .

## 2.5 First regime of uniform director precession

As demonstrated in [3] the homeotropic state remains stable when the incident light intensity is below some critical value ( $\rho_1 = 1$  in normalized units). Above the threshold  $\rho_1$  the director starts to precess uniformly with a frequency  $f_0$  [see Eq. (2.17)] around the  $z$ -axis (UP1). The trajectory in the  $(n_x, n_y)$  plane is a circle. In a coordinate system that rotates with frequency  $f_0$  around the  $z$  axis the trajectory in the  $(n_x, n_y)$  plane is just a fixed point. The frequency of precession  $f_0$  is approximately defined by Eq. (2.27) (see also [5]).

As is seen from Fig. 2.3 at  $\rho = \rho_1$  we deal with a discontinuous transition via subcritical Hopf bifurcation with hysteresis. If one starts from the UP1 state and the intensity  $\rho$  is decreased, the director switches back to the homeotropic state at  $\rho_1^* \approx 0.88$  where a saddle-node bifurcation occurs.

The time Fourier spectra of  $n_x(t)$  and of the oscillating part of the output intensity  $I_x(t)$  have one fundamental frequency,  $f_0$  and  $2f_0$  respectively. The double frequency arises because the angle  $\Phi$  enters quadratically into the expressions for  $|E_{x,y}|^2$  [see Eqs. (A.19)].  $\Theta_n$ ,  $\Phi_n$  and  $\Delta$  are constant and do not depend on time.

Figure 2.4 shows the director dynamics in the UP1 regime, when  $\rho_1 < \rho < \rho_2$ . In agreement with theory (right part of Fig. 2.4), the director precesses uniformly around the  $z$ -axis at frequency  $f_0$ . This is indicated by a quasi-sinusoidal behavior of  $i(t)$  together with a quasi-constant  $I_{\text{center}}$  (left part of Fig. 2.4).

---

<sup>2</sup>The experimental data was provided by E. Brasselet et al.

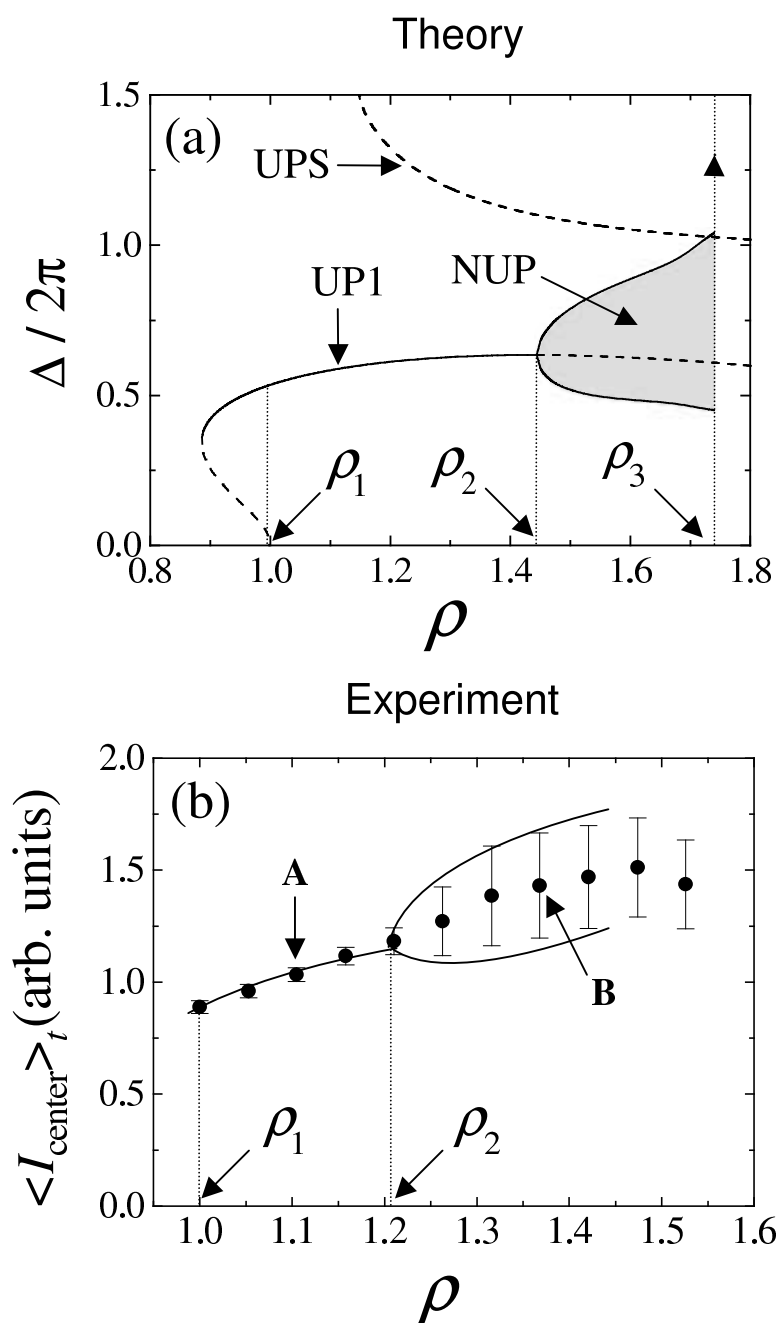


**Figure 2.3.** (a): calculated  $\Delta(\rho)$  ( $\Delta < 3\pi$ ). (b): experimental  $\langle I_{\text{center}}(\rho) \rangle_t$  ( $\bullet$ ). The vertical bars are the standard deviation of  $I_{\text{center}}(t)$  for the corresponding value of  $\rho$  and the solid line is to guide the eye of the extrema of  $I_{\text{center}}(t)$ . The points labeled A and B are also included in Fig. 2.5. They correspond to the time series in Figs. 2.4 and 2.11.

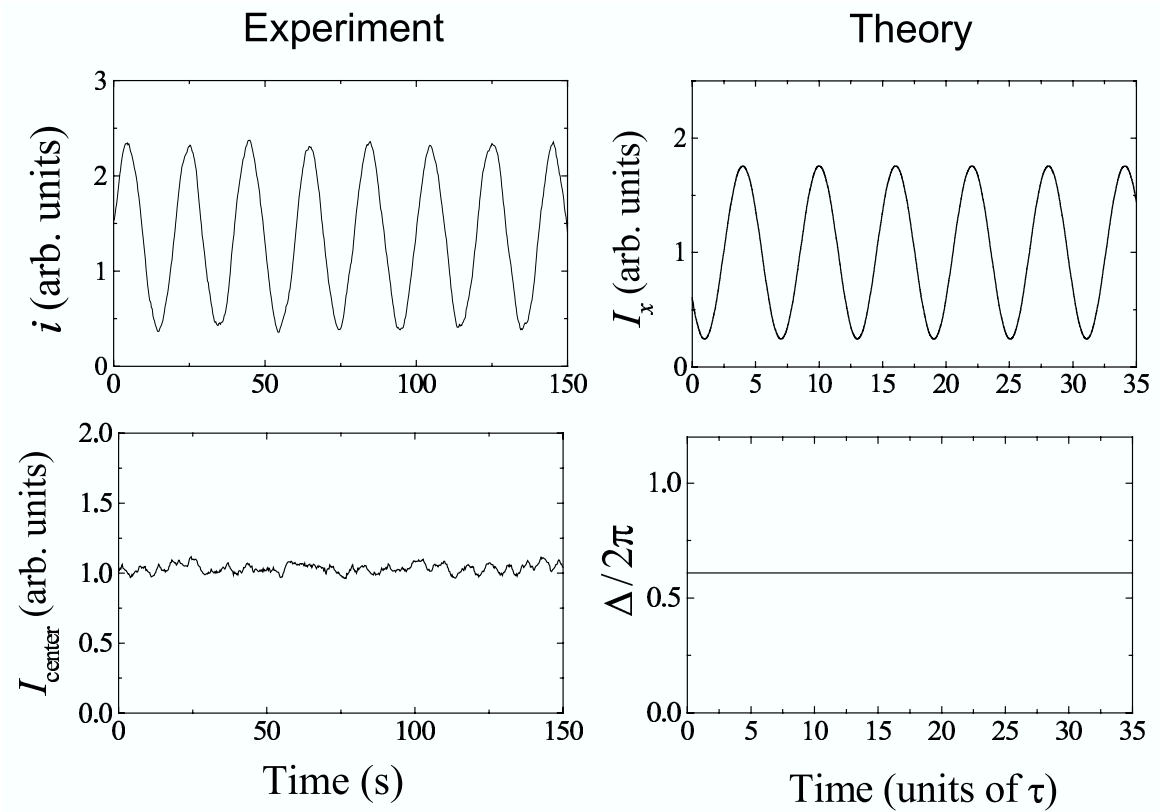


**Figure 2.4.** Director dynamics in the UP1 regime. Left part: experimental  $i(t)$  and  $I_{\text{center}}(t)$  for  $\rho = 1.10$ , which corresponds to point A in Figs. 2.3 and 2.5. Right part: calculated  $I_x(t)$  and  $\Delta(t)/2\pi$  for  $\rho = 1.20$ .

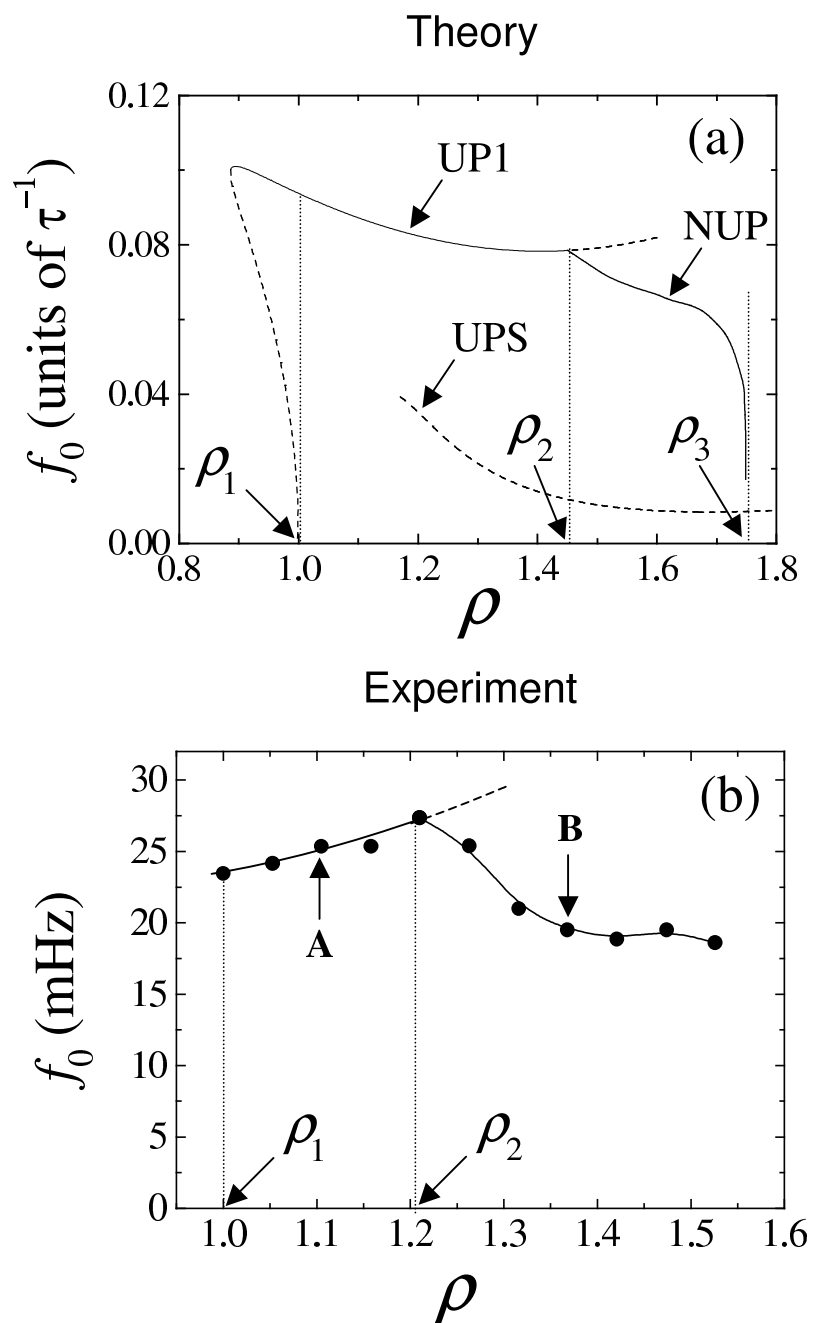


**Figure 2.5.** Precession frequency  $f_0(\rho)$  versus  $\rho$ .

(a): theory.

(b): experiment ( $\bullet$ ). The solid line is to guide the eye. The points labeled A and B correspond to the time series in Figs. 2.4 and 2.11.

A point of disagreement is that theory predicts a deceleration of the precession as  $\rho$  increases from  $\rho_1$  to  $\rho_2$  [Fig. 2.5(a)] whereas an acceleration is observed experimentally [Fig. 2.5(b)]. This behavior has already been noted in Ref. [44] and attributed to the finite size of the excitation beam: the present aspect ratio is  $\delta = 2w_0/L = 0.4$  (where  $2w_0$  is the beam diameter). For higher values of  $\delta$ , the deceleration behavior predicted by the infinite plane wave theory was in fact observed, as shown in Ref. [5] for  $\delta = 2$  and  $\delta = 3$ . In fact,  $\delta \simeq 2$  has been demonstrated to be a critical value for the aspect ratio of the laser beam in another context where the excitation light is linearly polarized at normal incidence [45].

## 2.6 Secondary supercritical Hopf bifurcation ( $\rho \simeq \rho_2$ )

It was recently observed in experiments that for at a certain intensity  $\rho_2$  the UP1 state loses its stability: the director motion then becomes a nonuniform precession with a new frequency labeled  $f_1$ , associated with nutation [9, 46]. The second order nature of the transition has already been identified experimentally [9, 13, 43] and theoretically [43, 46].

As a result of the appearance of the new frequency  $f_1$  at  $\rho = \rho_2$ , the director motion becomes quasi-periodic characterized by the two frequencies  $f_0$  and  $f_1$ . This is illustrated in Fig. 2.6(a) where the trajectory of the director in the  $(n_x, n_y)$  plane is plotted for  $\rho = 1.55$  at  $z = L/2 - \ell$  ( $\ell \neq 0$ ). The reason for this somewhat arbitrary choice is to have contributions from all polar modes since by construction the even modes  $\Theta_n \sin(n\pi z/L)$  are zero at the center of the cell ( $z = L/2$ ). This trajectory is not closed in the laboratory frame indicating quasi-periodicity of the director. In fact, the two independent motions, namely the precession ( $f_0$ ) and the nutation ( $f_1$ ) can be isolated by transforming to a frame that rotates with frequency  $f_0$ . The director components  $(n_x^{\text{rot}}, n_y^{\text{rot}})$  in this rotating frame are connected with those in the laboratory frame by

$$n_x^{\text{rot}} = n_y \sin(2\pi f_0 t) + n_x \cos(2\pi f_0 t), \quad (2.18)$$

$$n_y^{\text{rot}} = n_y \cos(2\pi f_0 t) - n_x \sin(2\pi f_0 t). \quad (2.19)$$

In the rotating frame, the director performs a simple periodic motion with frequency  $f_1$  as is seen in Fig. 2.6(b) with the arrow indicating the sense of rotation for the case where the incident light is left circularly polarized. As will be argued below this sense of rotation is always opposite to that of the underlying precession.

As depicted in Figs. 2.2(b),2.3(a), the dashed line starting at  $\rho = \rho_2$  is unstable. In other words, starting from initial conditions not too far from the UP1 state at some value of  $\rho$  inside the NUP regime, the system eventually settles on the NUP solution. This is illustrated in Fig. 2.6(c,d) (for  $\rho = 1.55$ ) where the trajectory of the director in the rotating frame is shown. Note that the precession frequency  $f_0$  for the NUP solution depends on  $\rho$  and differs from that of the (unstable) UP1 or UPS solutions (see Fig. 2.5). In this frame, the director trajectory of the UP1 and UPS states are circles, i.e. they are periodic motions with the frequency difference (see the dashed lines and the arrows in Fig. 2.6(c,d)). From Fig. 2.6(c) we see that starting from initial conditions near the UP1 solution, the director eventually settles on the NUP solution, which is represented by a simple limit cycle. A similar process starting from an appropriate initial condition near the UPS solution is shown in Fig. 2.6(d). The difference from the previous case is that here one finds initial conditions (near UPS) which lead to the largely-reoriented UP2 state. In fact, the unstable UPS branch represents the saddle point (or separatrix) that separates the regions of attraction of the NUP state (or, below  $\rho_2$ , the UP1 state) from that of the largely-reoriented UP2 state. At this point it might also be interesting to note that the UP1 state represents a stable node at  $\rho \sim \rho_1$  (the relevant stability exponents are real and negative). Then, between  $\rho_1$  and  $\rho_2$  it changes to a focus (the stability exponents become complex). At  $\rho_2$  the real part of the complex pair of stability exponents passes through zero and then becomes positive. The sense of rotation of the NUP loop [Fig. 2.6(b)] is fixed by the tendency towards smaller precession rate when  $\Theta$  increases. Thus, whenever  $\Theta$  is small  $\partial_t \Phi$  is large, resulting in a sense of rotation opposite to that of the precession.

In order to demonstrate unambiguously the nature of the bifurcation at  $\rho = \rho_2$ , we have verified two scaling properties. First we have checked that the amplitude of the limit cycle,  $\mathcal{A}$ , satisfies the scaling law  $\mathcal{A}(\rho) - \mathcal{A}(\rho_2) = \mathcal{O}(\rho - \rho_2)^{1/2}$  in the neighborhood of the bifurcation point. For this purpose, we defined theoretically this amplitude as  $\mathcal{A}_{\text{theory}} = \max |\mathbf{n}_\perp| - \min |\mathbf{n}_\perp|$  where  $\mathbf{n}_\perp = n_x \mathbf{e}_x + n_y \mathbf{e}_y$  is the projection of  $\mathbf{n}$  onto the plane of the layer. The experimental observable is chosen to be  $\mathcal{A}_{\text{exp}} = \text{SD}(I_{\text{center}})$ , where  $\text{SD}(X)$  accounts for standard deviation of the time series  $X(t)$ <sup>3</sup>. Clearly  $\mathcal{A}_{\text{theory}} \neq 0$  and  $\mathcal{A}_{\text{exp}} \neq 0$  only in the presence of nutation. The results are shown in Fig. 2.7 where  $\mathcal{A}_{\text{exp}}$  is plotted versus  $\rho$  in Fig. 2.7(a) (filled circles) and  $\mathcal{A}_{\text{theory}}$  is shown in Fig. 2.7(b) (solid line). The experimental data are fitted by  $\mathcal{A}_{\text{exp}}(\rho) - \mathcal{A}_{\text{exp}}(\rho_2) = \mathcal{O}(\rho - \rho_2)^\gamma$  using the four points in the range  $1.2 < \rho < 1.4$  and taking  $\mathcal{A}_{\text{exp}}(\rho_2)$  as the averaged value of  $\mathcal{A}_{\text{exp}}$  for  $\rho < 1.2$ . We found  $\gamma = 0.46 \pm 0.08$  (dashed line) and  $\rho_2 = 1.208 \pm 0.001$ . On the other hand we obtain  $\gamma = 1/2$  from the theory. Second, we have checked that

<sup>3</sup>The experimental data was provided by E. Brasselet et al.

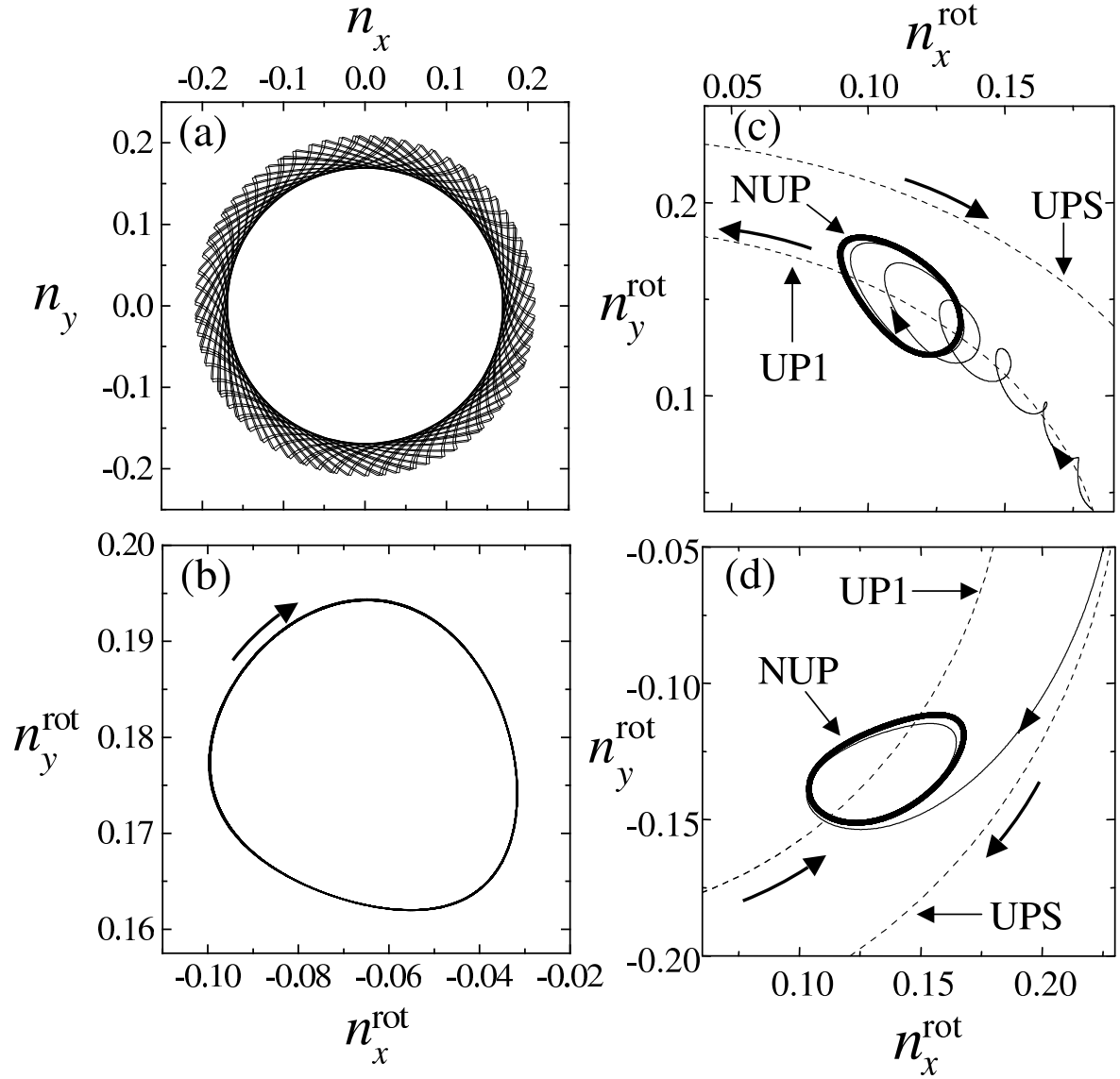


**Figure 2.6.** (a),(b): director trajectory at  $\rho = 1.55$ . (a) Quasiperiodic behavior in the laboratory frame  $(n_x, n_y)$ . (b) Periodic limit cycle in the rotating frame  $(n_x^{\text{rot}}, n_y^{\text{rot}})$ . The arrow indicates the sense of rotation when the incident light is left circularly polarized. (c),(d): director trajectory at  $\rho = 1.55$  in the  $f_0(\rho, \text{NUP})$ -rotating frame showing the instability of the UP1 and UPS solutions in the NUP regime. (c) Initial condition near the UP1 solution. (d) Initial condition near the UPS solution. The arrows indicate the sense of rotation of the corresponding trajectory when the incident light is left circularly polarized.

the frequency  $f_1$  satisfies the scaling law  $f_1(\rho) - f_1(\rho_2) = \mathcal{O}(\rho - \rho_2)$  as displayed in Fig. 2.8 where dashed lines are linear fits. In conclusion, all these results confirm that a *supercritical Hopf bifurcation* occurs at  $\rho = \rho_2$ .

The transition UP1  $\rightarrow$  NUP is associated with a sudden change of slope of the precession frequency versus intensity, as predicted by theory [see Fig. 2.5(a)]. This is related with a fact, that in the NUP regime, the phase shift  $\Delta$  has values closer to  $2\pi$  as  $\rho$  increases [see Fig. 2.3(a)], thus according to an approximate formula Eq. (2.27) (see Sec. 2.10)  $f_0$  decreases.

## 2.7 Regime of nonuniform director precession

In the NUP regime all modes  $\Theta_n$  and  $\Phi_n$  with  $n \geq 1$  are time dependent and the Fourier spectrum of their oscillating part contains frequencies  $mf_1$ , where  $m$  is an integer. The spectra of the phase delay  $\Delta$ , director components  $n_{x,y}$  and the output intensities  $I_{x,y}$  have peaks at frequencies given by the simple formulas:

$$\begin{aligned}\tilde{\Delta} &= \{mf_1\}, \\ \tilde{n}_{x,y} &= \{f_0, mf_1 \pm f_0\}, \\ \tilde{I}_{x,y} &= \{2f_0, mf_1 \pm 2f_0\}.\end{aligned}\tag{2.20}$$

Such predictions agree with the experimental observations reported in Ref. [9]. As an example in Fig. 2.9 the power spectra of the phase delay  $\Delta$  and output intensities  $I_{x,y}$  for  $\rho = 1.50$  are depicted. The exact nature of the spectra (i.e. the importance of each harmonic) depends on the incident intensity and for the purpose of demonstration, we quantified the importance of a certain frequency component  $f^*$  in the power spectrum of  $\Delta$  by taking the corresponding amplitude and dividing it by the largest one at  $f = f_1$ . The results are displayed in Fig. 2.10 for a few harmonics. Starting from  $W_{f^*} = 0$  at the bifurcation point  $\rho = \rho_2$ , these functions increase as  $\rho$  is increased. Nevertheless one can see that the amplitudes of the peaks decay quite fast with increasing  $m$ . Far above  $\rho = \rho_2$ , the director motion is thus no longer qualitatively similar to a quasi-uniform precession, as illustrated in Fig. 2.11. In this figure, the experimental  $i(t)$  and  $I_{\text{center}}(t)$  are presented for  $\rho = 1.37$  on the left and the calculated  $I_x(t)$  and  $\Delta(t)$  for  $\rho = 1.70$  are presented on the right.

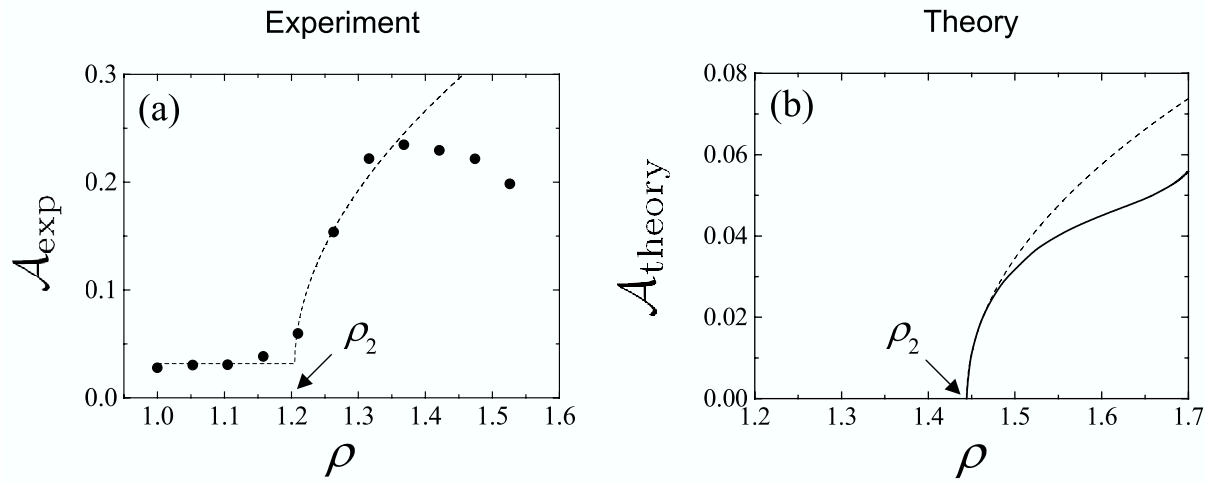


**Figure 2.7.** Scaling law for the amplitude  $\mathcal{A}$  of the limit cycle born at the transition  $\text{UP1} \rightarrow \text{NUP}$ . Left part: experimental data ( $\bullet$ ) fitted by  $(\rho - \rho_2)^\gamma$  near  $\rho_2$ , whose best fit gives  $\gamma = 0.46 \pm 0.08$ . Right part: theory (solid line) where the best fit (dashed line) gives  $\gamma = 1/2$ . See the text for details.

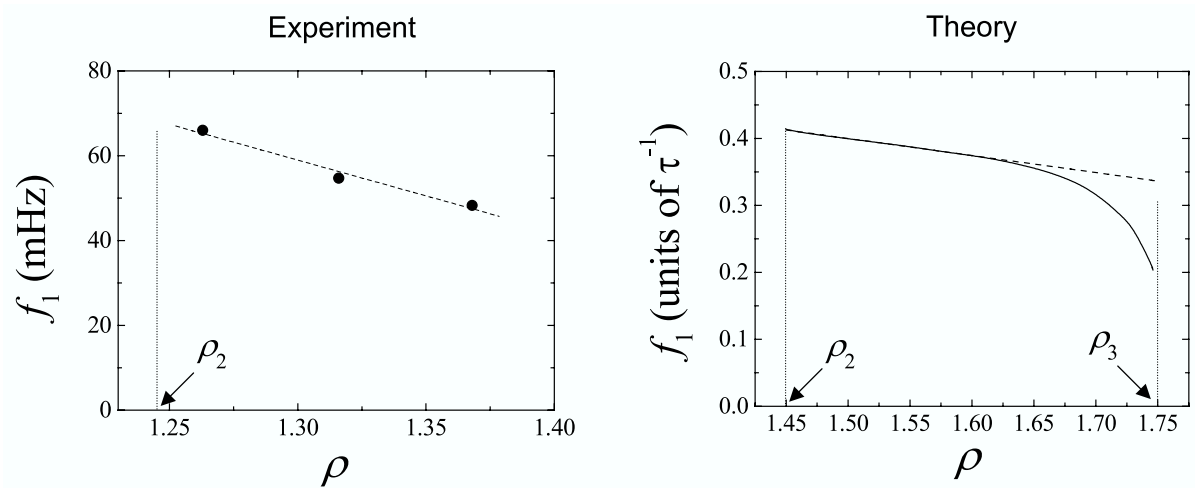


**Figure 2.8.** Scaling law for the frequency of the limit cycle born through the transition  $\text{UP1} \rightarrow \text{NUP}$ . Left part: experiment ( $\bullet$ ) with linear fit (dashed line). Right part: theory (solid line) with linear fit (dashed line).

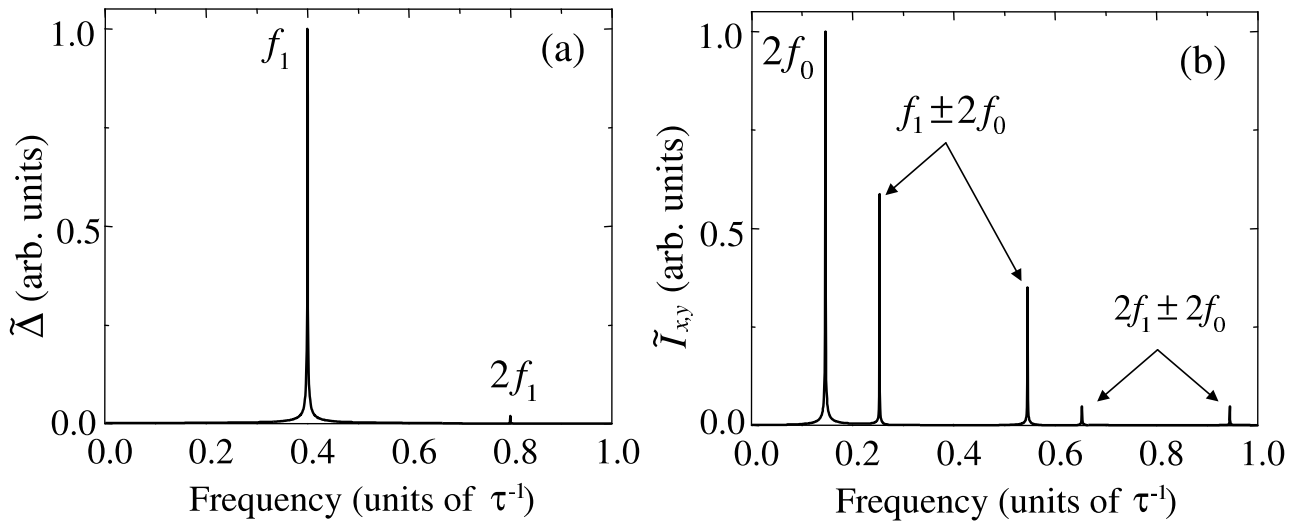


**Figure 2.9.** Calculated power spectra  $\tilde{\Delta}$  and  $\tilde{I}_{x,y}$  for  $\rho = 1.50$ .

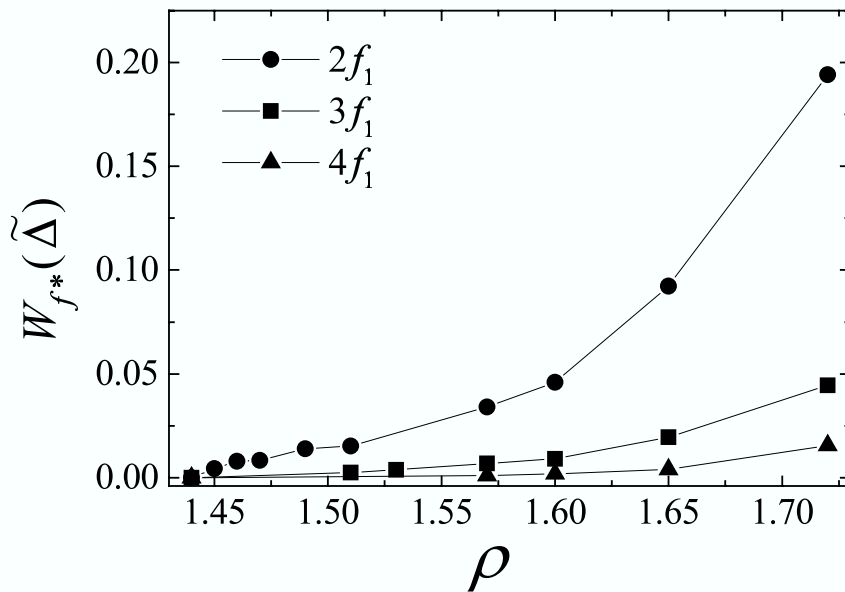


**Figure 2.10.** Characterization of the dynamics in the NUP regime ( $\rho_2 < \rho < \rho_3$ ): Amplitudes  $W_{f^*}(\tilde{\Delta})$  of the power spectrum of  $\Delta$  divided by the amplitude at  $f = f_1$  versus  $\rho$ .

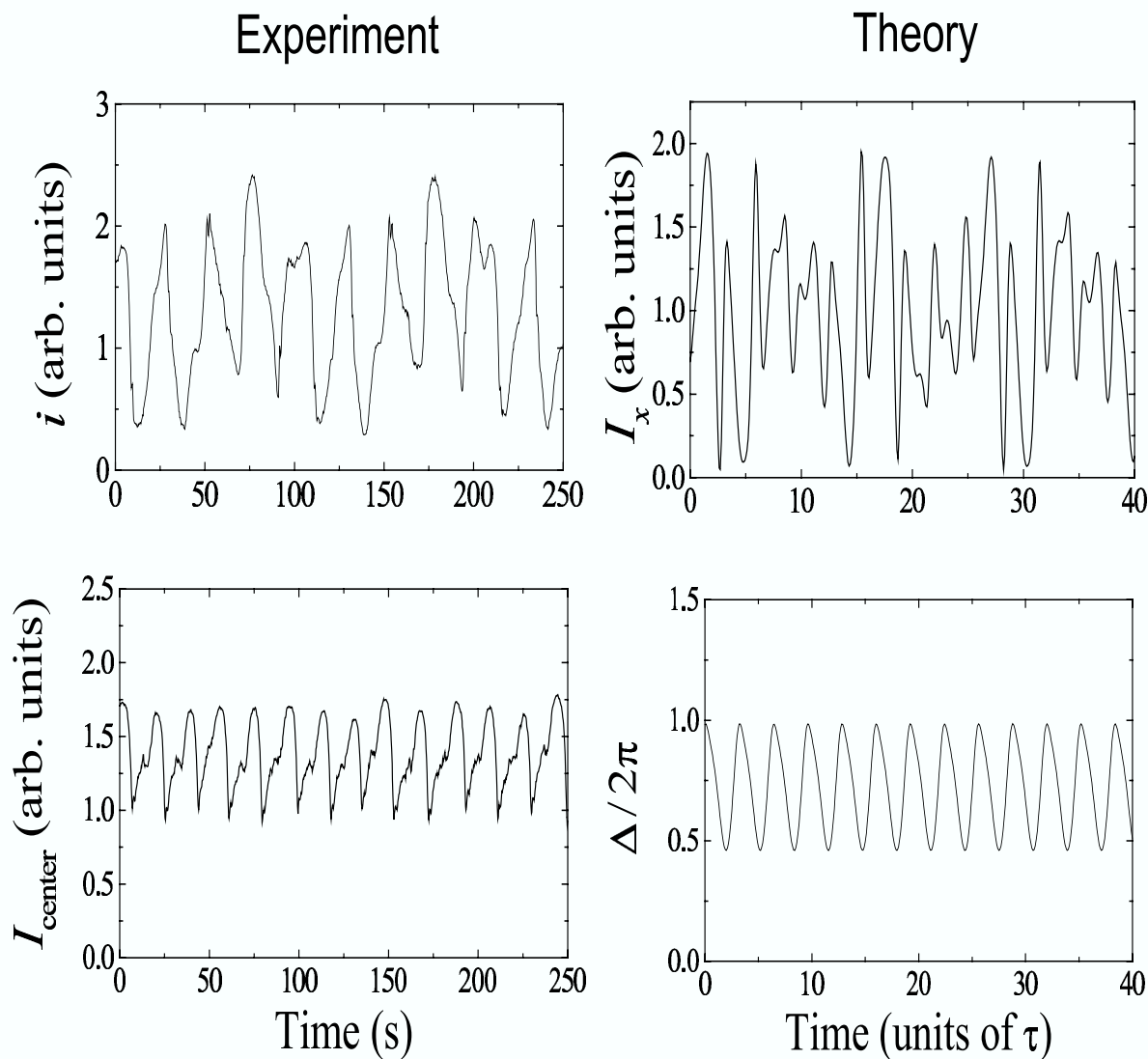


**Figure 2.11.** Dynamics in the NUP regime. Left part: experimental  $i(t)$  and  $I_{\text{center}}(t)$  for  $\rho = 1.37$ , which corresponds to point B in Figs. 2.3 and 2.5. Right part: calculated  $I_x(t)$  and  $\Delta(t)/2\pi$  for  $\rho = 1.70$ .

## 2.8 Homoclinic bifurcation ( $\rho \simeq \rho_3$ )

In some narrow region around  $\rho_3 \approx 1.75$  the period  $T = 1/f_1$  of the NUP increases progressively with increasing light intensity. Indeed, this period appears to diverge at  $\rho_3 \approx 1.75$ , as shown in Fig. 2.12. We found that this divergence is logarithmic, by fitting the calculated values to the function  $a + b \ln(\rho_3 - \rho)$ . The best fit is represented by the solid line in Fig. 2.12 which corresponds to  $a = 1.249$  and  $b = -0.612$ . The nature of the singularity at  $\rho = \rho_3$  signifies that the discontinuous transition  $\text{NUP} \rightarrow \text{UP2}$  [see Fig. 2.2(a)] has the character of a *homoclinic bifurcation* [47].

As  $\rho$  approaches the homoclinic bifurcation point, the trajectory of the director approaches the unstable UPS orbit for longer and longer intervals. This is demonstrated in Fig. 2.13 where the director trajectory is plotted in the  $(n_x, n_y)$  plane for  $\rho = 1.748542389055$ . The system moves very close to the unstable UPS limit cycle, represented by the dashed line [see Figs. 2.2 and 2.13]. As seen, the motion near  $\rho_3$  possesses two time scales, a slow one and a fast one, as expected from the homoclinic nature of the transition. Figure 2.14 emphasizes this point where the phase shift  $\Delta(t)$  and the instantaneous angular velocity  $\Omega(t) = d\Phi_0/dt$  are plotted versus time. When  $\Delta \simeq 2\pi$ , the angular velocity has some constant value, more than one order of magnitude smaller than the value reached when  $\Delta \simeq \pi$ . Taking into account that the total angular momentum transferred to the nematic by a photon is  $(1 - \cos \Delta)\hbar$ , the slow regime is interpreted as a situation where there is almost no net angular momentum transfer while the fast regime corresponds to quasi-optimal transfer.

At  $\rho = \rho_3$  the system jumps to a new state of uniform precession of the director (UP2) with large reorientation ( $\Theta \simeq 74^\circ$ ) and slow precession rate.

## 2.9 Second regime of uniform director precession

Figure Fig. 2.15 shows the typical director dynamics in the UP2 regime, when  $\rho > \rho_3$ . As predicted by theory (right part of Fig. 2.15), the director precesses uniformly around the  $z$ -axis at frequency  $f_0$ : one observes a quasi-sinusoidal  $i(t)$  together with a quasi-constant  $I_{\text{center}}$  (left part of Fig. 2.15). In this case, the frequency  $f_0$  is smaller than the one of the UP1 regime by more than one order of magnitude [compare the time scales of Figs. 2.4 and 2.15].

As displayed in Fig. 2.2(a), starting from the stable UP2 branch above  $\rho_3$  and lowering the excitation intensity, one finds a large and rather complicated hysteretic cycle, which

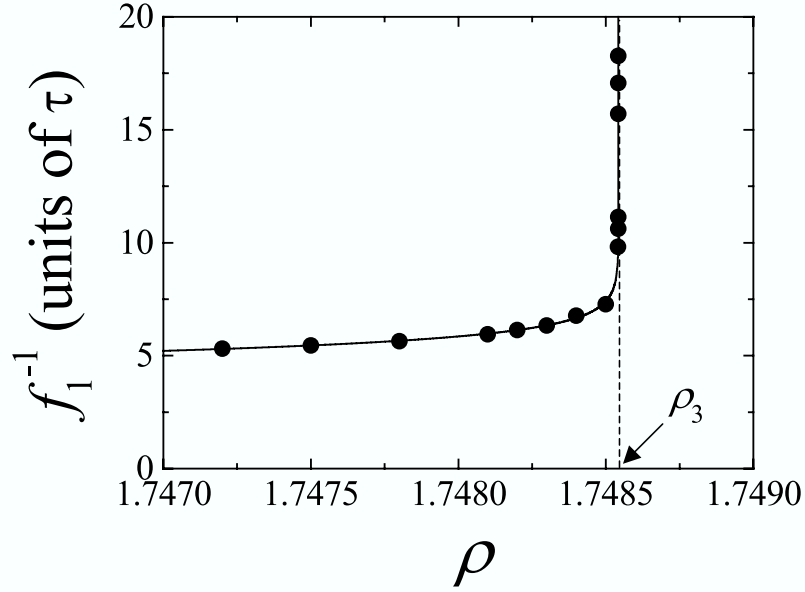


**Figure 2.12.** Characterization of the homoclinic bifurcation  $f_1^{-1}(\rho) = \mathcal{O}[\ln(\rho_3 - \rho)]$  near  $\rho_3$ . The solid line is the best fit to the theoretically calculated values ( $\bullet$ ).

eventually leads to a jump back to the UP1 solution at  $\rho_3^* = 1.09$ . This part of the UP2 branch consists of alternatively stable and unstable regions exhibiting a series of *saddle-node bifurcations*. This result was already obtained in the framework of an approximate model [5] (see also the next section).

Finally, it is instructive to plot the precession frequency  $f_0$  as a function of  $\rho$  for different regimes with uniform precession of the director. The result is shown in Fig. 2.16 where  $f_0$  is plotted versus  $\rho$ , both for the UP1, UPS and UP2 regimes. Note the different scales. The solid lines refer to stable limit cycles and dashed lines to unstable ones. One can see that in the UP2 regime the frequency of precession  $f_0$  is zero for some isolated values of the light intensity. Then the limit cycle in the  $(n_x, n_y)$  plane degenerates to a continuum of fixed points on a circle, a situation where the total angular momentum transfer from the light to the nematic is zero.

Recall that for the UP1 and NUP states  $\Delta$  is always smaller than  $2\pi$ , whereas for the stable UP2 states the values of  $\Delta$  are always large (basically many times  $2\pi$ ). Thus for the UP2 states the phase factor  $\alpha(z)$  [see Eq. (2.3)] varies rapidly across the layer from zero to  $\Delta$ , which leads to a rapidly oscillating torque term  $\mathcal{L}_\Phi$ , see Eq. (2.5). As a result the director twist  $\partial_z \Phi$  exhibits rapid spatial oscillations [see also Eq. (2.28)]. This effect becomes strongly visible in the backflow as discussed in Chapter 4.

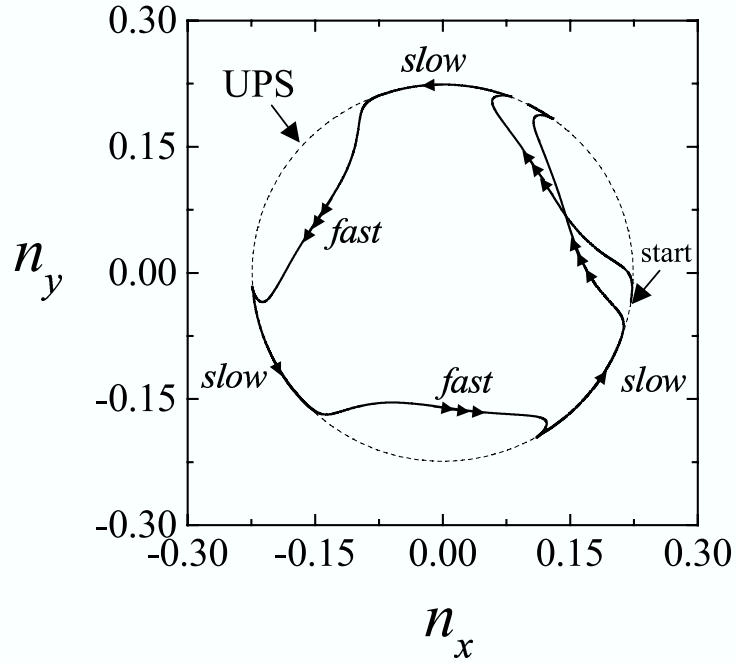


**Figure 2.13.** Calculated director trajectory in the  $(n_x, n_y)$  plane near  $\rho_3$  ( $\rho = 1.748542389055$ ).

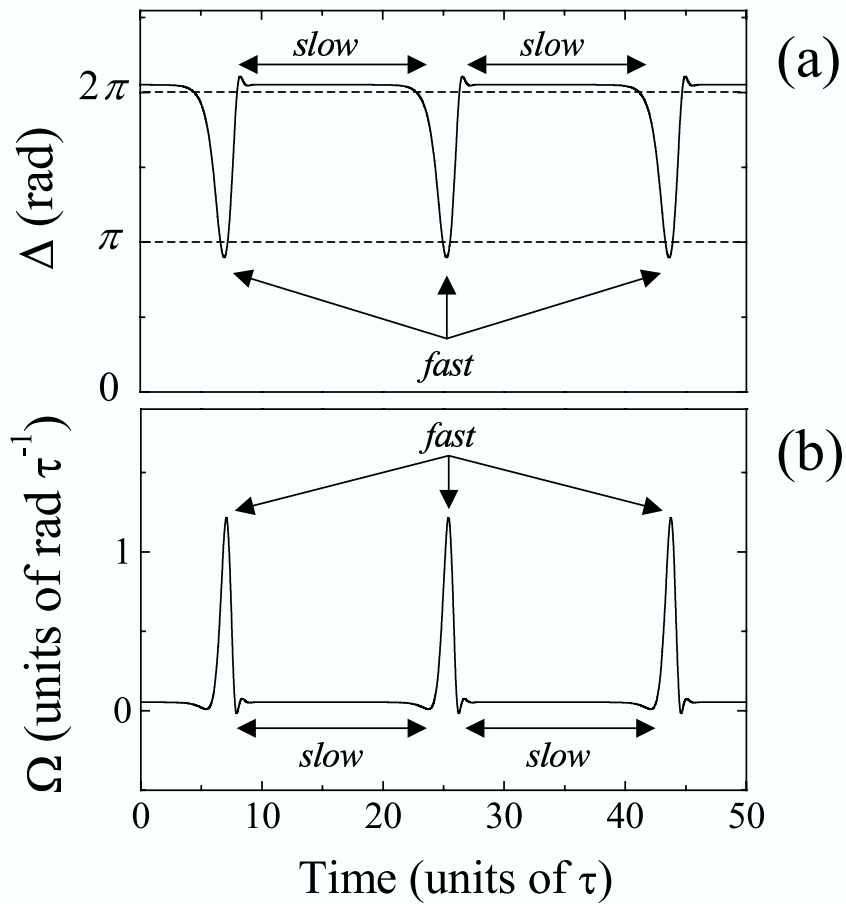


**Figure 2.14.** Calculated dynamics near  $\rho_3$  ( $\rho = 1.748542389055$ ). (a) Phase shift  $\Delta(t)$ . (b) Instantaneous angular velocity  $\Omega(t) = d\Phi_0/dt$ .

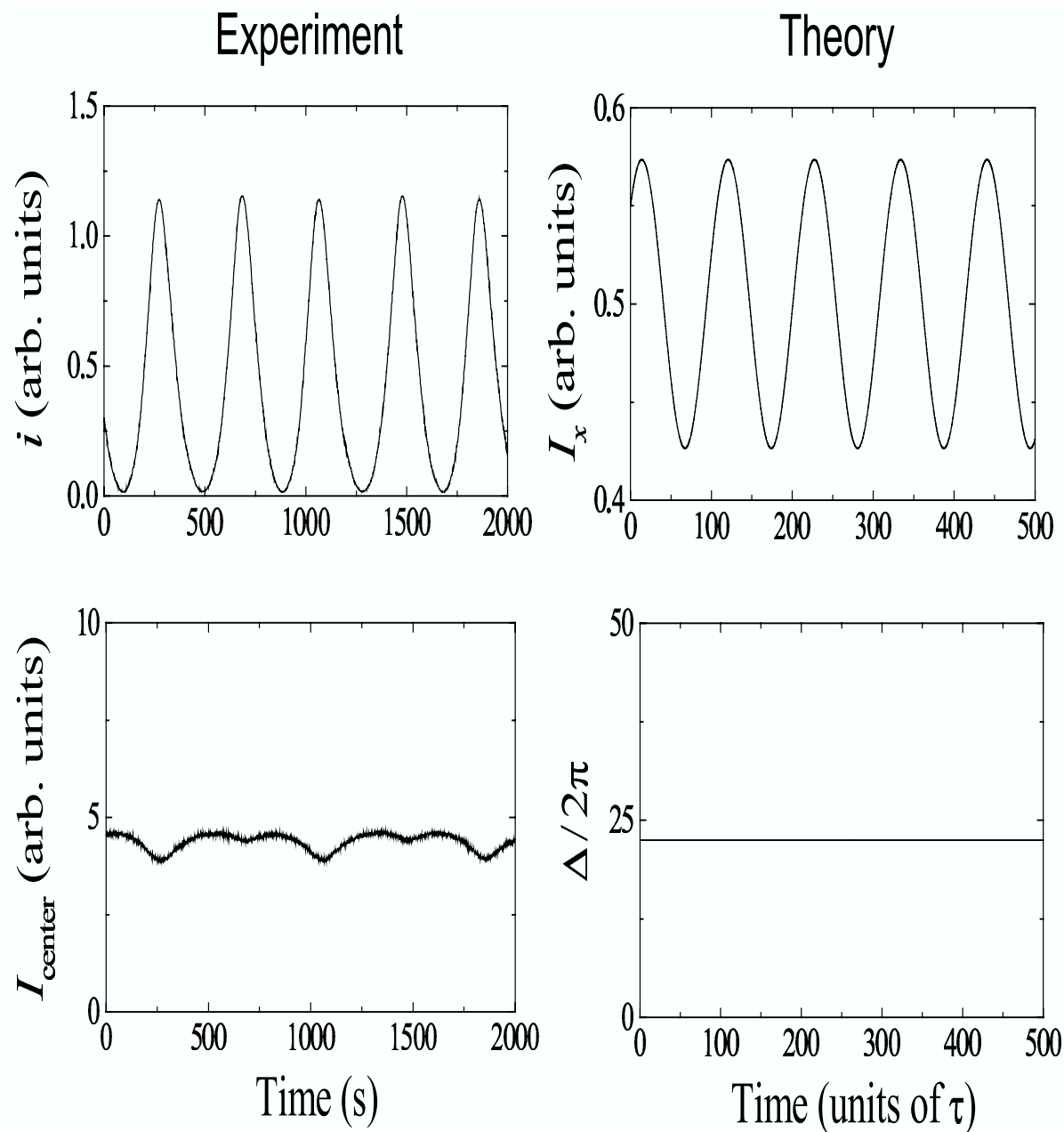


**Figure 2.15.** Director dynamics in the UP2 regime. Left part: experimental  $i(t)$  and  $I_{\text{center}}(t)$  just above the homoclinic bifurcation. Right part: calculated  $I_{x,y}(t)$  and  $\Delta(t)$  at  $\rho = 1.80$ .

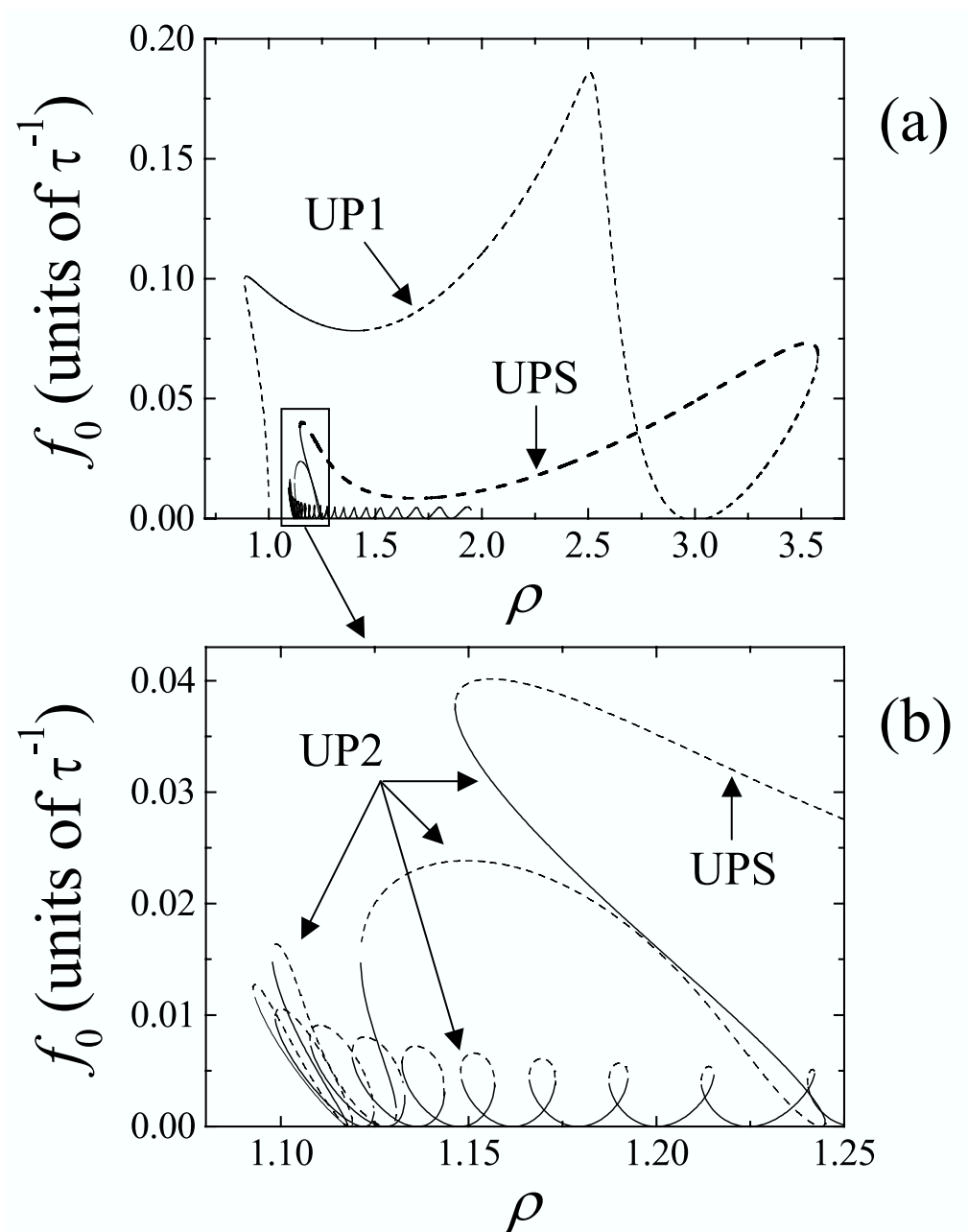


**Figure 2.16.** Precession frequency  $f_0(\rho)$  for the UP1, UPS and UP2 regimes. Part (b) magnifies the region delimited by the box in part (a). Solid (dashed) curves correspond to stable (unstable) solutions.

## 2.10 Approximate model for the uniform precession regimes

The problem can be considerably simplified and even solved analytically if we assume that the angle  $\Theta$  is small, keep only the first mode of  $\Theta$  and restrict our consideration to the case when the director precess uniformly ( $2\pi f_0 = d\Phi_0/dt$ ,  $d\Phi_n/dt = d\Theta_n/dt = 0$ ). We also assume that the gradient of the twist distortions  $\partial_z\Phi(z)$  is small which is well fulfilled for the UP1 regime described in Sec. 2.5.

The field equations (A.15) may be solved by means of successive iterations using  $|\partial_z\Phi| < 1$ . The zeroth-order solution of Eq. (A.15) is given by:

$$A_o^{(0)} = A_{o0}, \quad A_e^{(0)} = A_{e0} \cdot \left(\frac{\lambda_o}{\lambda_e}\right)^{\frac{1}{4}} \quad (2.21)$$

and the recurrence relations for the solutions have the following form:

$$\begin{cases} A_o^{(m)} = A_{o0} - \int_0^z dz' \partial_z \Phi \sqrt{\frac{\lambda_e}{\lambda_o}} e^{i\alpha(z')} A_e^{(m-1)} \\ A_e^{(m)} = A_{e0} - \int_0^z dz' \frac{\lambda_e' A_e^{(m-1)}}{4\lambda_e} + \int_0^z dz' \partial_z \Phi \sqrt{\frac{\lambda_o}{\lambda_e}} e^{-i\alpha(z')} A_o^{(m-1)} \end{cases} \quad (2.22)$$

The result after  $m$  iterations can be substituted into the evolution equations (2.4). Writing the angle  $\Theta$  in the form

$$\Theta = \Theta_1(t) \sin z \quad (2.23)$$

one can easily obtain the following relations for the phase delay  $\alpha(z)$  and that induced by the whole layer [see Eqs. (2.3)]:

$$\alpha(z) = \Delta v(z), \quad \Delta = \tilde{L} \Theta_1(t)^2, \quad (2.24)$$

where  $v(z)$  and the dimensionless thickness  $\tilde{L}$  are given by:

$$v(z) = \frac{z - \sin z \cos z}{\pi}, \quad \tilde{L} = \frac{\pi \sqrt{\varepsilon_\perp} \mu L}{2\lambda}, \quad \mu = \frac{\varepsilon_a}{\varepsilon_a + \varepsilon_\perp}. \quad (2.25)$$

We may use the first iteration  $m = 1$  for  $A_o, A_e$  [see Eqs. (2.22)] that includes the twist gradient  $\partial_z\Phi$  and substitute the result into the Eqs. (2.4), expanding all expressions as a power series in  $\Theta, \Phi$ . Retaining the terms up to third order in  $\Theta$  and keeping the lowest order terms in  $\partial_z\Phi$ , the equation for  $\Phi$  reduces to

$$2\pi f_0 \sin^2 z = \frac{d}{dz} [\sin^2 z \partial_z \Phi] + \rho \sin[\Delta v(z)] \sin^2 z. \quad (2.26)$$

One can obtain the following expressions for the frequency  $f_0$  and the twist gradient  $\partial_z \Phi$  by integrating Eq. (2.26) and evaluating the result at  $z = \pi$ :

$$f_0 = \frac{\rho (1 - \cos \Delta)}{2\pi \Delta}, \quad (2.27)$$

$$\partial_z \Phi = \frac{\pi \rho}{2\Delta} \frac{(1 - \cos \Delta)v(z) - 1 + \cos[\Delta v(z)]}{\sin^2 z}. \quad (2.28)$$

Similar simplifications of the equation for  $\Theta$  [see Eqs. (2.4)] yield the following result:

$$\begin{aligned} & [1 - (1 - k_1)\Theta^2]\Theta'' - (1 - k_1)\Theta\Theta'^2 - \Theta\Phi'^2 + \\ & \rho\Theta \left\{ 1 + \frac{9\mu - 4}{6}\Theta^2 + 2 \int_0^z dy \partial_z \Phi \sin[\Delta v(y)] \right\} = 0. \end{aligned} \quad (2.29)$$

After substituting Eqs. (2.23), (2.28) into Eq. (2.29) and projecting it onto the trial function  $\sin z$  we have a transcendent equation for  $\Delta$ :

$$\Delta \left[ 1 - \frac{(1 - k_1)\Delta}{2\tilde{L}} - \rho \left\{ 1 + \frac{(9\mu - 4)\Delta}{8\tilde{L}} \right\} + \frac{\rho^2}{2}G(\Delta) \right] = 0, \quad (2.30)$$

where  $G(\Delta)$  is defined as:

$$\begin{aligned} G(\Delta) &= 2\pi \int_0^\pi dz \frac{\sin[\Delta v](1 - v)[1 - \cos[\Delta v] - (1 - \cos \Delta)v]}{\Delta \sin^2 z} \\ &+ \pi \int_0^\pi dz \left[ \frac{1 - \cos[\Delta v] - (1 - \cos \Delta)v}{\Delta \sin z} \right]^2. \end{aligned} \quad (2.31)$$

The trivial solution  $\Delta = 0$  corresponds to the homeotropic orientation of the director. It is seen that the expression in the brackets of Eq. (2.30) is quadratic with respect to  $\rho$  with a solution given by (only one root leads to a physical solution):

$$\begin{aligned} \rho &= \frac{1}{G(\Delta)} \left[ 1 + \frac{(9\mu - 4)\Delta}{8\tilde{L}} - \right. \\ &\left. \left\{ \left( 1 + \frac{(9\mu - 4)\Delta}{8\tilde{L}} \right)^2 - 2G(\Delta) \left( 1 - \frac{(1 - k_1)\Delta}{2\tilde{L}} \right) \right\}^{\frac{1}{2}} \right]. \end{aligned} \quad (2.32)$$

This result coincides with the one obtained in [5] where the light propagation was treated in terms of the Stokes vector.

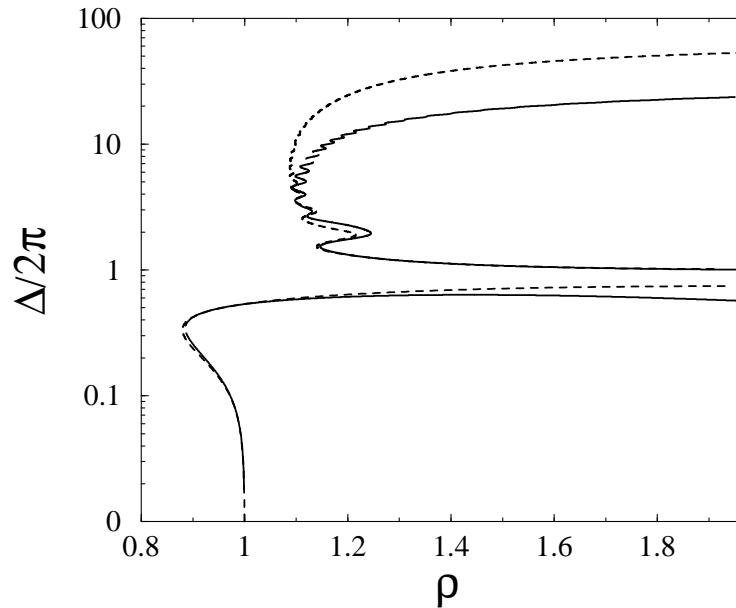


**Figure 2.17.** Phase delay  $\Delta/2\pi$  versus  $\rho$ .  
Dashed line: approximate solutions for the uniform director precession.  
Solid line: accurate solutions that are taken from Fig. 2.2.

In Fig. 2.17 the approximate solutions for  $\Delta(\rho)$  given by Eq. (2.32) and corresponding to UP1, UP2 and UPS solutions described in Sects. 2.4, 2.5 and 2.9 [see also Fig. 2.2] are shown (dashed lines) together with the accurate solutions obtained numerically (solid lines). One can see that the UP1 regime (at not too high values of  $\rho$ ) and the lowest part of the UP2 regime is described rather well by the approximate formula. The higher the values of  $\Delta$  are the worse the formula works because  $\Theta$  becomes large and the higher order modes of  $\Theta$  have to be taken into account. The loop depicted in Fig. 2.2(b) can not be reproduced in the framework of the approximate model for two reasons. One is, that Eq. (2.32) leads to complex values of  $\rho$  for the region of  $(\Delta, \rho)$  corresponding to the loop. The other is, that in Eq. (2.28) the gradient of the twist distortion  $\partial_z \Phi(z)$  is proportional to  $\rho/\Delta$ , which becomes large as  $\rho$  is increased since  $\Delta$  does not change considerably in the UP1 regime. Thus  $\partial_z \Phi(z)$  becomes large, and one iteration on  $A_o, A_e$  is insufficient to calculate the field.

## 2.11 Additional static fields

Having described in detail the different regimes encountered as the light intensity is varied, one can consider how to stabilize or destabilize some regimes to facilitate their observations. We extended slightly our model to include an additional static (low-

frequency) electric field aligned along the  $z$  axis (perpendicular to the layer). One should use  $ac$  fields with not too low frequency (say, above a few  $kHz$ ) in order to avoid complications due to electro-convection. We will nevertheless assume that the frequency is sufficiently low to apply the quasi-static approximation.

The second equation from Maxwell's Eqs. (1.9) gives the expression for the  $z$ -component of the static field:

$$E_z^{st} = \frac{C}{\varepsilon_{zz}^{st}}, \quad (2.33)$$

where

$$\varepsilon_{zz}^{st}(z) = \varepsilon_{\perp}^{st} + \varepsilon_a^{st} \cos^2 \Theta \quad (2.34)$$

is the  $z$  component of the dielectric tensor with the dielectric anisotropy  $\varepsilon_a^{st} = \varepsilon_{\parallel}^{st} - \varepsilon_{\perp}^{st}$  and the dielectric permittivity (for a low-frequency field)  $\varepsilon_{\perp}^{st}$  ( $\varepsilon_{\parallel}^{st}$ ) perpendicular (parallel) to  $\mathbf{n}$ . This field will help to stabilize [destabilize] our primary bifurcation scenario if the static dielectric anisotropy  $\varepsilon_a^{st} > 0$  [ $\varepsilon_a^{st} < 0$ ]. In Eq. (2.33)  $C$  is an unknown constant that can be found using the fact that the voltage  $V = E_0^{st} L$  applied between the substrates is fixed. Finally,  $E_z^{st}(z)$  is as follows (recall that we use the normalized  $z$  as before):

$$E_z^{st}(z) = \frac{\pi E_0^{st}}{\varepsilon_{zz}^{st}(z) \int_0^{\pi} \frac{dz}{\varepsilon_{zz}^{st}(z)}}. \quad (2.35)$$

The additional electric field exerts a torque on the director and must be taken into account by inserting

$$F_{st} = -\frac{\varepsilon_a^{st}}{8\pi} n_z^2 [E_z^{st}(z)]^2 \quad (2.36)$$

into the expression for the free energy (1.3). Eventually, Eq. (2.36) gives a contribution to the equation for  $\Theta$  only and the term we have to insert into  $\mathcal{L}_{\Theta}$  is [see Eqs. (2.4)]:

$$\mathcal{L}_{\Theta}^{st} = -\frac{\text{sign}(\varepsilon_a^{st})}{2} \frac{\pi^2 \sin 2\Theta e_{st}}{[\varepsilon_{zz}^{st}]^2 \left[ \int_0^{\pi} \frac{dz}{\varepsilon_{zz}^{st}} \right]^2}, \quad (2.37)$$

where  $e_{st}$  is the normalized strength of the electric field

$$e_{st} = \left( \frac{E_0^{st}}{E_{th}^{st}} \right)^2, \quad (E_{th}^{st})^2 = \frac{4\pi^3 K_3}{|\varepsilon_a^{st}| L^2}. \quad (2.38)$$

At  $e_{st} = 1$  and  $\rho = 0$  the classical Fréedericksz transition from homeotropic to stationary distorted state takes place (dielectric anisotropy should be negative of course  $\varepsilon_a^{st} < 0$ ) [48].

In Fig. 2.18 the phase delay  $\Delta$  versus  $\rho$  is shown for  $\varepsilon_a^{\text{st}} < 0$  and  $\varepsilon_a^{\text{st}} > 0$  for a given applied voltage  $V$ . For  $\varepsilon_a^{\text{st}} > 0$ , the static field plays a stabilizing role and the UP and NUP regimes shift to a region of higher intensities compared to the situation without static field ( $e_{st} = 0$ ). Moreover the region of the existence of the NUP regime becomes somewhat larger. This may be useful since it allows to make observations in the NUP for a wider range of excitation intensities. In contrast, when  $\varepsilon_a^{\text{st}} < 0$  [destabilizing effect] the regimes shift to lower intensities, while keeping the same sequence of bifurcations UP1  $\rightarrow$  NUP  $\rightarrow$  UP2 (not shown in the figure). Such a shift of the bifurcation thresholds may allow to carry out experiments at lower intensities. In addition, the range of intensities that corresponds to the NUP regime shrink to zero for sufficiently high  $e_{st}$  as seen in Fig. 2.18(a). Approximately at the same  $e_{st}$  the unstable loop (see Fig. 2.2(b)) is separated from the rest and reduces to an unstable "island". Also the strength of the hysteresis of the Fréedericksz transition decreases. This can be easily understood since for large values of  $e_{st}$ , the static electric torque dominates. In this limit, the behavior of the nematic cell will tend to be similar to one under the effect of a quasi-static field alone, for which the Fréedericksz transition is continuous (supercritical).

## 2.12 Discussion

In this chapter we have discussed the reorientation dynamics of a homeotropically aligned nematic liquid crystal film excited by circularly polarized light at normal incidence. The complete bifurcation scenario has been obtained theoretically.

It has been shown that the secondary instability above the optical Fréedericksz transition threshold is a *supercritical Hopf bifurcation*. As a result of this bifurcation, a quasi-periodic dynamics is generated where the motion of the director is a combination of precession and nutation with distinct fundamental frequencies. Moreover the discontinuous transition from the quasi-periodic regime to a uniform precession regime has been identified to be a *homoclinic bifurcation*. These results have been confirmed experimentally with the help of a pair of observable that allow to distinguish nutation from precession. The physical interpretation of the behavior of the nematic is based on the transfer of the spin angular momentum of the light to the liquid crystal.

Although homoclinic bifurcations play a key role in numerous systems their experimental identification is fairly scarce. We are here dealing with the simplest type where a limit cycle collides with a saddle point having one unstable direction [47]. Maybe the best-known examples for this case are systems described by the driven and damped

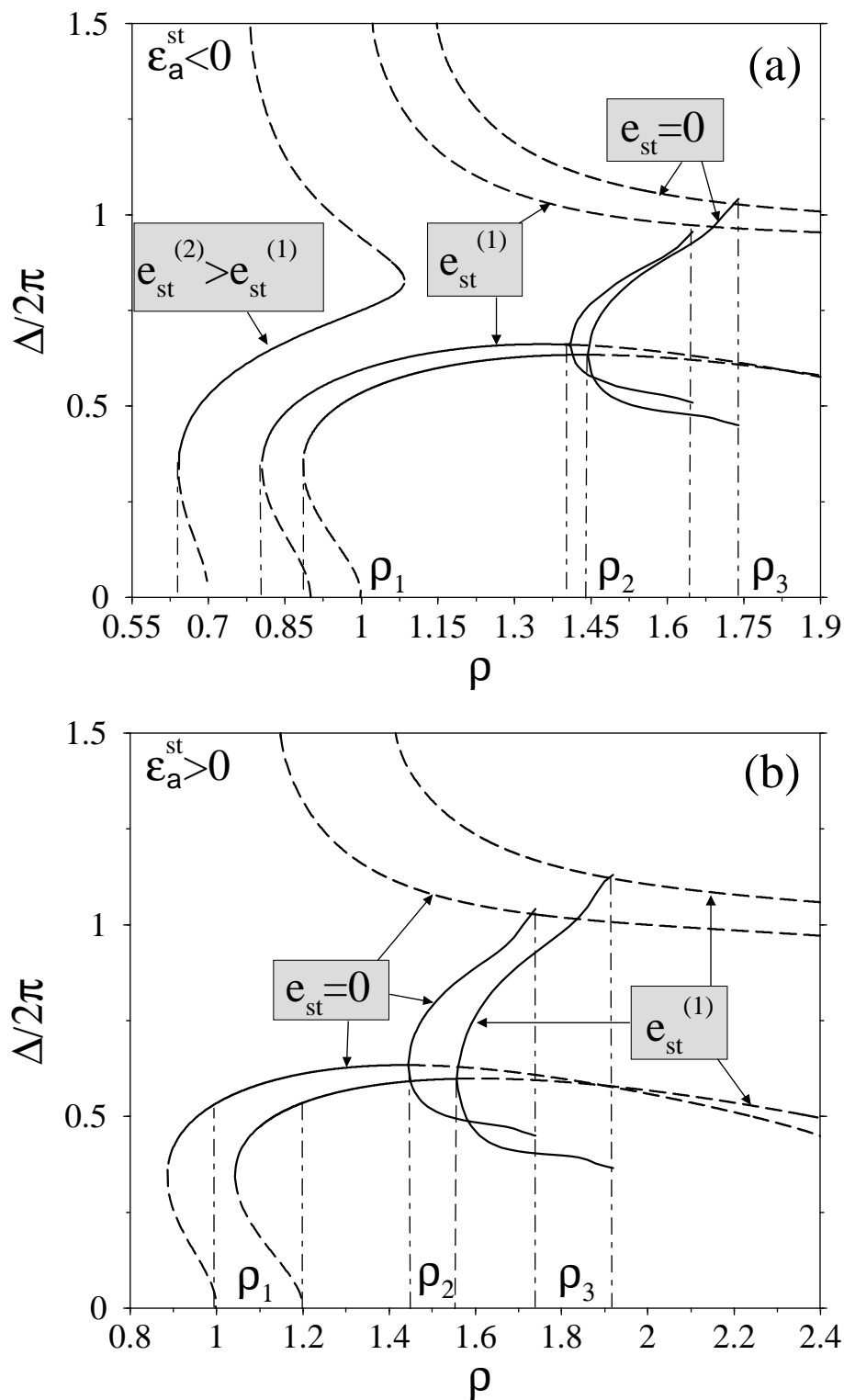


**Figure 2.18.** Effects of an additional static field on the bifurcation diagram for different signs of the static dielectric anisotropy. Destabilization occurs in the case  $\epsilon_a^{st} < 0$  [(a)] and  $e_{st} \neq 0$  while in the opposite case when  $\epsilon_a^{st} > 0$  [(b)] and  $e_{st} \neq 0$  the field plays a stabilizing role. Solid (dashed) curves correspond to stable (unstable) solutions.

Sine-Gordon equation, which includes, in particular, spatially restricted or extended Josephson contacts [49]. Actually the same equation describes driven and damped pendula. Examples of such a type of homoclinic bifurcations in hydrodynamic systems can be found in [50, 51]. More complicated homoclinic bifurcations may give rise to chaos as shown in classic work by Shil'nikov [47, 52]. For an experimental realization of such a scenario, see [53]. When a reflection symmetry is involved gluing of the two orbits can occur at the homoclinic point. An interesting example can be found in a light-driven instability in nematics involving a linearly polarized laser beam at oblique incidence [33, 34].

Further improvement of the theory involves generalization to finite beam size and the inclusion of the flow field excited by the motion of the director. Whereas the latter effect has been taken into account in the description of electric and magnetic field driven instabilities it has apparently never been considered in the context of light driven dynamic phenomena. It will be shown in Chapter 4 that in the system considered here only quantitative shifts of the various transitions arise [54]. Another direction of research could be the inclusion of lateral spatial degrees of freedom, as first done in the context of the oblique-incidence instability [55], see Chapter 5.



# Chapter 3

## Symmetry breaking effects in nonlinear reorientation dynamics induced by elliptically polarized light in nematics

It was shown in the previous chapter that circularly polarized light incident perpendicularly on a nematic layer induces quasiperiodic director rotation if the incident intensity exceeds the one for the Fréedericksz transition by about 40%. With further increase of the intensity a discontinuous transition via a homoclinic bifurcation takes place to a state of periodic rotation of the director with large reorientation. The aim of this chapter is to demonstrate the existence of analogous regimes for the case of elliptically polarized incident light. These are expected to be more complex because of the broken isotropy in the plane of the layer. Some features of the nonlinear dynamics induced by an elliptically polarized light were reported in Ref. [14,15] for intensities lower than that needed for the quasiperiodic director rotation.

### 3.1 Theoretical model

We consider an elliptically polarized (EP) plane wave incident perpendicularly on a layer of nematic that has initially homeotropic alignment (with strong homeotropic anchoring at the boundaries). The light is polarized in the plane of the layer (the  $\mathbf{x}, \mathbf{y}$  plane) and propagates along the positive  $\mathbf{z}$ -axis (see Fig. 2.1 in the previous chapter). Similar to Sec. 2.1 we use the representation (2.1) for the director and assume

$z, t$  dependence only. Thus the equations for the director motion and for the light propagation inside the layer are given, respectively, by Eqs. (2.4) and Eqs. (A.15). The boundary conditions for the angles  $\Theta$ ,  $\Phi$  and for the amplitudes  $A_o$ ,  $A_e$  (see Appendix A) are given respectively, by (2.7) and (A.17). We use the expansions (2.12) for  $\Theta$  and  $\Phi$  in order to derive a set of coupled nonlinear ODEs for the mode amplitudes  $\Theta_n(t)$ ,  $\Phi_n(t)$  analogous to Eqs. (2.15). The only difference in comparison with the case of the circular polarization is that in the elliptic case the equation (2.16) for  $\Phi_0$  is coupled with the rest of the equations (2.15) owing to the fact that  $\Phi_0$  does not disappear from the boundary conditions (A.17) whereas in the circular case it does [see Eq. (2.2)]. This is due to the broken rotational invariance around the  $z$ -axis. A regime of simple rotation of the director (when  $d\Phi_0/dt = \text{const}$  and  $d\Phi_n/dt = d\Theta_n/dt = 0$ ), possible in the CP case, can not be realized when the light ellipticity  $\chi \neq \pi/4$  [ $\chi$  varies between  $\pi/4$  (circular case) to 0 (linear polarization), see Appendix A]. In the EP case all modes (including  $\Phi_0$ ) are either time-dependent ( $d\Phi_0/dt \neq 0$ ,  $d\Phi_n/dt \neq 0$ ,  $d\Theta_n/dt \neq 0$ ) or time independent ( $d\Phi_0/dt = d\Phi_n/dt = d\Theta_n/dt = 0$ ) simultaneously.

In the calculations, we used same the material parameters and layer thickness as in Sec. 2.3.

## 3.2 Bifurcation scenario

In this section, the director motion is analyzed by taking  $\rho$  and  $\chi$  as control parameters [ $\rho = I/I_c$  is the normalized intensity introduced in Sec. 2.1, see Eq. (2.6)]. The results are presented for values of the ellipticity  $\chi$  from 0.35 to  $\pi/4$ . In this range numerous transitions between different dynamical regimes are observed. For lower values of  $\chi$  the rotating states we are interested in (see below) do not exist. Some aspects of the scenario in that region has been investigated in [15].

Figure 3.1 presents the different regimes that exist in the plane  $(\chi, \rho)$  for  $0.4 \leq \chi \leq \pi/4$ . Below the Fréedericksz threshold  $\rho_{\text{th}}$  that depends on  $\chi$  as [56]

$$\rho_{\text{th}} = \frac{1}{1 + \cos 2\chi} \quad (3.1)$$

the director is unperturbed (U) whereas above this threshold, one observes stationary distorted (D), oscillatory (O), periodic rotating (PR), quasi-periodic rotating (QPR) or largely distorted (LD) states depending on the values of  $\rho$  and  $\chi$ . Keeping the ellipticity fixed and increasing the intensity, these states appear as a well-defined sequence of transitions. In the range of interest for  $\chi$ , four distinct bifurcation sequences can be



**Table 3.1.** Calculated sequence of bifurcations as a function of the ellipticity  $\chi$  of the incident light.

Ellipticity	Sequence of transitions	Bifurcation nature
$0.35 < \chi < 0.53$	Unperturbed $\rightarrow$ Distorted	Pitchfork
	Distorted $\rightarrow$ Periodic oscillation	Supercritical Hopf
	Periodic oscillation $\rightarrow$ Periodic rotation	Gluing
	Periodic rotation $\rightarrow$ Periodic oscillation or distorted	Continuous
$0.53 < \chi < 0.72$	Unperturbed $\rightarrow$ Distorted	Pitchfork
	Distorted $\rightarrow$ Periodic oscillation	Supercritical Hopf
	Periodic oscillation $\rightarrow$ Periodic rotation-1	Gluing
	Periodic rotation-1 $\rightarrow$ Periodic rotation-2	Saddle-node
	Periodic rotation-2 $\rightarrow$ Distorted	continuous <sup>a</sup> or discontinuous <sup>b</sup>
$0.72 < \chi < \pi/4$	Unperturbed $\rightarrow$ Distorted	Pitchfork
	Distorted $\rightarrow$ Periodic oscillation	Supercritical Hopf
	Periodic oscillation $\rightarrow$ Periodic rotation-1	Gluing
	Periodic rotation-1 $\rightarrow$ Periodic rotation-2	Saddle-node
	Periodic rotation-2 $\rightarrow$ Quasi-periodic rotation	Supercritical Hopf
	Quasi-periodic rotation $\rightarrow$ Distorted or periodic rotation	Discontinuous
$\chi = \pi/4$	Unperturbed $\rightarrow$ Periodic rotation	Subcritical Hopf
	Periodic rotation $\rightarrow$ Quasi-periodic rotation	Supercritical Hopf
	Quasi-periodic rotation $\rightarrow$ Periodic rotation	Homoclinic

<sup>a</sup>for  $\chi < 0.66$

<sup>b</sup>for  $\chi > 0.66$

**Table 3.2.** Spectral content  $n_{x,y}(t)$ ,  $I_{x,y}(t)$  and  $\Delta(t)$  for the different dynamical regimes for an elliptically polarized incident light.

Regime	$n_{x,y}$	$I_{x,y}$	$\Delta$
Periodic oscillation	$nf_0$	$nf_0$	$nf_0$
Periodic rotation	$(2n-1)f_0$	$2nf_0$	$2nf_0$
Quasi-periodic rotation	$nf_1 \pm (2m+1)f_0$	$nf_1 \pm 2mf_0$	$nf_1 \pm 2mf_0$

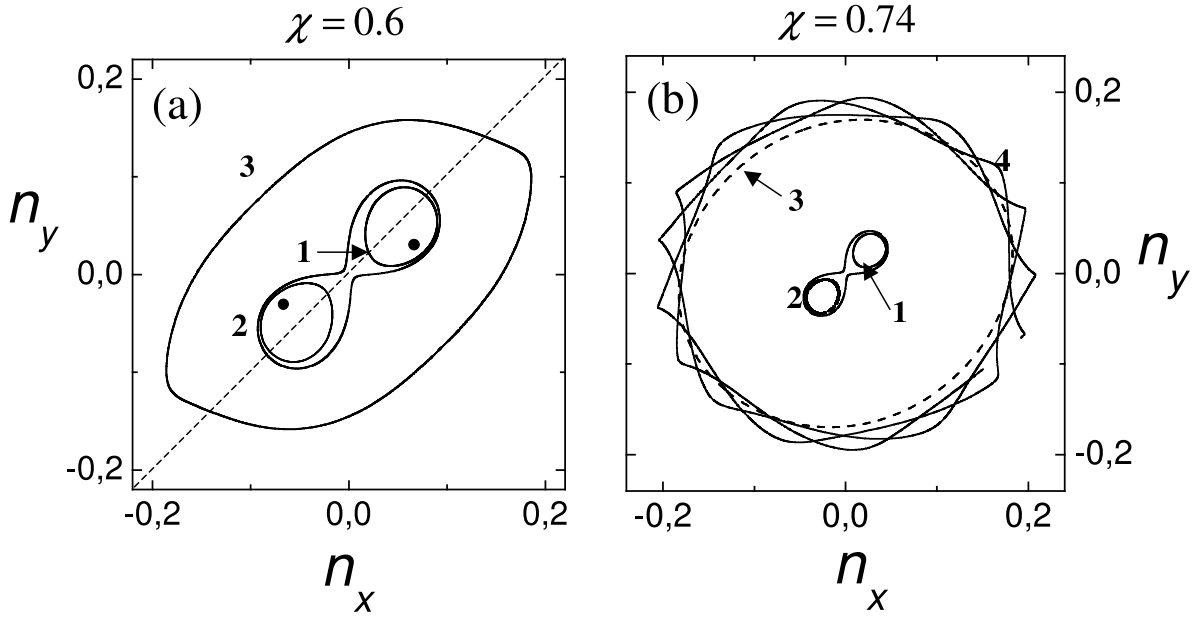


**Figure 3.2.** Calculated director trajectories in the  $(n_x, n_y)$  plane. (a)  $\chi = 0.6$ : distorted state at  $\rho = 0.8$  ( $\bullet$ ); periodic oscillating state at  $\rho = 0.91$  (curve 1); periodic rotating state  $PR_1$  slightly above the gluing bifurcation at  $\rho = 0.917$  (curve 2); periodic rotating state  $PR_2$  at  $\rho = 0.95$  (curve 3). (b)  $\chi = 0.74$ : periodic oscillating state at  $\rho = 0.9925$  (curve 1); periodic rotating state  $PR_1$  slightly above the gluing bifurcation at  $\rho = 0.9932$  (curve 2); periodic rotating state  $PR_2$  slightly above the saddle-node bifurcation at  $\rho = 0.9936$  (curve 3, dashed line); quasi-periodic rotating state at  $\rho = 1.5$  (curve 4).

consists of oscillatory states (near  $\chi = 0.35$ ) or stationary distorted states.

For  $0.53 < \chi < 0.72$  there is one more regime. In fact, the limit cycle amplitude of the PR regime, now labeled  $PR_1$  [curve 2 in Figs. 3.2(a)], abruptly increases. This results in another periodic rotating regime labeled  $PR_2$  with higher reorientation amplitude [curve 3 in Figs. 3.2(a) and 3.2(b)]. The transition takes place via a *saddle-node bifurcation* (not shown in Fig. 3.1 because it is very near to the gluing bifurcation) which additionally allows for the hysteretic behavior when the intensity is reduced starting from the  $PR_2$  state, as already discussed in Ref. [15]. The system switches back to the O or D state at the line labeled  $h_{PR}$  in Fig. 3.1. In contrast, no hysteresis is observed when  $\rho$  is decreased starting from the  $PR_1$  regime since the  $O \rightarrow PR_1$  transition is continuous. Finally, for high intensity there is a continuous (for  $\chi < 0.66$ ) or discontinuous (for  $\chi > 0.66$ ) transition to a LD regime represented by stationary distorted states. For  $\chi > 0.66$  the  $PR_2 \rightarrow LD$  transition is discontinuous and hysteretic. In that case, the system remains largely reoriented when the intensity is reduced until the hysteretic line  $h_{LD}$  is reached, for which the system switches to the  $PR_2$  regime with small reorientation (Fig. 3.1).

For  $0.72 < \chi < \pi/4$  one has the sequence  $U \rightarrow D \rightarrow O \rightarrow PR_1 \rightarrow PR_2$  as before [see Figs. 3.1, 3.2(b)]. However, for higher values of  $\rho$  a QPR regime is born through a *secondary supercritical Hopf bifurcation*, which introduces a new frequency  $f_1$  into the system and transforms the dynamics into quasi-periodic [curve 4 in Fig. 3.2(b)]. As the intensity increases the QPR state undergoes a discontinuous transition to a LD regime represented by a stationary distorted or slowly rotating (close to  $\chi = \pi/4$ ) state.

The particular case  $\chi = \pi/4$ , which corresponds to CP incident light, has been the subject of Chapter 2. The results are summarized at the end of Table 3.1.

The signature of the anisotropy of incident light is visible in the director trajectories in the  $(n_x, n_y)$  plane. The PR trajectories are obviously non circularly symmetric for  $\chi = 0.6$  [curves 2 and 3 in Fig. 3.2(a)] whereas the  $PR_2$  and QPR states are almost circularly symmetric when the polarization is almost CP [curves 3 and 4 in Fig.3.2(b)]. It is also worth recalling that the dynamical regimes O, PR and QPR can be described by means of one (for O and PR regimes) or two (for QPR regime) frequencies,  $f_0$  and  $f_1$  respectively. The spectral content of the variables  $n_{x,y}$ ,  $\Delta$  and  $I_{x,y}$  is listed in Table 3.2. In fact, it is simple to identify a given dynamical regime by looking at the spectra of the relevant variables.

Our results may be compared with previous theoretical treatment [15]. The equations of motion for the director in Ref. [15] were solved using the same mode expansion as we have done here, but retaining only  $\Theta_1$  and at least the  $\Phi_0$  and  $\Phi_1$  modes [inclusion of additional twist modes  $\Phi_{n \geq 2}$  were shown not to alter qualitatively the dynamics]. In distinction to our calculations however, their coupled mode equations have been solved in the small distortion approximation. The QPR regime was not found by this approach although other dynamical regimes such as O and PR were obtained and observed experimentally [14]. The reason is that higher nonlinearities on the twist gradient, namely  $(\partial_z \Phi)^2$  and higher order modes of  $\Theta$  start to play a key role at higher  $\rho$  that are neglected in this reduced model. The observation of the QPR state was reported in the particular case of a CP incident light [12, 13] and was later clearly understood theoretically [43].

Below we discuss more specifically some of the bifurcations when the polarization state of the incident light varies and present experimental confirmation. We shall focus on the case of ellipticity close to  $\chi = \pi/4$  for which a transition from a periodic to quasi-periodic rotating regime is expected.

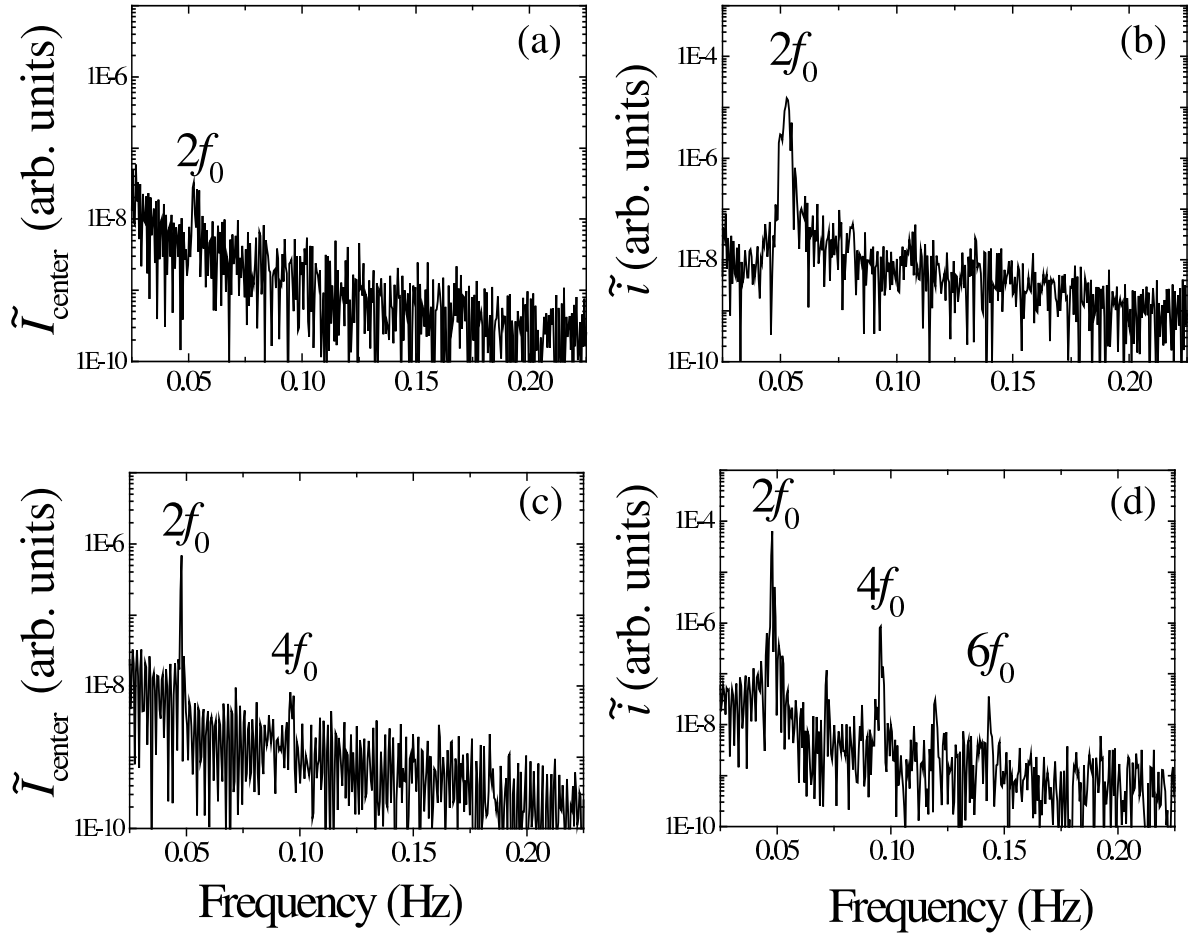


**Figure 3.3.** Experimental power spectra of  $I_{\text{center}}(t)$  and  $i(t)$  in the periodic rotating regime for  $\rho = 1.10$  and  $\chi \approx \pi/4$  (a-b) and  $\chi = 0.74$  (c-d).

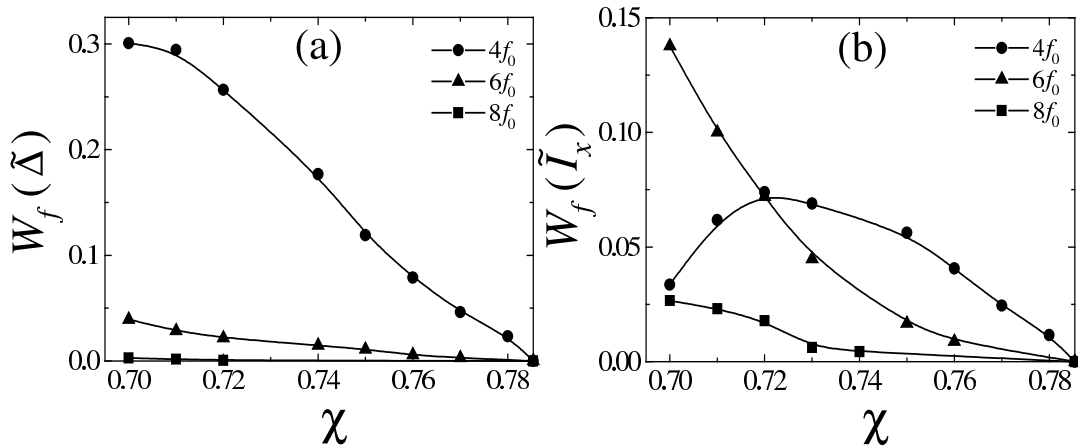


**Figure 3.4.** Calculated amplitudes of the peaks at frequencies  $2nf_0$  ( $2 \leq n \leq 4$ ) normalized to the peak at  $2f_0$  in the power spectra of (a)  $\Delta(t)$  and (b)  $I_{x,y}(t)$  versus  $\chi$  for  $\rho = 1.10$ . The solid line is to guide the eye.

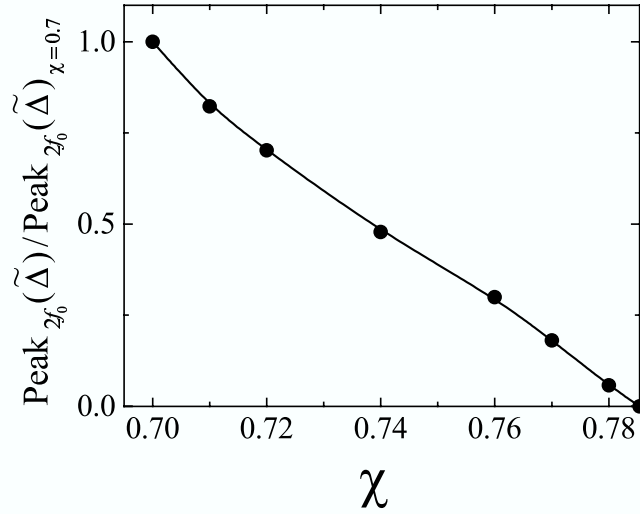


**Figure 3.5.** Calculated amplitude of the fundamental peak  $2f_0$  in the power spectrum of  $\Delta(t)$  versus  $\chi$  normalized to the peak at  $2f_0$  at  $\chi = 0.7$ , for  $\rho = 1.10$ . The solid line is to guide the eye.

### 3.3 Periodic rotating regime

When the system is in the PR state all the spectra of the dynamical variables (see Table 3.2) are described by a single frequency  $f_0$  (and, for  $\chi < \pi/4$ , its harmonics). The experimental observation is shown <sup>1</sup> in Figs. 3.3 where the power spectra of  $I_{\text{center}}$  and  $i(t)$  are plotted for  $\rho = 1.10$ ,  $\chi = \pi/4$  (a-b) and  $\rho = 1.10$ ,  $\chi = 0.74$  (c-d). Recall that  $I_{\text{center}}(\text{experimental})$  should be related to  $\Delta(\text{theoretical})$  and  $i(\text{experimental})$  to  $I_{x,y}(\text{theoretical})$  (for more details see Sec. 2.4). As expected from theory, only at  $\chi = 0.74$  do both spectra exhibit clear harmonics  $2nf_0$  (Table 3.2). The harmonic  $4f_0$  is clearly visible in the spectrum of  $I_{\text{center}}$  [Fig. 3.3(c)] and the harmonics  $4f_0$  and  $6f_0$  are also apparent in the spectra of  $i$  [Fig. 3.3(d)]. Figure 3.4 shows the calculated amplitude of a given peak  $W_f$  at frequency  $f$  normalized to the peak at  $2f_0$  in the power spectra of  $\Delta$  and  $I_{x,y}$  as a function of  $\chi$  for  $\rho = 1.10$ . One sees that the peaks at  $2nf_0$  with  $n \geq 2$  tend to zero as the polarization becomes circular ( $\chi \rightarrow \pi/4$ ). On the other hand, the amplitude of the power spectrum of  $\Delta$  at the frequency  $2f_0$  also goes to zero when  $\chi$  approaches  $\pi/4$  (Fig. 3.5) since the rotation is uniform in the CP case ( $\Delta = \text{const}$ ). These trends are confirmed experimentally in Figs. 3.3(a-b) which correspond to CP incident light. In these experiments, the angle  $\chi$  satisfies  $\chi \geq 0.78$ , i.e. within 1% or better accuracy of the ideal value  $\pi/4$ . We believe that non perfect rotational invariance can explain the residual appearance of the frequency  $2f_0$  in Fig. 3.3(a). The following estimate illustrates this. From Fig. 3.3(a) the ratio of the peaks

---

<sup>1</sup>The experimental data was provided by E. Brasselet et al.

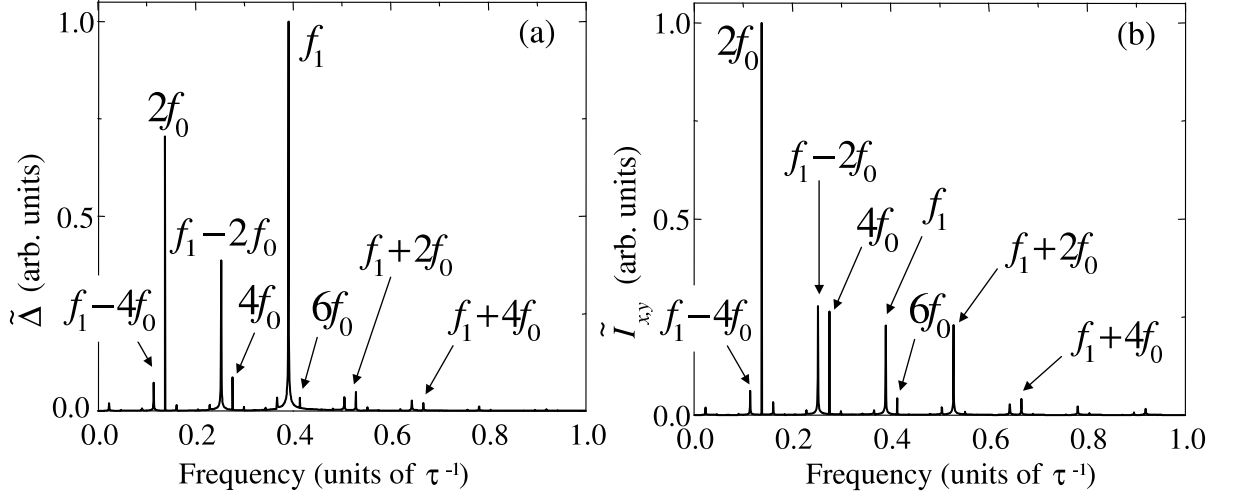


**Figure 3.6.** Calculated power spectra  $\tilde{\Delta}$  (a) and  $\tilde{I}_{x,y}$  (b) in the quasi-periodic rotating regime for  $\rho = 1.50$  at  $\chi = 0.74$ .

at  $f = 2f_0$  for  $\tilde{I}_{center}$  turns out to be  $W_{\chi \simeq \pi/4}(\tilde{I}_{center})/W_{\chi=0.74}(\tilde{I}_{center}) = 0.047$ . From the curve in Fig. 3.5 one then reads off a value of  $\chi = 0.783$  that is consistent with the experimental constraint.

### 3.4 Transition from periodic to quasi-periodic rotating regime

As shown in Fig. 3.1, when  $\chi > 0.72$ , the periodic rotating regime is predicted to lose its stability at  $\rho = \rho_2$  (which depends on  $\chi$ ): the resulting director dynamics then becomes a quasi-periodic rotation characterized by two frequencies  $f_0$  and  $f_1$ . This is illustrated in Figs. 3.6(a-b) where the power spectra of  $\Delta$  and  $I_{x,y}$  are plotted for  $\chi = 0.74$  and  $\rho = 1.50$ . Although the PR  $\rightarrow$  QPR transition appears to be similar to the one observed in the CP case, the spectral composition of the dynamical variables in the QPR state are different in the CP and EP cases. This is seen in the comparison of Figs. 2.9(a-b) (from the previous Chapter), taken at  $\chi = \pi/4$  and  $\rho = 1.50$ , with Figs. 3.6(a-b). The spectra of  $\Delta$  and  $I_{x,y}$  both contain the frequencies  $nf_1 \pm 2mf_0$  in the EP case while  $\tilde{\Delta} = nf_1$  and  $\tilde{I}_{x,y} = nf_1 \pm 2f_0$  in the CP case [see Table 3.2 and Eq. (2.20)]. In other words, both precession i. e. the motion of  $\Phi$ , and nutation, i. e. the motion of  $\Theta$ , are quasi-periodic (two frequencies  $f_0$  and  $f_1$ ) and nonlinear (presence of harmonics) in the EP case. In contrast, in the CP case these motions are both nonlinear but only precession is quasi-periodic. For  $\rho = 1.10$ , the director performs a

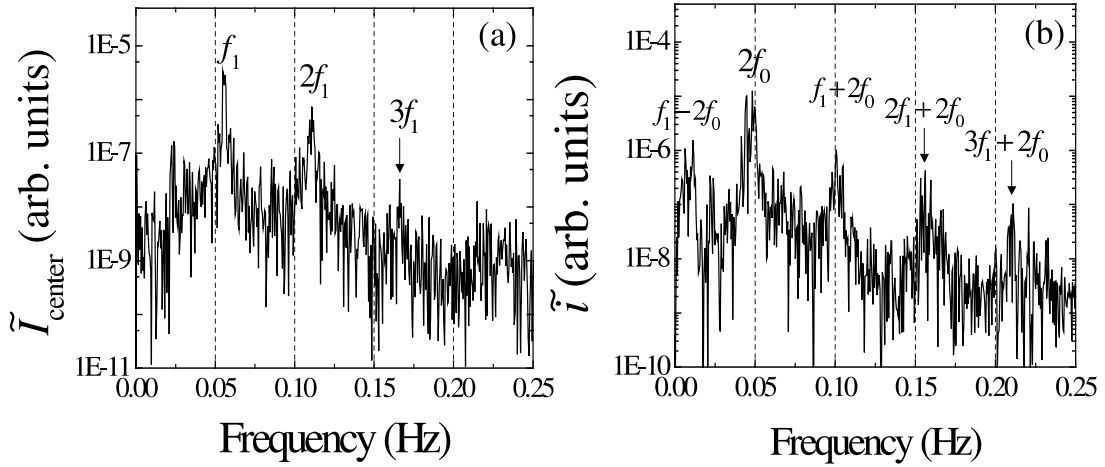


**Figure 3.7.** Experimental power spectra of  $I_{\text{center}}(t)$  (a) and  $i(t)$  (b) in the quasi-periodic rotating regime for  $\rho = 1.30$  and  $\chi = 0.76$ .

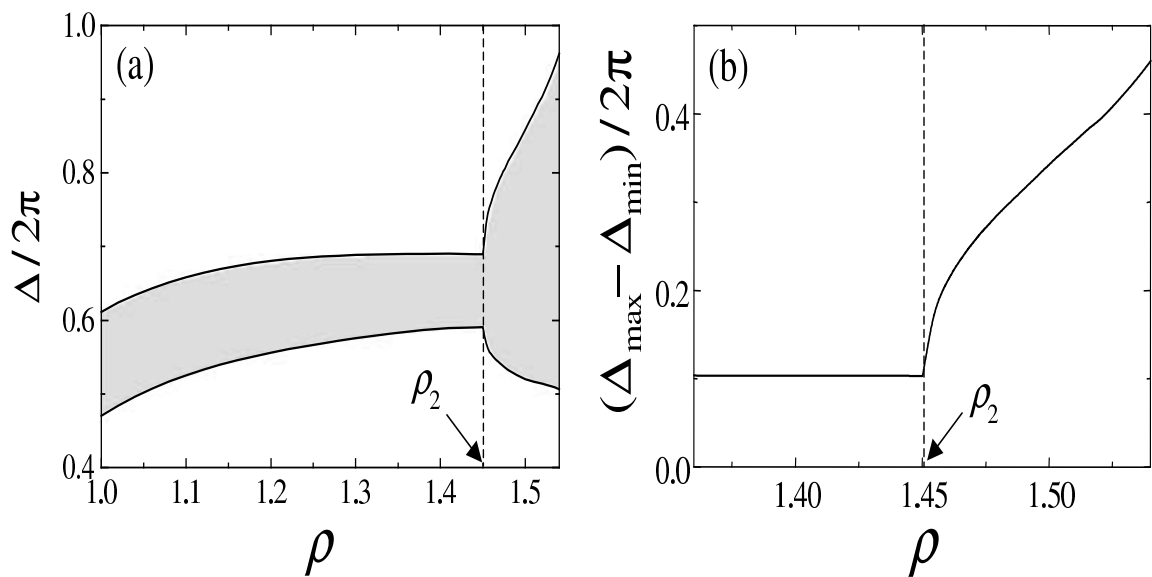


**Figure 3.8.** Calculated  $\Delta/2\pi$  versus  $\rho$  at  $\chi = 0.74$  showing the supercritical Hopf bifurcation between the periodic and the quasi-periodic rotating regime at  $\rho = \rho_2$ . (a) The gray region represents the values explored during the oscillations of  $\Delta(t)$ . (b) Amplitude  $\mathcal{A} = \Delta_{\text{max}} - \Delta_{\text{min}}$  of the oscillation of  $\Delta(t)$  in the neighborhood of the bifurcation point  $\rho = \rho_2$ .

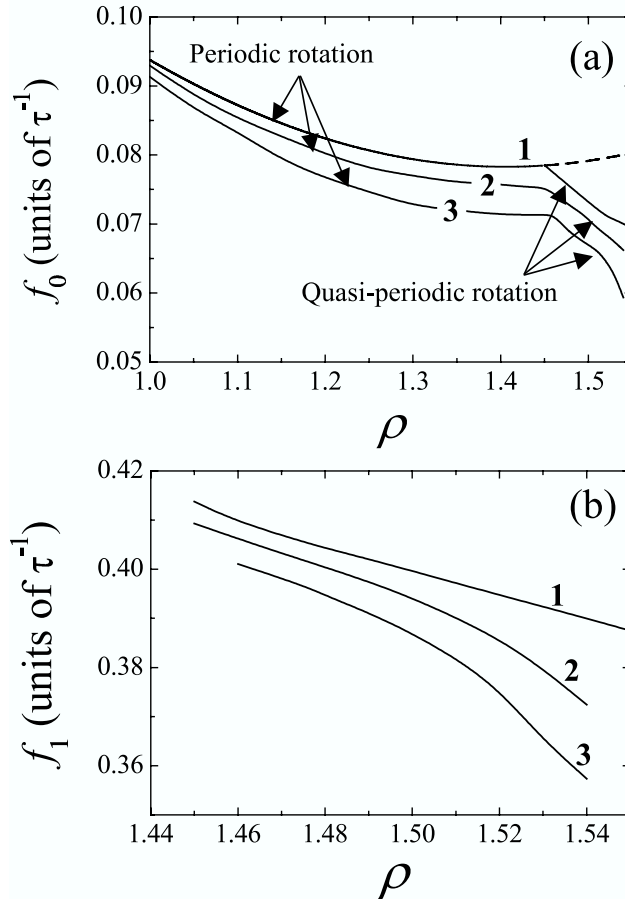


**Figure 3.9.** Calculated characteristic frequencies  $f_0$  (a) and  $f_1$  (b) versus  $\rho$  in the periodic and quasi-periodic rotating regime for  $\chi = \pi/4$  (curve 1),  $\chi = 0.75$  (curve 2) and  $\chi = 0.73$  (curve 3).

periodic motion characterized by a unique frequency  $f_0$ , as expected. At the transition to quasi-periodic dynamics, the emergence of the new frequency  $f_1$  and its harmonics changes dramatically the appearance of the experimental spectra of  $I_{\text{center}}$  and  $i$ . Figure 3.7 illustrates this point at  $\rho = 1.30$  and  $\chi = 0.76$ . As predicted by theory,  $f_1$  is the dominant frequency of  $\tilde{I}_{\text{center}}$  [Fig. 3.7(a)] and  $2f_0$  is the dominant frequency of  $\tilde{i}$  [Fig. 3.7(b)].

The nature of the bifurcation at  $\rho = \rho_2$  can be further characterized by verifying the scaling properties associated with the bifurcation. First we have checked that the amplitude of the limit cycle,  $\mathcal{A}$ , satisfies the scaling law  $\mathcal{A}(\rho) - \mathcal{A}(\rho_2) = \mathcal{O}(\rho - \rho_2)^{1/2}$  in the neighborhood of the bifurcation point. For this purpose, we define theoretically this amplitude as  $\mathcal{A} = (\Delta_{\text{max}} - \Delta_{\text{min}})/2\pi$  where  $\Delta_{\text{max},\text{min}}$  are respectively the maximum and the minimum of  $\Delta(t)$  for a given  $\rho$ . The results are shown in Fig. 3.8 where  $\mathcal{A}$  is plotted versus  $\rho$ . We found that in vicinity of the bifurcation  $\mathcal{A}(\rho) - \mathcal{A}(\rho_2) = \mathcal{O}(\rho - \rho_2)^\gamma$  with  $\gamma \simeq 0.5$  and  $\rho_2 \simeq 1.45$ . We have also verified that the frequency  $f_1$  satisfies the

scaling law  $f_1(\rho) - f_1(\rho_2) = \mathcal{O}(\rho - \rho_2)$  as one can see from Fig. 3.9(b). In summary, all these results confirm that there is a supercritical Hopf bifurcation at  $\rho = \rho_2$ .

### 3.5 Quasi-periodic rotating regime

The dependence of the calculated frequencies  $f_0$  and  $f_1$  as a function of the incident intensity are displayed in Fig. 3.9 for different values of  $\chi$ :  $\chi = \pi/4$  (curve 1),  $\chi = 0.75$  (curve 2) and  $\chi = 0.73$  (curve 3). The frequency  $f_0$  is obtained from the Fourier spectrum of  $I_{x,y}$ , which exhibits the dominant frequency  $2f_0$  [see Fig. 3.3(d) in the PR regime and Figs. 3.6(b) and 3.7(b) in the QPR regime]. The frequency  $f_1$  in the QPR regime is extracted from the Fourier spectrum of  $\Delta$ , where it is the dominant frequency [see Figs. 3.6(a) and 3.7(a)].

One can see that as in the CP case the transition PR  $\rightarrow$  QPR is accompanied by a sudden change of slope of the precession frequency  $f_0$  versus intensity [see Fig. 3.9(a)]. As in the CP case this is related with a fact, that in the NUP regime, the phase shift  $\Delta$  has values closer to  $2\pi$  as  $\rho$  increases [see Fig. 3.8(a)]. Moreover it is seen from Figs. 3.9(a-b) that a decrease of the ellipticity at fixed intensity corresponds to a decrease of both  $f_0$  and  $f_1$ . The decrease of  $f_0$  is related to the fact that the mean value  $\langle \Delta \rangle_t$  of  $\Delta(t)$  at fixed  $\rho$  becomes closer to  $2\pi$  as  $\chi$  decreases [see Fig. 3.10].

The analysis of the QPR  $\rightarrow$  LD transition in the EP case is more complicated than in the CP case where it was shown that the bifurcation is homoclinic of the simplest type with a limit cycle that collides with a saddle point having one unstable direction (see previous Chapter). It is no longer possible to easily obtain the unstable PR solutions allowing to classify the bifurcation when  $\chi \neq \pi/4$ : the loss of rotational invariance leads to time-dependent mode amplitudes  $\Theta_n$  and  $\Phi_n$  for all  $n$ . At present, we can only ascertain that the transition from QPR to LD states is discontinuous and associated with a hysteretic behavior. The LD regime consists of either rotating states, whose rotation frequency is at least one order of magnitude slower than that for the PR states, or distorted states. In fact, the slowly rotating LD state exists only in a very narrow region of  $\chi$  close to  $\chi = \pi/4$ .

### 3.6 Discussion

The nonlinear reorientation dynamics generated by elliptically polarized light at normal incidence to a homeotropic nematic liquid crystal film has been studied theoretically.

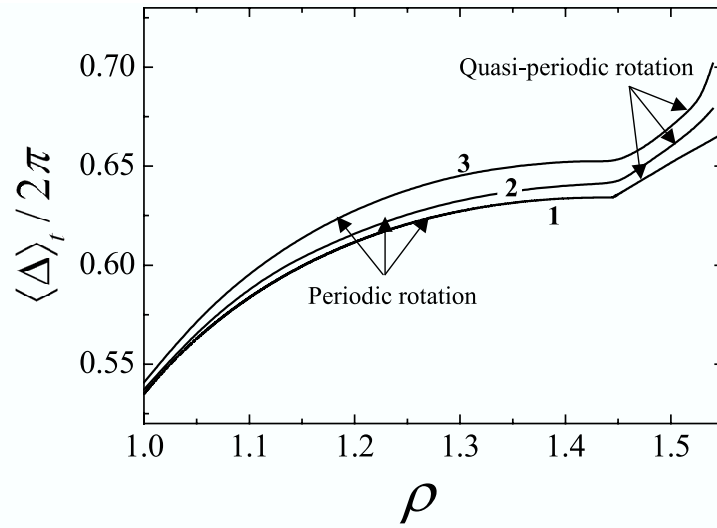


**Figure 3.10.** Calculated mean value  $\langle \Delta \rangle_t$  of  $\Delta(t)$  versus  $\rho$  in the periodic and quasi-periodic rotating regime for  $\chi = \pi/4$  (curve 1),  $\chi = 0.75$  (curve 2) and  $\chi = 0.73$  (curve 3).

The complete bifurcation diagram with the light intensity and the ellipticity as control parameters has been calculated rigorously. We have found that the quasiperiodic regime extends from the circular polarization to the elliptical one down to the value  $\chi = 0.72$ . However, in the latter case the spectra of the dynamical variables become more complicated although they are still characterized in terms of two distinct frequencies associated with precession and nutation. As in the circular case the quasiperiodic states appear in a supercritical Hopf bifurcation. Experimental observations have confirmed the existence of the new regime and its occurrence, in a small range of ellipticity close to circular polarization.



# Chapter 4

## Influence of the backflow effect on the orientational dynamics induced by light in nematics

We have seen in previous chapters that the director dynamics in a nematic is very rich when intense light propagates through it. However, in the theoretical models described up to now the velocity field was supposed to be zero  $\mathbf{v} = 0$ . The aim of this chapter is to clarify the influence of the backflow effect (at least in one particular geometry). Thereby, for the first time a full theory is developed for the nonlinear behavior of a nematic starting from the nematodynamic equations, which eventually could be used for a quantitative comparison with experiment. The same problem will be considered here as in Chapter 2 (see also Fig. 2.1) but with the inclusion of flow.

### 4.1 Basic equations

Using the macroscopic approach for the nematic developed in [57,58] the Navier-Stokes equation for the velocity  $\mathbf{v}$  can be written as [59]:

$$\rho_m (\partial_t + \mathbf{v} \cdot \nabla) v_i = -\nabla_j (p \delta_{ij} + \pi_{ij} + T_{ij}^{visc}), \quad (4.1)$$

where  $\rho_m$  and  $p$  are the density of the LC and the pressure respectively.  $\pi_{ij}$  is the Ericksen stress tensor <sup>1</sup> defined as:

$$\pi_{ij} = \frac{\partial F}{\partial (\partial_j n_k)} \cdot \partial_i n_k \quad i = x, y, z \quad (4.2)$$

---

<sup>1</sup>summation over doubly occurring indices is assumed.

with the free energy density  $F$  [see Eq. (1.5)]. The viscous stress tensor  $T_{ij}^{visc}$  in Eq. (4.1)

$$-T_{ij}^{visc} = \alpha_1 n_i n_j n_k n_l A_{kl} + \alpha_2 n_j N_i + \alpha_3 n_i N_j + \alpha_4 A_{ij} + \alpha_5 n_j n_k A_{ki} + \alpha_6 n_i n_k A_{kj} \quad (4.3)$$

is written in terms of the six Leslie coefficients  $\alpha_i$  [58], the symmetric strain-rate tensor  $A_{ij}$  and the vector  $\mathbf{N}$ , which gives the rate of change of the director relative to the fluid:

$$\begin{aligned} A_{ij} &= (\partial_i v_j + \partial_j v_i)/2, \\ \mathbf{N} &= (\partial_t + \mathbf{v} \cdot \nabla) \mathbf{n} - \boldsymbol{\omega} \times \mathbf{n}. \end{aligned} \quad (4.4)$$

Here  $\boldsymbol{\omega} = (\nabla \times \mathbf{v})/2$  is the local fluid rotation. The Leslie coefficients are linked by the Parodi relation [60]:

$$\alpha_2 + \alpha_3 = \alpha_6 - \alpha_5. \quad (4.5)$$

In addition we assume incompressibility of the fluid (the density  $\rho_m$  is constant):

$$\nabla \cdot \mathbf{v} = 0. \quad (4.6)$$

The equation for the director  $\mathbf{n}$  that is coupled with the equation for the velocity  $\mathbf{v}$  Eq. (4.1) is:

$$\gamma_1 (\partial_t + \mathbf{v} \cdot \nabla - \boldsymbol{\omega} \times) \mathbf{n} = -\underline{\underline{\delta}}^\perp (\gamma_2 \underline{\underline{A}} \mathbf{n} + \mathbf{h}), \quad (4.7)$$

where  $\gamma_1 = \alpha_3 - \alpha_2$  and  $\gamma_2 = \alpha_3 + \alpha_2$ . The projection tensor  $\underline{\underline{\delta}}^\perp$  and the molecular field  $\mathbf{h}$  were already introduced in Chapter 1 [see Eqs. (1.4), (1.5)]. One can see that in the absence of the velocity field,  $\mathbf{v} = 0$ , Eq. (4.7) reduces to Eq. (1.4). If the nematic is initially at rest and the director  $\mathbf{n}$  is driven by external forces (for instance by an optical field), then due to the coupling of Eqs. (4.1,4.7) a macroscopic flow can eventually appear. Such a flow that appears as a result of director reorientation is called backflow.

## 4.2 Adiabatic elimination of the flow field

From now on we assume that all physical quantities depend on  $(z, t)$  only. Then from Eq. (4.6) and the no-slip boundary conditions

$$\mathbf{v}|_{z=0,L} = 0 \quad (4.8)$$

one can immediately conclude that the  $z$  component of the velocity vanishes:

$$\mathbf{v} = (v_x(z, t), v_y(z, t), 0), \quad (4.9)$$

so  $\mathbf{v}$  is parallel to the plane of the layer. Moreover, all convective derivatives  $\mathbf{v} \cdot \nabla$  also vanish.

We may distinguish two time scales: one is the director relaxation time  $\tau$ , the other the momentum diffusion time  $\tau_{visc}$  which is associated with the relaxation of  $\mathbf{v}$

$$\tau = \frac{\gamma_1 L^2}{\pi^2 K_3}, \quad \tau_{visc} = \frac{\rho_m L^2}{\gamma_1}. \quad (4.10)$$

Typically  $\tau \sim 1s$  and  $\tau_{visc} \sim 10^{-6}s$ . Using the fact that  $\tau_{visc} \ll \tau$  the Navier-Stokes equation (4.1) can be considerably simplified as the velocity follows adiabatically the motion of the director. Thus the time derivatives  $\partial_t v_i$  in Eq. (4.1) can be neglected and the whole l. h. s. of Eq. (4.1) vanishes. In the absence of  $x, y$  dependence the only contributions to Eq. (4.1) come from  $j = z$ . Finally, taking into account that  $\pi_{xz} = \pi_{yz} = 0$  [see Eq. (4.2)] the following relations are obtained from Eq. (4.1):

$$\begin{aligned} -T_{xz}^{visc}(z, t) &= C_1(t) \\ -T_{yz}^{visc}(z, t) &= C_2(t), \end{aligned} \quad (4.11)$$

where  $C_1(t)$  and  $C_2(t)$  are functions that do not depend on  $z$  and will be fixed by the boundary conditions. The third equation following from Eq. (4.1) can be used to find the pressure  $p(z, t)$  but this is not of interest here. Straightforward calculations of  $T_{xz}^{visc}$  and  $T_{yz}^{visc}$  from Eqs. (4.3) together with Eqs. (4.11) give the following equations:

$$\begin{aligned} -T_{xz}^{visc}(z, t) &= [2\alpha_1 n_x^2 n_z^2 + (\alpha_5 - \alpha_2) n_z^2 + (\alpha_3 + \alpha_6) n_x^2 + \alpha_4] \frac{U}{2} + \\ & n_x n_y [2\alpha_1 n_z^2 + \alpha_3 + \alpha_6] \frac{V}{2} + \alpha_2 n_z \partial_t n_x + \alpha_3 n_x \partial_t n_z = C_1(t) \end{aligned} \quad (4.12)$$

$$\begin{aligned} -T_{yz}^{visc}(z, t) &= [2\alpha_1 n_y^2 n_z^2 + (\alpha_5 - \alpha_2) n_z^2 + (\alpha_3 + \alpha_6) n_y^2 + \alpha_4] \frac{V}{2} + \\ & n_x n_y [2\alpha_1 n_z^2 + \alpha_3 + \alpha_6] \frac{U}{2} + \alpha_2 n_z \partial_t n_y + \alpha_3 n_y \partial_t n_z = C_2(t), \end{aligned} \quad (4.13)$$

where  $U = \partial_z v_x$  and  $V = \partial_z v_y$ , and the explicit dependence of the variables on  $(z, t)$  is suppressed for brevity. Note that the equation for  $T_{yz}^{visc}$  can be obtained from the one for  $T_{xz}^{visc}$  by interchanging the indices  $x$  and  $y$ .

**Table 4.1.** Relationship between dimension and dimensionless quantities.

quantity	physical	dimensionless
length	$z$	$z\pi/L$
wavevector	$k_0$	$k_0L/\pi$
time	$t$	$t/\tau^a$
viscosity coefficients	$\alpha_i$	$\alpha_i/\gamma_1$
velocity	$\mathbf{v}$	$\mathbf{v}\pi\tau/L$

<sup>a</sup> $\tau$  is the director relaxation time defined in Eq. (4.10).

Next we consider the director equation (4.7). We write  $\mathbf{n}$  in terms of spherical angles  $\Theta$  and  $\Phi$ , see Eq. (2.1), and insert this into Eq. (4.7). Then, performing the same manipulations that lead to Eqs. (2.4) (see Sec. 2.1) and introducing dimensionless quantities according to Table 4.1 the following equations for  $\Theta$  and  $\Phi$  can be derived:

$$\partial_t \Theta + \mu (U \cos \Phi + V \sin \Phi) = \mathcal{L}_\Theta \quad (4.14)$$

$$\partial_t \Phi + \alpha_2 \cot \Theta (V \cos \Phi - U \sin \Phi) = \mathcal{L}_\Phi,$$

where  $\mu = \alpha_2 - \gamma_2 \sin^2 \Theta$  and  $\mathcal{L}_\Theta, \mathcal{L}_\Phi$  are given by Eqs. (2.5). Note that starting from Eqs. (4.14) all quantities will be dimensionless, although the same symbols for them have been kept (see Table 4.1).

After introducing the  $(\Theta, \Phi)$  representation in Eqs. (4.12,4.13) we use Eqs. (4.14) to eliminate the time derivatives of the director. Then the equations for the velocity gradients  $U, V$  can be written as:

$$\begin{pmatrix} g_1 & a \\ a & g_2 \end{pmatrix} \begin{pmatrix} U \\ V \end{pmatrix} + \begin{pmatrix} f_1 \\ f_2 \end{pmatrix} = \begin{pmatrix} C_1 \\ C_2 \end{pmatrix}, \quad (4.15)$$

where

$$\begin{aligned} 2g_1 &= g_{11} + g_{12} \cos^2 \Phi \\ 2g_2 &= g_{11} + g_{12} \sin^2 \Phi \\ 2a &= g_{12} \sin \Phi \cos \Phi. \end{aligned} \quad (4.16)$$

Here  $g_{11}, g_{12}$  depend on  $\Theta$  only:

$$\begin{aligned} g_{11} &= ([\alpha_5 - \alpha_2 - 2\alpha_2^2] \cos^2 \Theta + \alpha_4) \\ g_{12} &= (\alpha_5 - \alpha_2 \gamma_2 + 2[\alpha_1 + \gamma_2^2] \cos^2 \Theta) \sin^2 \Theta. \end{aligned} \quad (4.17)$$

Moreover

$$\begin{aligned} f_1 &= \mu \cos \Phi \mathcal{L}_\Theta - \frac{\alpha_2}{2} \sin \Phi \sin 2\Theta \mathcal{L}_\Phi \\ f_2 &= \mu \sin \Phi \mathcal{L}_\Theta + \frac{\alpha_2}{2} \cos \Phi \sin 2\Theta \mathcal{L}_\Phi. \end{aligned} \quad (4.18)$$

One can invert the matrix in Eqs. (4.15) and thus solve for  $U, V$ :

$$\begin{pmatrix} U \\ V \end{pmatrix} = \frac{1}{g_1 g_2 - a^2} \begin{pmatrix} g_2 (C_1 - f_1) - a (C_2 - f_2) \\ -a (C_1 - f_1) + g_1 (C_2 - f_2) \end{pmatrix}. \quad (4.19)$$

Next we use (4.19) to construct the linear combinations of  $U$  and  $V$  appearing in Eqs. (4.14):

$$\begin{aligned} U \cos \Phi + V \sin \Phi &= \frac{2}{g_{11} + g_{12}} \{C_1 \cos \Phi + C_2 \sin \Phi - \mu \mathcal{L}_\Theta\} \\ V \cos \Phi - U \sin \Phi &= \frac{1}{g_{11}} \{2(C_2 \cos \Phi - C_1 \sin \Phi) - \alpha_2 \sin 2\Theta \mathcal{L}_\Phi\}. \end{aligned} \quad (4.20)$$

Finally, we substitute Eqs. (4.20) into Eqs. (4.14) to eliminate  $U, V$  from the director equations:

$$\partial_t \Theta = \left[ 1 + \frac{2\mu^2}{g_{11} + g_{12}} \right] \mathcal{L}_\Theta - \frac{2\mu (C_1 \cos \Phi + C_2 \sin \Phi)}{g_{11} + g_{12}} \quad (4.21)$$

$$\partial_t \Phi = \left[ 1 + \frac{2\alpha_2^2 \cos^2 \Theta}{g_{11}} \right] \mathcal{L}_\Phi + \frac{2\alpha_2 \cot \Theta (C_1 \sin \Phi - C_2 \cos \Phi)}{g_{11}}. \quad (4.22)$$

Equations (4.21, 4.22) still contain the unknown quantities  $C_1(t), C_2(t)$ . They can be found by integrating Eqs. (4.19) with respect to  $z$  from 0 to  $\pi$  ( $z = \pi$  corresponds to  $z = L$  in normalized units). The integral of the left hand side

$$\int_0^\pi U dz = \int_0^\pi V dz = 0 \quad (4.23)$$

vanishes due to the boundary conditions Eqs. (4.8). Thus a set of linear equations for  $C_1, C_2$  is obtained. Then we write  $\Phi$  as  $\Phi = \Phi_0(t) + \Phi_d(z, t)$ , where  $\Phi_0(t)$  describes the pure rotation and  $\Phi_d(z, t)$  contains the rest [see Eq. (2.12)]. Straightforward calculations give the following expressions for the linear combinations of  $C_1, C_2$  needed in Eqs. (4.21), (4.22):

$$C_1 \cos \Phi + C_2 \sin \Phi = 2 \frac{[I_1(I_4 + I_5) - I_2 I_3] \sin \Phi_d + [I_2(I_4 - I_5) + I_1 I_3] \cos \Phi_d}{I_5^2 - I_3^2 - I_4^2} \quad (4.24)$$

$$C_1 \sin \Phi - C_2 \cos \Phi = 2 \frac{[I_2(I_4 - I_5) + I_1 I_3] \sin \Phi_d + [-I_1(I_4 + I_5) + I_2 I_3] \cos \Phi_d}{I_5^2 - I_3^2 - I_4^2}$$

with

$$\begin{aligned}
I_1 &= \int_0^\pi dz \left\{ \frac{\alpha_2 \sin 2\Theta \mathcal{L}_\Phi \cos \Phi_d}{2g_{11}} + \frac{\mu \mathcal{L}_\Theta \sin \Phi_d}{g_{11} + g_{12}} \right\}, \\
I_2 &= \int_0^\pi dz \left\{ \frac{\alpha_2 \sin 2\Theta \mathcal{L}_\Phi \sin \Phi_d}{2g_{11}} - \frac{\mu \mathcal{L}_\Theta \cos \Phi_d}{g_{11} + g_{12}} \right\}, \\
I_3 &= \int_0^\pi dz \frac{g_{12} \sin 2\Phi_d}{g_{11}(g_{11} + g_{12})}, \quad I_4 = - \int_0^\pi dz \frac{g_{12} \cos 2\Phi_d}{g_{11}(g_{11} + g_{12})}, \\
I_5 &= \int_0^\pi dz \frac{2g_{11} + g_{12}}{g_{11}(g_{11} + g_{12})}.
\end{aligned} \tag{4.25}$$

It is important that  $\Phi_0(t)$  drops out from Eqs. (4.24) and, as a consequence, from the director equations Eqs. (4.21, 4.22). Thus, in the case of circularly polarized light the statement about the invariance with respect to rotations around the  $z$ -axis (2.8) of the coupled director and field equations Eqs. (4.21, 4.22), (A.15) together with the boundary conditions (2.2), (2.7) remains intact when including backflow (as it must).

It should be noted that sometimes (for simplicity) the following unrealistic boundary conditions are used for the velocity gradients [61]

$$U|_{z=0,L} = V|_{z=0,L} = 0 \tag{4.26}$$

instead of (4.8) (so-called stress-free boundaries). One can immediately conclude in this case from Eqs. (4.12, 4.13) that  $T_{xz}^{visc}|_{z=0,L} = T_{yz}^{visc}|_{z=0,L} = 0$ . Equations (4.11) then give  $C_1 = C_2 = 0$ . Finally, the director equations Eqs. (4.21, 4.22) are considerably simplified and the backflow effect manifests itself just as a renormalization of the viscosity  $\gamma_1$ . However, such boundary conditions cannot be realized in a real experiment.

The procedure of adiabatic elimination of the velocity field from the director equations was used for instance when electrically driven twisted [62–65] or hybrid [66] nematic cells were studied. (There the procedure is simpler.) An electric field with a strength equal to several times the Fréedericksz threshold value was applied for some time to the layer [63], resulting in a stationary deformation. When the applied field was switched off, the director tilt angle became greater than  $\pi/2$  in the bulk before relaxing back to zero. Such an interesting phenomena (the so called "optical bounce") can be accounted for only if the backflow within the plane of the layer is taken into account. Another example of the use of the method of velocity elimination is the study of the electric-field-induced splay Fréedericksz transition [67].

### 4.3 Linear stability analysis of the basic state

The next step is to compare the results of the linear stability analysis around the homeotropic state for the cases with and without backflow. Similar to Sec. 2.2 we linearize Eq. (4.21) in  $\Theta$ . Using Eq. (2.9) we can write the linear part of  $\mathcal{L}_\Theta$  as

$$\mathcal{L}_\Theta = \partial_z^2(\Theta) + \rho \Theta. \quad (4.27)$$

Linearization of the terms proportional to  $C_1, C_2$  leads to the formula

$$C_1 \cos \Phi + C_2 \sin \Phi = -\frac{2I_2}{I_5}, \quad (4.28)$$

where  $I_2$  and  $I_5$  are the integrals defined in (4.25). In linear approximation they are given by

$$I_2 = -\frac{b}{2\alpha_2(1-b)} \int_0^\pi dz \mathcal{L}_\Theta, \quad I_5 = \frac{\pi b}{\alpha_2^2(1-b)} \quad (4.29)$$

with

$$b = \frac{2\alpha_2^2}{\alpha_4 + \alpha_5 - \alpha_2} = \frac{\alpha_2^2}{\eta_1} > 0. \quad (4.30)$$

Here  $\eta_1$  is a Miesowicz effective viscosity [37]. Thus, the right-handside of Eq. (4.28) is independent of  $\Phi$  which shows that  $\Phi$  does not appear in the linearized Eq. (4.21). This is a consequence of the fact that  $\Phi$  is not defined for the homeotropic state (see also Sec. 2.2). Finally, the linearized equation Eq. (4.21) has the form

$$(1-b) \partial_t(\Theta) = \mathcal{L}_\Theta - \frac{b}{\pi} \int_0^\pi dz \mathcal{L}_\Theta. \quad (4.31)$$

We look for solutions in the form

$$\Theta(z, t) = \Theta(z) e^{\sigma t}, \quad (4.32)$$

where  $\sigma$  is the growth rate and then obtain from Eqs. (4.27, 4.31)

$$\partial_z^2(\Theta(z)) + [\rho - \sigma(1-b)] \Theta(z) - \frac{b}{\pi} \int_0^\pi dz [\partial_z^2(\Theta(z)) + \rho \Theta(z)] = 0. \quad (4.33)$$

Taking into account the boundary conditions  $\Theta|_{z=0,\pi} = 0$ , Eq. (4.33) is solved by

$$\Theta = -\cos\left[\frac{\pi}{2}\delta\right] + \cos\left[\delta\left(\frac{\pi}{2} - z\right)\right], \quad (4.34)$$

**Table 4.2.** Viscosity coefficients for the nematic 5CB at  $T = 26^\circ\text{C}$  (see G. Ahlers in [16]).  $\alpha_6 = \alpha_2 + \alpha_3 + \alpha_5$  (Onsager relation).

viscosities	$\alpha_1$	$\alpha_2$	$\alpha_3$	$\alpha_4$	$\alpha_5$
in units					
of $\text{dyn} \cdot \text{s}/\text{cm}^2$	-0.066	-0.77	-0.042	0.634	0.624
normalized to $\gamma_1$	-0.091	-1.058	-0.058	0.871	0.857

where  $\delta(\rho)$  satisfies the transcendental equation

$$2b(\delta^2 - \rho) \sin \left[ \frac{\pi}{2} \delta \right] + \delta(b\rho - \delta^2) \cos \left[ \frac{\pi}{2} \delta \right] = 0 \quad (4.35)$$

and

$$\sigma = \frac{\rho - \delta^2}{1 - b}. \quad (4.36)$$

Noting that  $\rho = \delta = 1$  is a solution of Eq. (4.35) we expand the equation with respect to  $\delta$  and  $\rho$  around this point. To lowest order one finds:

$$\delta = 1 + \frac{4b(\rho - 1)}{\pi^2(1 - b) + 8b}. \quad (4.37)$$

Finally, the growth rate  $\tilde{\sigma} = \sigma/\tau$  in physical units can be written as:

$$\tilde{\sigma} = \frac{\rho - 1}{\tau\xi}, \quad (4.38)$$

where

$$\xi = (1 - b) \left( 1 + \frac{8}{\pi^2} \frac{b}{1 - b} \right) = 1 - \left( 1 - \frac{8}{\pi^2} \right) \frac{\alpha_2^2}{\eta_1} \simeq 1 - 0.19 \frac{\alpha_2^2}{\eta_1}. \quad (4.39)$$

One can see from Eq. (4.38) that the homeotropic state loses stability at  $\rho = 1$ . Equation (4.38) corresponds to Eq. (2.11) with  $\tau$  replaced by  $\tau\xi$ , or, equivalently,  $\gamma_1$  replaced by  $\gamma_1\xi$ . Thus within the linear stability analysis backflow results in a renormalization of the rotational viscosity  $\gamma_1$  (in fact a reduction).

In the calculations we took the viscosity coefficients for the nematic 5CB (see Table 4.2). For these parameters the value of  $\xi$  turns out to be  $\xi \simeq 0.85$ . It is worth noting that the use of the stress-free boundary conditions [see Eq. (4.26)] leads to a different factor  $\xi = 1 - b \simeq 0.20$  for the parameters used. Such a significant decrease of  $\gamma_1$  is incompatible with the experiments.

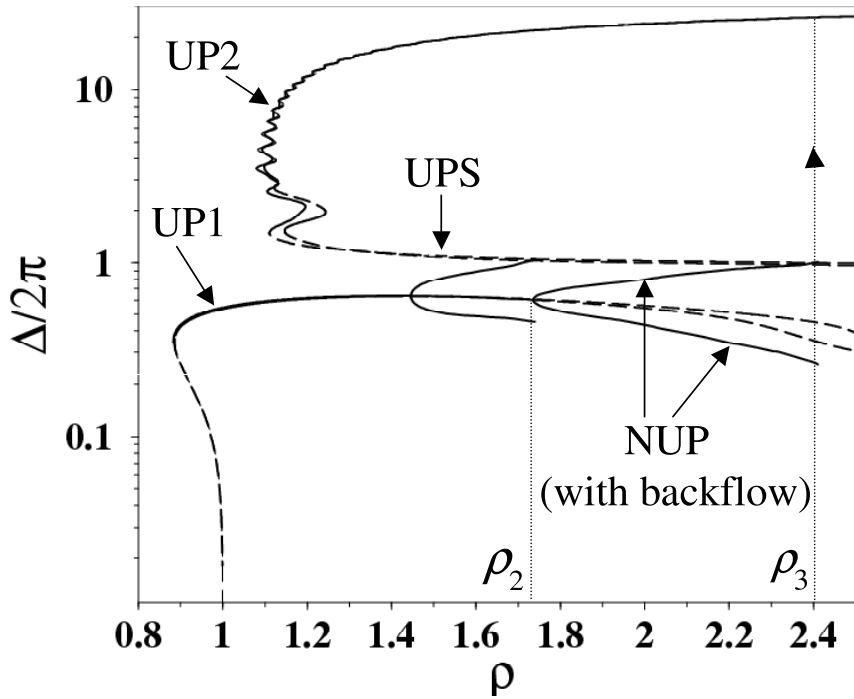


**Figure 4.1.**  $\Delta/2\pi$  versus  $\rho$  in logarithmic scale for the case with and without backflow. The latter case is also shown in Fig. 2.2(a). Solid (dashed) curves correspond to stable (unstable) solutions.

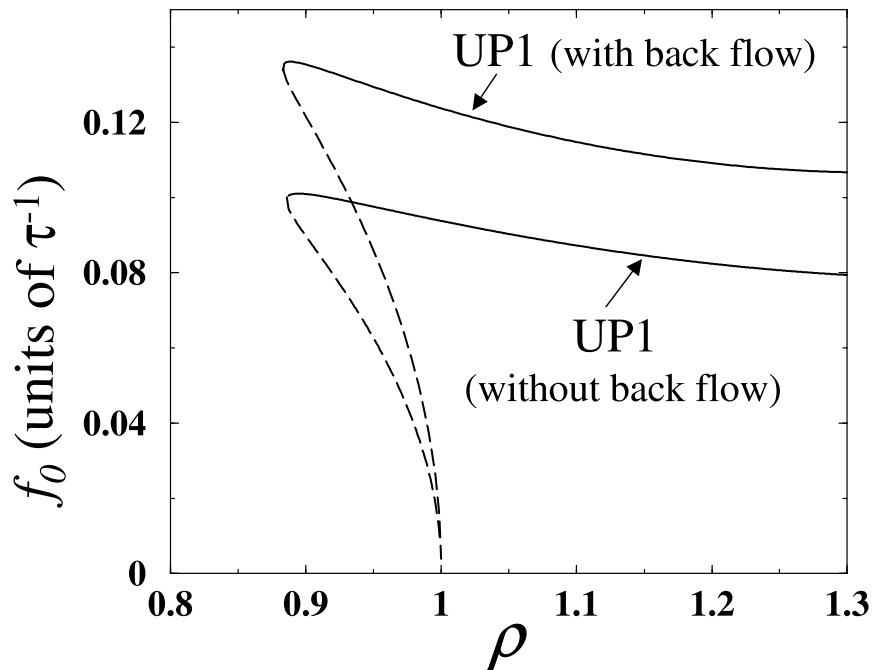


**Figure 4.2.** Precession frequency  $f_0$  versus  $\rho$  for the case with and without backflow. The latter case is shown in Fig. 2.5(a). Solid (dashed) curves correspond to stable (unstable) solutions.

## 4.4 Simulations

In order to investigate the full bifurcation scenario reported in Chapter 2 we simulated the system of coupled nematodynamic equations after the elimination of the velocity gradients from the director equations that consist of i) director equations (4.21, 4.22) with the boundary conditions (2.7); ii) light field equations (A.15) with the boundary conditions (2.2). For this purpose we expand  $\Theta$  and  $\Phi$  with respect to the trial functions (2.12) and perform the projection procedure described in Sec. 2.3 that eventually leads to a set of coupled ODE's for the modes  $\Theta_n, \Phi_n$  [see also Eqs. (2.15)]. We then solved the ODEs using the Runge-Kutta method as was done before. It should be noted that the procedure of numerical integration becomes more complicated compared to the case without backflow because of the appearance of the integrals (4.25) that have to be evaluated at each time step.

In Fig. 4.1 the phase delay  $\Delta$  versus  $\rho$  is shown for the case with and without flow. Clearly  $\Delta$  remains almost the same in the regimes with uniform director precession (UP1, UP2). However, the regime of nonuniform director precession (NUP) shifts to higher intensities. The thresholds for the NUP and for the UP2 regimes (see Sec. 2.4) turns out to be  $\rho_2 = 1.74$  and  $\rho_3 = 2.4$  instead of  $\rho_2 = 1.45$  and  $\rho_3 = 1.75$  reported in Chapter 2. Thus the backflow leads to a quantitative change of the bifurcation scenario. In Fig. 4.2 the precession frequency  $f_0$  versus  $\rho$  is shown for the case with and without backflow. The backflow results in an increase of  $f_0$  because  $\gamma_1$  effectively decreases.

After integrating Eqs. (4.20) with respect to  $z$ , the expressions for the velocity components can be easily found. In Fig. 4.3 typical profiles for the velocity component  $v_x$  versus  $z$  (in normalized units) are shown for a UP1, UP2 and NUP state. One can see that the amplitude of the velocity in the NUP regime is significantly larger than that for the UP1 regime.

An interesting and, at first sight, surprising fact is, that for the UP2 state,  $v_x$  oscillates fairly rapidly across the cell. The reason is that the interference structure of  $o$  and  $e$  light for UP2 states leads to an oscillating behavior of the electric part of the torque [see the last term in Eq. (2.5) for  $\mathcal{L}_\Phi$ ] resulting in a similar structure in  $\partial_z \Phi$  [see Eq. (2.28)]. Since  $\mathcal{L}_\Phi$  also appears in the expressions for the velocity gradients (4.20), it leads to a similar behavior of  $v_x$ . This is valid only if  $\Delta = \alpha(\pi)$  is large as is the case for the UP2 states. For instance  $\Delta/2\pi \simeq 22.5$  for  $\rho = 1.81$ , see Fig. 4.1. The director profiles, however, do not exhibit such an oscillatory behavior but are characterized by an abrupt change of the derivatives at some points. Since in the UP1 and NUP regimes  $\Delta$  is always less than  $2\pi$  the velocity field changes sign of most one time.

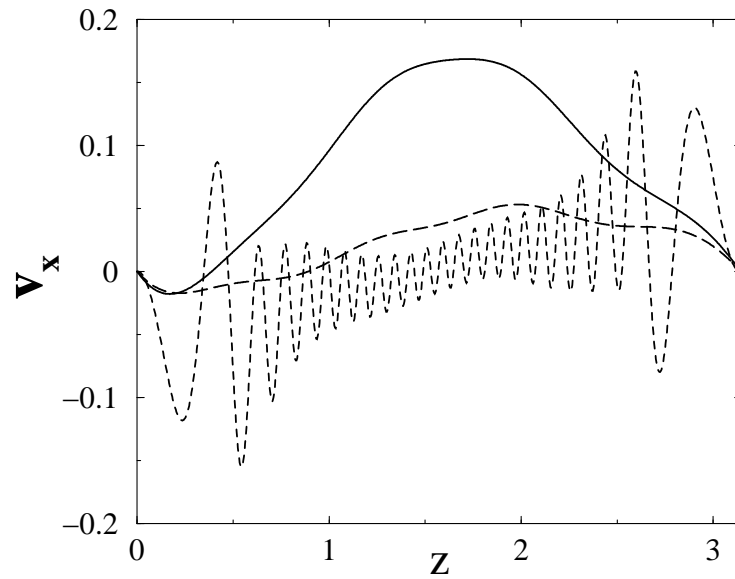


**Figure 4.3.** Profiles of  $v_x$  inside the cell at some time  $t$  when  $v_x$  is maximal. Long-dashed line: UP1 state ( $\rho = 1.70$ ). Solid line: NUP state ( $\rho = 1.81$ ). Dashed line: UP2 state ( $\rho = 1.81$ ). The dimensionless velocity  $v_x \simeq 0.2$  corresponds to  $1 \mu\text{m/s}$ .

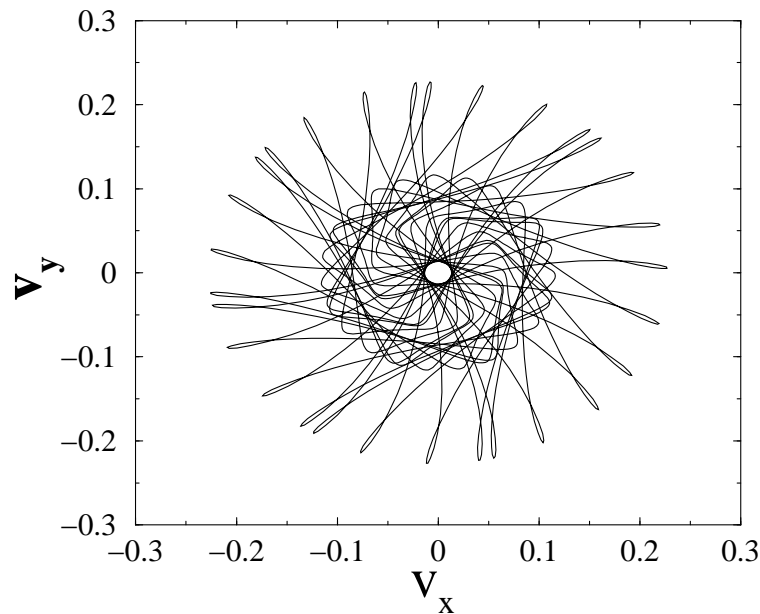


**Figure 4.4.** Typical phase portrait in the  $(v_x, v_y)$  plane for NUP regime ( $\rho = 1.90$ ) at some fixed values of  $z$  (not at the middle of the cell).

In Fig. 4.4 the phase portrait in the  $(v_x, v_y)$  plane for the NUP regime is shown. This trajectory is not closed because the flow (as the director) is characterized by two frequencies  $f_0$  (precession) and  $f_1$  (nutaton) as for the case without backflow. It should be pointed out that the time average of  $v_x$  and  $v_y$  is zero because we do not have an external flow.

## 4.5 Discussion

In this chapter we have shown the influence of the backflow effect on the director dynamics when driven by circularly polarized light. For this purpose we have performed a linear stability analysis around the basic state in order to assess the viscosity reduction factor. Then we have simulated the full set of nematodynamic equations and demonstrated that backflow leads to quantitative changes in the dynamical scenario. It turns out that the regime of nonuniform precession shifts to higher light intensities and exists in a larger interval. However, the experimental values of the thresholds  $\rho_2$ ,  $\rho_3$  are even smaller than that given by the theory without backflow. We believe that the discrepancy between the theoretical predictions and the experiment is mainly due to the fact that in the experiments one was far away from realizing the large-aspect ratio case (the beam size was of the order of the layer thickness). Hopefully, in future experiments with large-aspect ratio systems our predictions will be tested quantitatively. We have found an anticipated spatial oscillation of the backflow in the UP2 regime. It results from spatial oscillations of the director twist  $\partial_z \Phi$ , which are a consequence of oscillations in the torque resulting from interference phenomena between ordinary and extraordinary light. The structure in the director twist is present also when backflow is neglected, i.e. in the calculation of Chapter 2. Backflow acts as a sensitive diagnostic to detect it.

# Chapter 5

## Pattern forming instability induced by light in pure and dye-doped nematics

In this chapter a theoretical study of the instabilities induced by a linearly polarized ordinary light wave incident at a small oblique angle on a thin layer of homeotropically oriented nematic liquid crystal with special emphasis on the dye-doped case will be discussed. The spatially periodic Hopf bifurcation that occurs as the secondary instability after the stationary Fréedericksz transition is analyzed.

### 5.1 Basic state

We consider a linearly-polarized plane wave incident at a small oblique angle  $\beta_0$  on a layer of dye-doped nematic LC which has initially homeotropic alignment. The light is polarized along the  $y$ -axis i.e., we deal with an ordinary wave. We introduce the angles  $\theta(z, t)$  and  $\varphi(z, t)$  (see Fig. 5.1) so that

$$\mathbf{n} = (\sin \theta, \cos \theta \sin \varphi, \cos \theta \cos \varphi). \quad (5.1)$$

We substitute into the Eqs. (1.6,1.7) the expression (5.1) for the director to derive a set of two PDEs for  $\theta, \varphi$ . These equations are presented explicitly in Appendix B.

It is easily seen from Eqs. (1.16-1.17) that in the undistorted LC ( $\theta = \varphi = 0$ ) the light maintains its polarization inside the layer, so that we have only a nonzero  $y$ -component of the electric field  $E_{0y}$  that obeys the equation:

$$\partial_z^2 E_{0y} + k_0^2(\varepsilon_\perp + i\gamma_\perp - s_0^2)E_{0y} = 0. \quad (5.2)$$

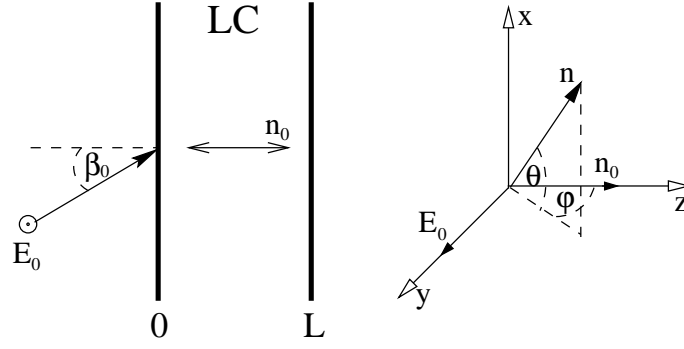


**Figure 5.1.** Geometry of the setup: linearly polarized light along the  $\mathbf{y}$ -direction incident at angle  $\beta_0$  on a nematic LC layer with the director  $\mathbf{n}_0 \parallel \mathbf{z}$  (homeotropic state). The components of the director  $\mathbf{n}$  are described in terms of the angles  $\theta, \varphi$  ( $\theta = \varphi = 0$  in the homeotropic state).

The solution of this equation is given by

$$E_{0y}(z) = E_0 e^{ik_z z}, \quad (5.3)$$

where  $E_0$  is the amplitude of the incident electric field and

$$k_z = k_{Re} + ik_{Im} \simeq k_0 \sqrt{\varepsilon_\perp - s_0^2} + \frac{i\gamma_\perp k_0}{2\sqrt{\varepsilon_\perp - s_0^2}}. \quad (5.4)$$

The terms of the order of  $[\gamma_\perp/(\varepsilon_\perp - s_0^2)]^2$  in  $k_z$  are neglected because  $\gamma_\perp \ll \varepsilon_\perp$ . We will examine the case  $\xi_{eff} > 0$  (the factor appearing before the optical torque) so that the preferred orientation corresponds to the director parallel to the electric field  $\mathbf{n} \parallel \mathbf{E}$ . Since in our geometry initially  $\mathbf{n} \perp \mathbf{E}$ , the homeotropic state will cease to be stable above some critical intensity of the incident light. The reorientation of the LC then leads to modification of the electric field polarization inside the LC.

## 5.2 Linearization of the equations around the basic state

As can be shown from Eqs. (B.1,B.2) in the linear approximation  $\theta$  remains zero and the linearized equation of motion for  $\varphi(z, t)$  has the following simple form:

$$\gamma_1 \partial_t \varphi = K_3 \partial_z^2 \varphi + \frac{(\varepsilon_a + \zeta)}{16\pi} (2 |E_{0y}|^2 \varphi + E_{1z}^* E_{0y} + E_{1z} E_{0y}^*), \quad (5.5)$$

where  $E_{1z}$  is the  $z$ -component of the field that perturbed by director reorientation (calculated to first order in  $\varphi$ ). Straightforward calculations yield the following equation

for  $E_{1z}(z)$  from Eqs. (1.16-1.17):

$$(\varepsilon_{\parallel} + i\gamma_{\parallel}) \frac{d^2 E_{1z}}{dz^2} + k_0^2 (\varepsilon_{\perp} + i\gamma_{\perp}) (\varepsilon_{\parallel} + i\gamma_{\parallel} - s_0^2) E_{1z} + (\varepsilon_a + i\gamma_a) \frac{d^2 (\varphi E_{0y})}{dz^2} + \quad (5.6)$$

$$k_0^2 (\varepsilon_a + i\gamma_a) (\varepsilon_{\perp} + i\gamma_{\perp}) \varphi E_{0y} = 0.$$

Substituting  $E_{1z}(z)$  into Eq. (5.6) in the form

$$E_{1z}(z) = E(z) e^{ik_z z}, \quad (5.7)$$

with  $k_z$  given by (5.4) and taking into account that  $k_0 L \gg 1$  ( $L$  is the width of the layer), a first-order ODE for  $E(z)$  that varies slowly with  $z$  on the scale  $k_0^{-1}$  can be derived:

$$y_2 \partial_z E(z) + y_3 E(z) + y_1 \partial_z \varphi(z) + y_3 E_0 \varphi(z) = 0, \quad (5.8)$$

where

$$y_1 = \frac{i}{\sqrt{\varepsilon_{\perp}}} \left\{ 2(\varepsilon_a + i\gamma_a) \varepsilon_{\perp} - \varepsilon_a \gamma_{\perp} - \left( \varepsilon_a + i \left[ \gamma_a - \frac{\varepsilon_a \gamma_{\perp}}{2\varepsilon_{\perp}} \right] \right) s_0^2 \right\} \quad (5.9)$$

$$y_2 = y_1 + \sqrt{\varepsilon_{\perp}} (2i\varepsilon_{\perp} - 3\gamma_{\perp}) + \frac{(\gamma_{\perp} - 2i\varepsilon_{\perp}) s_0^2}{2\sqrt{\varepsilon_{\perp}}}, \quad y_3 = k_0 (\varepsilon_a + i\gamma_a) s_0^2.$$

The terms with second derivatives  $\partial_z^2 E(z)$  and  $\partial_z^2 \varphi(z)$  appear without the prefactor  $k_0$  and can be neglected. This approximation corresponds to the so-called Geometric Optics Approximation [2]. In (5.9) only the linear terms in  $\gamma_a, \gamma_{\perp}$  and the terms up to  $s_0^4$  were kept ( $\gamma_a, \gamma_{\perp} \ll 1, s_0^4 \ll 1$ ). Keeping in mind that  $E(0) = 0$  and  $\varphi(0) = 0$  we derived the following equation for  $E(z)$ :

$$E(z) = -\frac{y_1 E_0}{y_2} \varphi(z) + \frac{(y_1 - y_2) y_3 E_0}{y_2^2} \int_0^z e^{y_3/y_2(z'-z)} \varphi(z') dz'. \quad (5.10)$$

Finally the real part of  $E(z)$  can be found from Eq. (5.10):

$$\begin{aligned} \text{Re}[E(z)] &= \frac{E_0}{\varepsilon_a + \varepsilon_{\perp}} \times \quad (5.11) \\ &\left\{ -\varepsilon_a \varphi(z) + \frac{\pi \kappa}{L} \varepsilon_{\perp} \int_0^z \left[ \psi \cos\left(\frac{\pi \kappa}{L}(z' - z)\right) + \sin(\kappa(z' - z)) \right] e^{(\pi/L)\xi \kappa(z' - z)} \varphi(z', t) dz' \right\}, \end{aligned}$$

where the coefficients  $\psi, \xi, \kappa$  are defined as:

$$\begin{aligned} \psi &= -\frac{\varepsilon_a^2 \gamma_{\perp} - 3\varepsilon_a \varepsilon_{\perp} \gamma_{\perp} + 2\gamma_a \varepsilon_{\perp}^2 - 2\gamma_a \varepsilon_{\perp} \varepsilon_a}{2(\varepsilon_a + \varepsilon_{\perp}) \varepsilon_a \varepsilon_{\perp}}, \quad \xi = \frac{2\gamma_a \varepsilon_{\perp}^2 - 3\varepsilon_a \varepsilon_{\perp} \gamma_{\perp} - \varepsilon_a^2 \gamma_{\perp}}{2(\varepsilon_a + \varepsilon_{\perp}) \varepsilon_a \varepsilon_{\perp}}, \\ \kappa &= \frac{L}{\pi} \frac{s_0^2 \varepsilon_a k_0}{2\sqrt{\varepsilon_{\perp}} (\varepsilon_{\perp} + \varepsilon_a)}. \quad (5.12) \end{aligned}$$

One can see from Eq. (5.12) that the coefficients  $\psi$  and  $\xi$  appear because of the absorption of the dye only and they vanish for the case of a pure LC.  $\kappa\pi$  is (to a very good approximation) the phase shift between the ordinary and the extraordinary wave induced by the layer in the undisturbed homeotropically aligned LC.

We may now rewrite Eq. (5.5) in terms of  $Re[E(z)]$  taking into account Eq. (5.3) for  $E_{0y}$ , Eq. (5.4) for  $k_z$  and Eq. (5.7) for  $E_{1z}$ :

$$\gamma_1 \partial_t \varphi(z, t) = K_3 \partial_z^2 \varphi(z, t) + \frac{(\varepsilon_a + \zeta) E_0^2 e^{-2k_{Im}z}}{8\pi} \left\{ \varphi(z, t) + \frac{Re[E(z)]}{E_0} \right\}. \quad (5.13)$$

Substituting the expression for  $Re[E(z)]$  [see Eq. (5.11)] into Eq. (5.13) the following integro-differential equation for  $\varphi$  can be derived:

$$\begin{aligned} \tau \partial_t \varphi(z, t) = & \left( \frac{L}{\pi} \right)^2 \partial_z^2 \varphi(z, t) + \rho \left\{ \left( \frac{\pi\kappa}{L} \right) \int_0^z \left[ \psi \cos \left( \frac{\pi\kappa}{L} (z' - z) \right) + \sin \left( \frac{\pi\kappa}{L} (z' - z) \right) \right] \right. \\ & \left. \times e^{\frac{\pi}{L} \xi \kappa (z' - z)} \varphi(z', t) dz' + \varphi(z, t) \right\} e^{-2k_{Im}z}, \end{aligned} \quad (5.14)$$

where the parameter  $\tau$  is the characteristic time of the director motion defined as:

$$\tau = \frac{\gamma_1 L^2}{\pi^2 K_3} \quad (5.15)$$

and  $\rho$  is the normalized intensity given by:

$$\rho = \frac{I}{I_l}, \quad \text{with } I_l = \frac{\pi^2 c(\varepsilon_{\perp} + \varepsilon_a) K_3}{L^2 \varepsilon_a \sqrt{\varepsilon_{\perp} \eta}}, \quad \eta = \frac{\varepsilon_a + \zeta}{\varepsilon_a}, \quad (5.16)$$

where  $I$  is the intensity of the incident light.

For perpendicular incidence and for a pure nematic [ $\eta = 1$ ,  $\gamma_{\perp} = \gamma_{\parallel} = 0$ ] Eq. (5.14) reduces to:

$$\tau \partial_t \varphi(z, t) = \left( \frac{L}{\pi} \right)^2 \partial_z^2 \varphi(z, t) + \rho \varphi(z, t). \quad (5.17)$$

Taking into account that Eq. (5.17) has the same form as Eqs. (2.9) [except in former case it is not normalized] one can conclude that the basic state loses stability at  $\rho = 1$  [see also Eq. (2.11)]. Thus  $I_l$  [see Eq. (5.16)] for  $\eta = 1$  coincides with the threshold intensity of the LIFT for a pure nematic at perpendicular incidence [2].

Note that for a pure nematic Eq. (5.14) reduces to the one obtained in [68].

### 5.3 Approximate stability analysis of the basic state

We use a two-mode expansion with respect to  $z$  for the angle  $\varphi(z, t)$  with the boundary conditions  $\varphi(z = 0) = \varphi(z = L) = 0$ :

$$\varphi(z, t) = A_1(t) \sin\left(\frac{\pi z}{L}\right) + A_2(t) \sin\left(\frac{2\pi z}{L}\right), \quad (5.18)$$

where  $A_1$  and  $A_2$  are time-dependent amplitudes. This is motivated by the fact that the distorted state is asymmetric with respect to the center of the layer because of absorption and the perturbation of the light polarization inside the layer. Therefore we have to include at least one mode that is symmetric and one mode that is antisymmetric with respect to the center of the layer. After projecting Eq.(5.14) onto the trial functions we have a system of two equations for the modes  $A_1$  and  $A_2$ :

$$\tau \frac{dA_1}{dt} = \Lambda_{11}A_1 + \Lambda_{12}A_2, \quad \tau \frac{dA_2}{dt} = \Lambda_{21}A_1 + \Lambda_{22}A_2, \quad (5.19)$$

where the elements of the matrix  $\Lambda_{ij}$  depend on the material parameters and the control parameters  $\rho$  and  $\kappa$  (which is proportional to  $s_0^2$ ). The procedure of deriving  $\Lambda_{ij}$  is straightforward and the expressions for the  $\Lambda_{ij}$  are presented in the Appendix C.

We look for solutions proportional to  $\exp(\sigma t)$ , where  $\sigma$  is the growth rate defined as follows:

$$\sigma = \frac{\text{Tr}(\Lambda) \pm \sqrt{\text{Tr}^2(\Lambda) - 4 \det(\Lambda)}}{2}. \quad (5.20)$$

The basic state is stable for  $\text{Re}(\sigma) < 0$ . The stability diagram in the  $(\kappa, \rho)$  plane can now be calculated for any given set of material parameters of the LC. As an example we consider the nematic 5CB doped with the dye AD1 at 0.1% concentration. We used the following values of material parameters at the temperature  $T = 24^\circ$ :  $\alpha_o = 42 \text{ cm}^{-1}$ ,  $n_o = 1.53$ ,  $\alpha_e = 190 \text{ cm}^{-1}$ ,  $n_e = 1.71$ , (absorption coefficients and refractive indices of the ordinary and extraordinary light, respectively),  $\lambda = 633 \text{ nm}$  (wavelength of laser),  $\zeta = 58$  [22],  $\gamma = 0.845 \text{ dyn} \cdot \text{s}/\text{cm}^2$ ,  $K_1 = 0.64 \cdot 10^{-6} \text{ dyn}$ ,  $K_2 = 0.42 \cdot 10^{-6} \text{ dyn}$ ,  $K_3 = 0.86 \cdot 10^{-6} \text{ dyn}$  (see G. Ahlers in [16]); the calculations are made for a layer thickness of  $50 \text{ }\mu\text{m}$ . For these parameters  $I_l = 33.21 \text{ W}/\text{cm}^2$ ,  $\tau = 2.49 \text{ s}$ .

The stability diagram is depicted in Fig. 5.2. The solid line corresponds to a pitchfork bifurcation ( $\det\Lambda(\kappa, \rho) = 0$  while  $\text{Tr}\Lambda(\kappa, \rho) < 0$ ), and the dashed one corresponds to a Hopf bifurcation of the homeotropic state ( $\text{Tr}\Lambda(\kappa, \rho) = 0$  while  $\det\Lambda(\kappa, \rho) > 0$ ). These lines divide the  $(\kappa, \rho)$  plane into a stable and an unstable region of the homeotropic alignment. They join in a so-called Takens-Bogdanov point where  $\det[\Lambda(\kappa, \rho)] =$

$Tr[\Lambda(\kappa, \rho)] = 0$ . The approximate value of this point for the pure nematic is  $\kappa_{TB} = 2/\sqrt{13}$ ,  $\rho_{TB} = 13/5$  (see [34]). For the dye-doped nematic this value depends on absorption and is given by an approximate formula Eq. (C.3). For the layer thickness and material parameters given above this value is  $\kappa_{TB} \simeq 0.6$ ,  $\rho_{TB} \simeq 3$ .

At this point it is interesting to note that the homeotropic state represents a stable node in region I where  $[Tr\Lambda(\kappa, \rho)]^2 > 4 det\Lambda(\kappa, \rho)$  with  $Tr\Lambda(\kappa, \rho) < 0$  and a stable focus in region II where  $[Tr\Lambda(\kappa, \rho)]^2 < 4 det\Lambda(\kappa, \rho)$  with  $Tr\Lambda(\kappa, \rho) < 0$ . In region III the homeotropic state is unstable [see Fig. 5.2a)].

There are two differences compared to the case of a pure LC. First, the enhancement of the orientational optical nonlinearity described by the parameter  $\zeta$  leads to a "renormalization" of the threshold intensity (see Eq. (5.16)). (However, since Fig. 5.2 is plotted with the renormalized threshold intensity, this fact alone would not change the stability diagram shown there). Second, absorption gives rise to attenuation of the field inside the nematic. This results in a shift of the line of primary instability to the region of higher intensities as is shown in Fig. 5.2b). From this figure one can see the quantitative difference between the case when the absorption is neglected (dashed-dot lines) and when the absorption is taken into account (solid and dashed lines). Note that the critical intensity  $\rho_{th}$  for perpendicular incidence thus becomes larger than 1.

We may expand  $\Lambda_{ij}^{pure}$  (see Appendix C.1) with respect to  $\kappa$  in order to get an approximate formula for the threshold  $\rho(\kappa)$  versus normalized angle  $\kappa$  for a case without absorption [see the dashed-dot lines in Fig. 5.2b)]. From the conditions  $det\Lambda = 0$  and  $Tr\Lambda = 0$  one can derive the intensity for the stationary and the Hopf bifurcation, respectively:

$$\rho_{st} = \frac{20 - 13\kappa^2 \pm \sqrt{3(4 - \kappa^2)(12 - 35\kappa^2)}}{2[4 - \kappa^2(1 - \kappa^2)]}, \quad \rho_H = \frac{20}{8 - \kappa^2}. \quad (5.21)$$

We can also find the approximate value of the threshold  $\rho_{th}$  for the case with absorption for perpendicular incidence due to the fact that then  $\Lambda_{ij}^{abs}$  is greatly simplified [see Eq. (C.2)]. In this case we have from Eq. (C.1):

$$\Lambda_{11} = -1 + (1 - \beta)\rho, \quad \Lambda_{12} = \Lambda_{21} = \frac{32\beta\rho}{9\pi^2}, \quad \Lambda_{22} = -4 + (1 - \beta)\rho, \quad (5.22)$$

where  $\beta = k_{Im}L$  [see Eq. (5.4)]. Eventually Eq. (5.22) leads to an approximate value for  $\rho_{th}$ :

$$\rho_{th} = \frac{5(1 - \beta) - \sqrt{9 - 18\beta + 25\beta^2}}{2(1 - 2\beta)}. \quad (5.23)$$

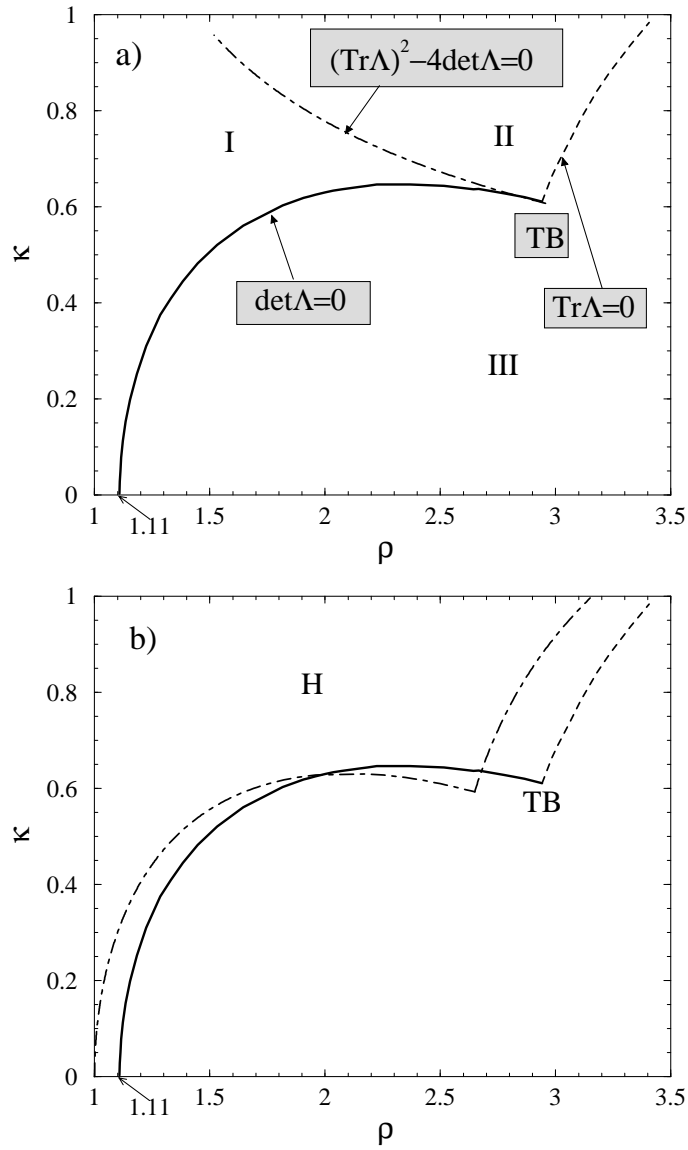


**Figure 5.2.** Stability diagram of the homeotropic in the  $(\kappa, \rho)$  plane.

a) Solid line  $[det\Lambda(\kappa, \rho) = 0]$ : stationary bifurcation;

dashed line  $[Tr\Lambda(\kappa, \rho) = 0]$ : Hopf bifurcation.

The dash-dotted line is defined by  $[Tr\Lambda(\kappa, \rho)]^2 - 4det\Lambda(\kappa, \rho) = 0$ .

I, II are the regions of stability of the homeotropic state.

III is the region where the homeotropic state is unstable.  $TB$  is the Takens-Bogdanov point  $[Tr\Lambda(\kappa, \rho) = det\Lambda(\kappa, \rho) = 0]$ .

b)  $H$  is the region of stability of the homeotropic state. Solid and dashed lines correspond to those in a). The dash-dotted lines are obtained when the absorption effect is neglected.

## 5.4 The stationary distorted state

After the homeotropic state loses stability via a stationary bifurcation (at not too large angle of incidence), the director settles in a stationary distorted state. It is determined by the second-order ODEs (B.1,B.2) for  $\theta(z)$  and  $\varphi(z)$  (now these angles can be of arbitrary magnitude) after inserting  $\partial_t\varphi = \partial_t\theta = 0$ .

These equations contain the field components which obey Maxwell's equations (1.17). It is convenient to write  $\bar{\Psi}(z)$  [see (1.18)] using the Oldano formalism developed for nonabsorbing anisotropic media [69]. In Appendix D we give a detailed description of this method. Finally we may expand  $\bar{\Psi}(z)$  as a combination of two vectors  $\bar{\alpha}_2$  and  $\bar{\alpha}_4$ , see (D.5), that correspond to forward propagating ordinary and extraordinary waves inside the homeotropically aligned LC, respectively

$$\bar{\Psi}(z) = b_2(z)e^{ik_0a_2z}\bar{\alpha}_2 + b_4(z)e^{ik_0a_4z}\bar{\alpha}_4 \quad (5.24)$$

and write the equations for the light propagation Eqs.(1.17) in terms of the amplitudes  $b_2(z)$  and  $b_4(z)$ :

$$\begin{cases} \frac{db_2}{dz} = \frac{ik_0}{N_2} [P_{22}(z)b_2 + b_4e^{-ik_0(a_2-a_4)z}P_{24}(z)] \\ \frac{db_4}{dz} = \frac{ik_0}{N_4} [P_{44}(z)b_4 + b_2e^{-ik_0(a_4-a_2)z}P_{42}(z)] \end{cases}, \quad (5.25)$$

where  $a_2, a_4, N_2, N_4$  and the functions  $P_{ij}(z)$  are given in (D.4), (D.8), and (D.13).

The advantage of the system (5.25) is that we now have only two equations for the "slow" amplitudes  $b_2(z)$  and  $b_4(z)$ . So, in total, we have a system of coupled ordinary differential equations for  $\theta(z)$ ,  $\varphi(z)$ ,  $b_2(z)$  and  $b_4(z)$  with boundary conditions  $\theta|_{z=0,L} = \varphi|_{z=0,L} = 0$ , and initial conditions for the incoming ordinary polarized light  $b_2|_{z=0} = A_0$ ,  $b_4|_{z=0} = 0$ . Here  $A_0$  can be related to the normalized intensity  $\rho$  defined by Eq. (5.16):

$$A_0 = \sqrt{\frac{8\pi^3 (\varepsilon_a + \varepsilon_\perp) (\varepsilon_\perp - s_0^2 + i\gamma_\perp) K_3\rho}{\varepsilon_a\varepsilon_\perp\eta L^2}}, \quad (5.26)$$

where  $\rho$  is the normalized intensity introduced in Eq. (5.16). The equations for  $\theta(z)$  and  $\varphi(z)$ , (B.1,B.2), contain the field combinations  $E_x E_x^*$  etc. that are related to the amplitudes  $b_2, b_4$  by Eqs. (D.14).

The system of "nematic+field" equations (with boundary conditions) is invariant under the transformation

$$[\theta, \varphi, E_x, E_y] \rightarrow [\theta, -\varphi, E_x, -E_y]. \quad (5.27)$$

owing to the reflection symmetry with respect to the  $y$  direction. Since the primary instability breaks this symmetry, two different distorted states exist, which are mutual images under this transformation. For perpendicular incidence of the light there is an additional reflection symmetry with respect to the  $x$  direction and, as a consequence, the system of equations is also invariant under the transformation

$$[\theta, \varphi, E_x, E_y] \rightarrow [-\theta, \varphi, -E_x, E_y]. \quad (5.28)$$

The system of equations can only be solved numerically. For this purpose we introduced the new variables  $d\theta/dz, d\varphi/dz$  to transform our set of equations to a system of six first-order equations. The main difficulty is that we have a "two point boundary value problem" not an "initial value problem". Thus we cannot simply start from some initial values at the beginning and just perform numerical integration to the end. To solve this system we used the "shooting method" from the NAG Fortran Library. The idea of this method is to transform the boundary value problem into an initial value one. In our case this means that the known values  $\theta|_{z=L} = \varphi|_{z=L} = 0$  at the second boundary  $z = L$  are substituted by estimated values  $d\theta/dz|_{z=0}, d\varphi/dz|_{z=0}$  at the first one. Then the "shooting" program improves these estimated values in such a way that finally the solution satisfies the known boundary conditions at  $z = L$ . To guarantee that we obtain the solution which connects smoothly with the homeotropic state we started with intensities only slightly above the threshold and tracked the solutions to larger  $\rho$  (for angles  $\beta_0$  for which there is a stationary bifurcation of the homeotropic state). It should be noted that the derivatives  $d\theta/dz, d\varphi/dz$  are supposed to be small quantities for the intensities close to the homeotropic threshold because the director profile is then weakly distorted (for the homeotropic state  $d\theta/dz|_{z=0} = d\varphi/dz|_{z=0} = 0$ ). This allows us to choose some small values for the derivatives as estimates and then the "shooting" program corrects them. As a control, different starting values for the derivatives were chosen, which led to the same corrected values of  $d\theta/dz|_{z=0}, d\varphi/dz|_{z=0}$ . Then, we increased  $\rho$  slightly and used the values of  $d\theta/dz|_{z=0}, d\varphi/dz|_{z=0}$  obtained in the previous step as an initial estimate. This procedure allowed us to derive the profiles  $\theta(z), \varphi(z), b_2(z)$  and  $b_4(z)$  for any  $\kappa$  and  $\rho$  above threshold.

As an example the director and field distributions are shown in Figs. 5.3 a) and b). The symmetrical solution can be obtained by the transformation (5.27).

## 5.5 Stability analysis of the stationary distorted state

Next we have performed a linear stability analysis of the distorted stationary state with respect to spatially periodic perturbations in the plane of the nematic layer. We

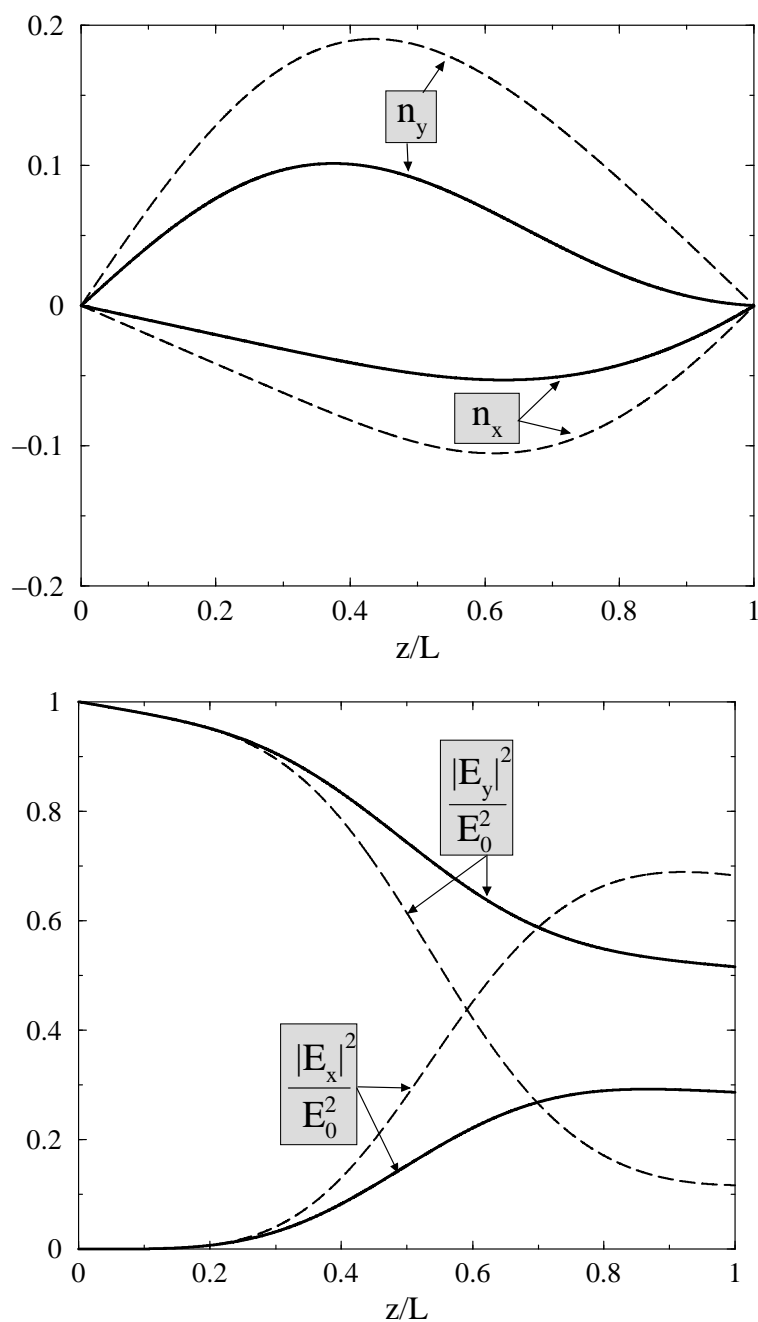


**Figure 5.3.** a) Profiles of the director components  $n_x$ ,  $n_y$  for the stationary distorted state.

b) Distortion of the field components inside the nematic layer for the stationary distorted state.  $E_z$  is small compared to  $E_x$ ,  $E_y$  and is not depicted;  $E_0$  is the amplitude of the incident electric field.

Solid lines:  $\beta_0 = 11^\circ$  ( $\kappa = 0.375$ ) and  $\rho = 2.0$ ;

Dashed lines:  $\beta_0 = 5^\circ$  ( $\kappa = 0.078$ ) and  $\rho = 1.49$ ;

write

$$\mathbf{n} = \mathbf{n}_0(z) + \delta\mathbf{n}(x, y, z, t) = \mathbf{n}_0(z) + \delta\mathbf{n}(z)e^{\sigma t + i(qx + py)}, \quad (5.29)$$

$$\bar{\Psi} = \bar{\Psi}_0 + \bar{\Psi}_1 = \sum_{k=2,4} (b_k(z) + \delta b_k(z)e^{\sigma t + i(qx + py)})e^{ik_0 a_k z} \bar{\alpha}_k,$$

where  $\delta\mathbf{n}$  and  $\delta b_k$  are small spatially periodic perturbations with wavenumbers  $q$  and  $p$ ;  $\sigma$  is the growth rate.

From the equation  $\mathbf{n}^2 = 1$  follows that  $\mathbf{n}_0 \delta\mathbf{n} = \mathbf{0}$ . Thus there are only two independent components of  $\delta\mathbf{n}$  and we expressed  $\delta n_z(z)$  in terms of the other components as:

$$\delta n_z(z) = -\frac{n_{0x}\delta n_x(z) + n_{0y}\delta n_y(z)}{n_{0z}}. \quad (5.30)$$

Substituting  $\mathbf{n} = \mathbf{n}_0(z) + \delta\mathbf{n}(x, y, z, t)$  into the expression for the free energy (1.3) and retaining the terms up to the second order in  $\delta\mathbf{n}$  the linear equations for  $\delta n_x(z)$  and  $\delta n_y(z)$  from Eqs. (1.4) have been obtained. These equations contain  $\delta n_x(z)$ ,  $\delta n_y(z)$  themselves, their  $z$  derivatives up to second order and  $\delta b_{2,4}(z)$  with complicated coefficients depending on the stationary distorted state  $\mathbf{n}_0(z)$ ,  $b_{2,4}(z)$  and wavenumbers  $q$  and  $p$ .

Also, we have decomposed the matrix  $\mathbf{D}_z$  [see (D.2)] as  $\mathbf{D}_z = \mathbf{D}_{z0} + \mathbf{D}_{z1}$ , where the matrix  $\mathbf{D}_{z0}$ , corresponds to the stationary state  $\mathbf{n}_0(z)$ , and the matrix  $\mathbf{D}_{z1}$  depends linearly on  $\delta\mathbf{n}$ . After linearization of Eqs. (5.25) [using the decomposed form of  $\mathbf{D}_z$ ] the equations for  $\delta b_{2,4}$  can be obtained:

$$\begin{cases} \frac{d(\delta b_2(z))}{dz} = \frac{ik_0}{N_2} \left( \delta b_2 P_{22}^{(0)} + \delta b_4 e^{ik_0(a_4 - a_2)z} P_{24}^{(0)} + b_2^{(0)} P_{22}^{(1)} + b_4^{(0)} e^{ik_0(a_4 - a_2)z} P_{24}^{(1)} \right) \\ \frac{d(\delta b_4(z))}{dz} = \frac{ik_0}{N_4} \left( \delta b_2 e^{ik_0(a_2 - a_4)z} P_{24}^{(0)} + \delta b_4 P_{44}^{(0)} + b_2^{(0)} e^{ik_0(a_2 - a_4)z} P_{24}^{(1)} + b_4^{(0)} P_{44}^{(1)} \right), \end{cases} \quad (5.31)$$

where  $b_2^{(0)}(z)$ ,  $b_4^{(0)}(z)$  are the field amplitudes for the stationary state. Here  $P_{kj}^{(0)} = \bar{\alpha}_k^T \mathbf{M} \mathbf{D}_{z0} \bar{\alpha}_j$  and  $P_{kj}^{(1)} = \bar{\alpha}_k^T \mathbf{M} \mathbf{D}_{z1} \bar{\alpha}_j$  are the matrix elements of  $\mathbf{D}_{z0}$  and  $\mathbf{D}_{z1}$  with respect to the eigenvectors (D.5) respectively, see (D.12).

It should be noted that the wavenumbers  $q$  and  $p$  appear only in the elastic part of the director equations and drop out of Eqs. (5.31). In the original Maxwell equations Eqs. (1.9) the field perturbations contain  $x, y$  dependence. However, neglecting the slow variations is a very good approximation because the corrections are of the order  $q/k_0$ ,  $p/k_0$  which are expected to be very small. This holds as long as the width of the layer is much larger than the wavelength of the light.

To solve the eigenvalue problem for  $\sigma$  we expand  $\delta n_{x,y}(z)$ ,  $\delta b_{2,4}(z)$  in terms of systems of functions which satisfy the boundary conditions.

For  $\delta \mathbf{n}$  the boundary conditions are  $\delta n_{x,y}|_{z=0,L} = 0$ , thus we write

$$\delta \mathbf{n} = \sum_k \mathbf{A}_k \sin\left(\frac{\pi k z}{L}\right). \quad (5.32)$$

Clearly the boundary conditions for the perturbations of the field amplitudes are  $\delta b_{2,4}|_{z=0} = 0$ . One can see that at  $z = 0, L$  the r.h.s. of the system (5.31) vanishes so one also has  $d(\delta b_{2,4})/dz|_{z=0,L} = 0$ . Therefore we used the expansion

$$\delta \mathbf{b} = \sum_n \mathbf{B}_n \sin^2\left(\frac{\pi n z}{2L}\right). \quad (5.33)$$

This set of functions is complete but not orthogonal. We also have to truncate these expansions to a finite number of modes.

After substituting the expansions (5.32, 5.33) into the system of equations for  $\delta \mathbf{n}$ ,  $\delta \mathbf{b}$  and projecting onto the modes (Galerkin method), the eigenvalue problem for  $\sigma$  becomes:

$$\mathcal{M}X = \sigma CX, \quad X = \begin{pmatrix} \mathbf{A} \\ \mathbf{B} \end{pmatrix}, \quad C = \begin{pmatrix} \mathbf{1} & 0 \\ 0 & 0 \end{pmatrix}, \quad (5.34)$$

where  $X$  is the vector of modes  $\mathbf{A}_n, \mathbf{B}_k$  and the matrix  $C$  is a block matrix.  $\mathbf{1}$  is the unit matrix whose dimension is equal to the sum of the number of modes taken for  $\delta n_x$  and  $\delta n_y$ . The matrix  $C$  appears on the r.h.s. of Eq. (5.34) because of the absence of time derivatives in Eqs. (5.31). Note that the matrix  $\mathcal{M}$  in Eq. (5.34) depends on the stationary state and on  $p, q$ .

We have solved the eigenvalue problem numerically to find the neutral surface  $\rho_0(q, p)$  (for given angle  $\beta_0$ ) which is defined by the condition  $Re(\sigma(q, p)) = 0$ . The number of Galerkin modes was chosen such that the accuracy of the calculated eigenvalues was better than 0.1% (we took six modes for  $\delta \mathbf{n}$  and forty modes for  $\delta \mathbf{b}$ ). The minimum of this surface gives the critical intensity  $\rho_c = \min_{q,p} \rho_0(q, p)$  and the critical wavevector  $(q_c, p_c)$ . Since  $\Omega_c = Im(\sigma)$  turned out to be nonzero at the minimum, the instability corresponds to a Hopf bifurcation. The branch of the secondary Hopf instability is depicted as the dash-dotted line in Fig. 5.4a) and for small angles of incidence in Fig. 5.4b).

It is interesting to note the following tendencies: as the incident angle  $\beta_0$  increases the critical intensity also increases, but the director and field deformations at the secondary

instability decrease. This is clearly demonstrated in Figs. 5.3 a), b) where the profiles of the director components  $n_x, n_y$  and field components  $E_x, E_y$  inside the nematic layer are shown for  $\beta_0 = 5^\circ$  and  $\beta_0 = 11^\circ$  for the values of  $\rho$  slightly below the secondary instability [see also Fig. 5.4 a)].

The dimensionless Hopf frequency  $\Omega_c \tau$  [ $\tau$  is defined in Sec. 5.2 by Eq. (5.15)] versus the normalized parameter  $\kappa$  [proportional to  $s_0^2$ , see Eq. (5.12)] is shown in Fig. 5.5. Figure 5.6 shows a typical contour plot of the neutral surface  $\rho_0(q, p)$ . The point  $(q_c L, p_c L)$  in this figure is the minimum of the surface and as is seen the bifurcation is inhomogeneous with critical vector  $(q_c, p_c) \neq 0$ . This means that travelling waves are expected to appear. However  $\rho_c$  is only slightly below the homogeneous threshold  $\rho_0(q = 0, p = 0)$ . The fact that  $(q_c, p_c) \neq 0$  is related to the broken reflection symmetry in the  $(x, y)$  plane and will be discussed below.

As was pointed out in Sec. 5.4, for nonzero  $\beta_0$  there are two symmetry-degenerate stationary distorted states. Clearly the two neutral surfaces are related by changing  $p$  to  $-p$  and the critical wave vectors will be  $(q_c, p_c)$  and  $(q_c, -p_c)$ . Thus two different travelling waves with critical vectors  $(q_c, \pm p_c)$  can be realized depending on which stationary state will be selected after the homeotropic state loses stability. It can also be pointed out that with a change of sign of the angle of incidence  $\beta_0 \rightarrow -\beta_0$ , the sign of  $q_c$  is also changed  $q_c \rightarrow -q_c$ .

An interesting situation arises in the limit of normal incidence. One might expect that for  $\beta_0 \rightarrow 0$  the wavenumber  $q_c \rightarrow 0$ , since in this limit the external symmetry breaking in the  $x$  direction vanishes. However, this turned out not to be the case. The reason is that then another stationary instability that spontaneously breaks the  $x$ -reflection symmetry intervenes the primary and the Hopf bifurcation. For the parameters of our computation one has  $\rho_{th} = 1.11$ ,  $\rho_{c1} = 1.13$  (point A in Fig. 5.4b) and  $\rho_{c2} = 1.17$  (point B in Fig. 5.4b)). One now has four symmetry-degenerate states and consequently four travelling waves with critical wave vectors  $(\pm q_c, \pm p_c)$ .

In Fig. 5.7 the  $n_x$  and  $n_y$  are shown versus  $\rho$  for perpendicular incidence and for  $\beta_0 = 0.5^\circ$  [for values of  $\rho$  lower than the Hopf bifurcation]. Note that the symmetrical solution can be obtained by the transformation (5.27) and for the perpendicular case in addition by (5.28). Thus, after the primary pitchfork bifurcation from the homeotropic to a stationary distorted state that breaks the  $y \rightarrow -y$  reflection symmetry, for perpendicular incidence we deal with another pitchfork bifurcation at  $\rho = \rho_{c1}$  which breaks  $x \rightarrow -x$  reflection symmetry. However this secondary pitchfork bifurcation is destroyed in the case of oblique incidence as is shown in Fig. 5.7. Such a behavior can be interpreted as an imperfect bifurcation [47] with respect to the angle

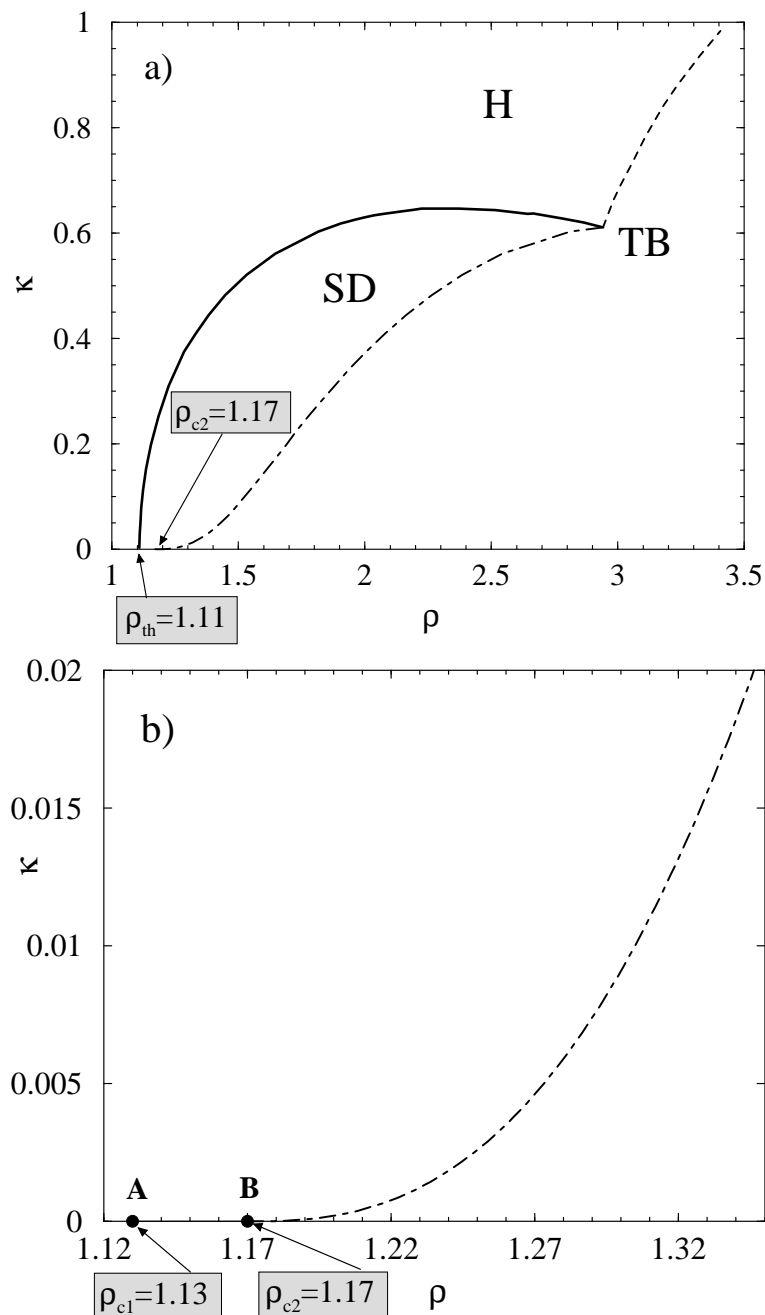


**Figure 5.4.** a) Stability diagram of the homeotropic and stationary distorted states in the  $(\kappa, \rho)$  plane.  $H$  is the region of the homeotropic state.  $SD$  is the region of the stationary distorted state bounded toward large  $\rho$  by the secondary Hopf bifurcation (dash-dotted line).  $TB$  is the Takens-Bogdanov point. b) The secondary instability for small angles of incidence. We show the instabilities of the stationary distorted state for perpendicular incidence of the light: A: pitchfork bifurcation to a state with  $n_x(z) \neq 0$ ; B: Hopf bifurcation.

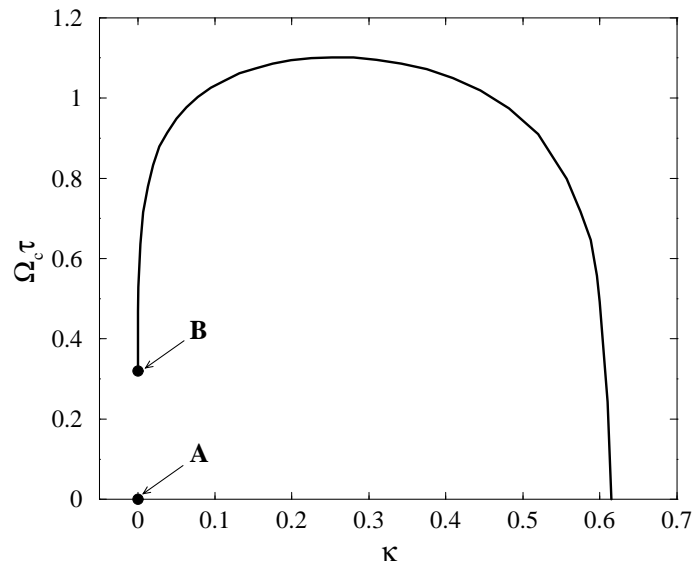


**Figure 5.5.** Dimensionless Hopf frequency  $\Omega_c \tau$  for the secondary instability versus  $\kappa$ . Points A and B are the Hopf frequencies at points A and B depicted in Fig. 5.4b).

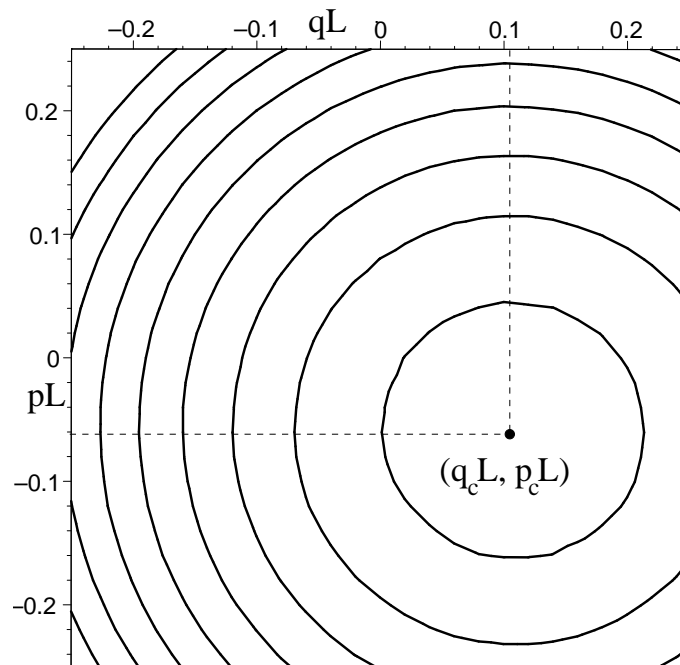


**Figure 5.6.** Contour lines for the surface  $\rho(p, q)$  correspond to  $\beta_0 = 11^\circ$  ( $\kappa = 0.375$ ). The critical intensity is  $\rho_c = 2.01$  with the critical wavevector  $(q_c L, p_c L) = (0.11, -0.06)$ ;  $\rho_0(q = 0, p = 0) - \rho_c = 1.5 \cdot 10^{-3}$ .

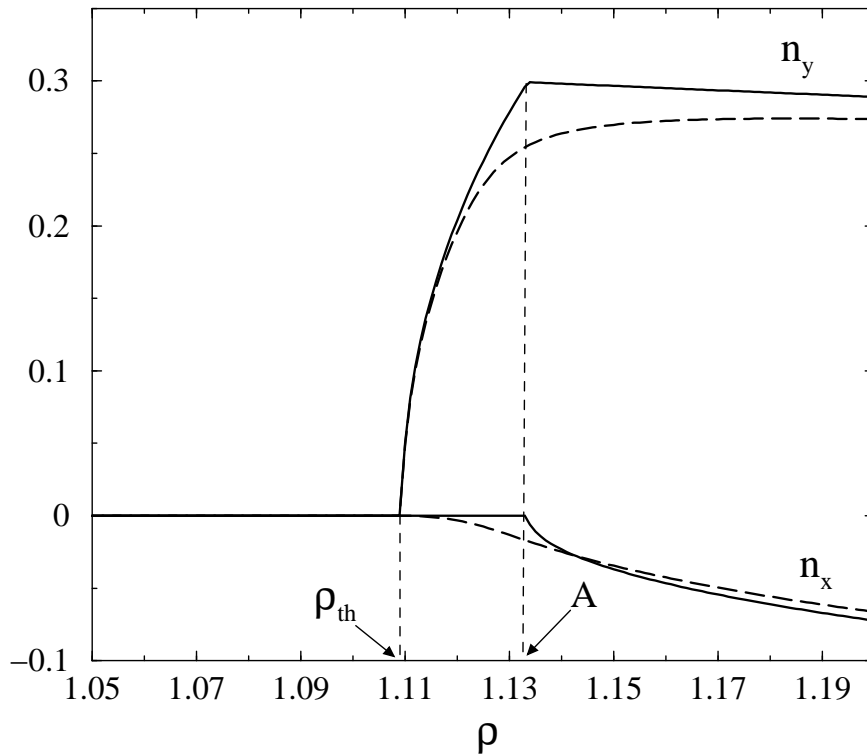


**Figure 5.7.** Profiles of the director components  $n_x$ ,  $n_y$  versus  $\rho$  at some  $z$  inside the layer (not at the middle). Solid and dashed lines correspond to  $\beta_0 = 0^\circ$  and  $\beta_0 = 0.5^\circ$  respectively.  $\rho_{th}$  is the threshold intensity of the LIFT. Point A has the same meaning as in Fig. 5.4b).

$\beta_0$  at  $\rho = \rho_{c1}$ .

In some further investigations we have changed the ratios between the elastic constants keeping other material parameters constant and saw the following tendency: for larger anisotropy of the constants the minimum of the surface becomes deeper and the critical wavenumbers become larger [see Fig. 5.8a,b)]. The error of the dimensionless critical wavenumbers  $q_c L, p_c L$  depicted in this figure is less than  $10^{-2}$ .

It can also be shown analytically that in the one-constant approximation ( $K_1 = K_2 = K_3$ ) the bifurcation is homogeneous [ $(q_c, p_c) = 0$ ] for any  $\kappa$ . This follows from the fact that then on the right-hand side of the director equations one has only terms proportional to  $(p^2 + q^2)\delta n_x$  and  $(p^2 + q^2)\delta n_y$ . As a consequence, the neutral surface  $\rho_0(q, p)$  becomes proportional to  $p^2 + q^2$ , so that the minimum is at  $(q_c, p_c) = 0$ . This result is completely general and is related to the fact that for  $K_1 = K_2 = K_3$  the orientational elasticity becomes isotropic [37].

From Fig. 5.8a,b) one can see that  $q_c L, p_c L \sim 0.1$ . This means that the period of the structure  $2\pi/q_c, 2\pi/p_c \sim 60L = 0.3 \text{ cm}$ . Thus in an experiment the spot size of the

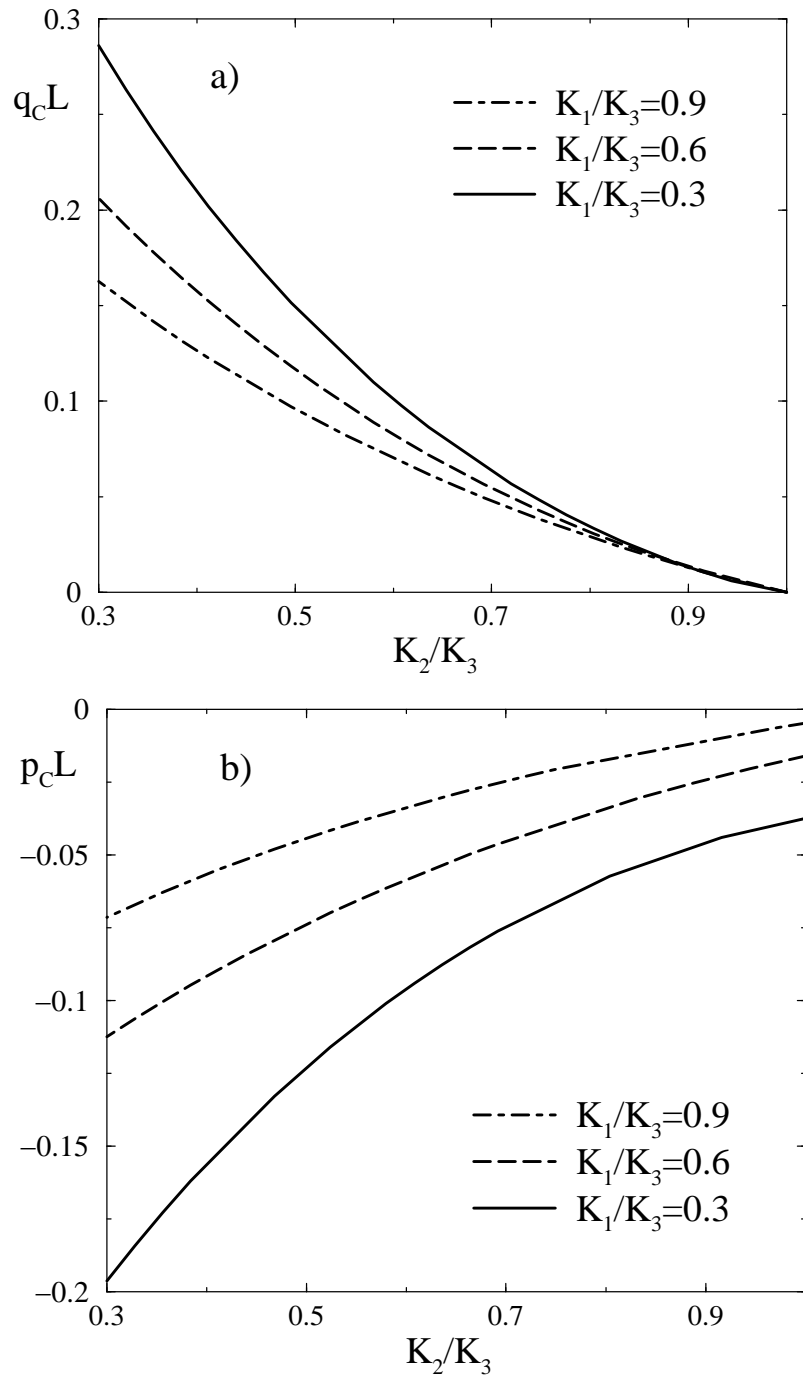


**Figure 5.8.** Critical wavenumbers  $q_c, p_c$  versus  $K_2/K_3$  for different ratios  $K_1/K_3$  ( $\beta_0 = 11^\circ$ ).

light must be rather large in order to observe the travelling waves.

## 5.6 Heating of the nematic due to the dye

An effect of light absorption during the light propagation in dye-doped nematic can cause significant heating of the LC if the intensity of the light is of the order of the LIFT threshold [18]. On the other hand, the material parameters of the nematic such as elastic constants are temperature dependent. Previously, we assumed that the nematic is maintained at constant temperature (under certain conditions) and took the material parameters for a fixed temperature. The question is whether such an assumption is reliable and can be realized in an experiment. To answer this question we have estimated the maximum temperature difference occurring *inside* the nematic 5CB doped with the dye AD1 from the steady-state heat conductivity equation. We considered a cell placed in a thermostage with a temperature  $T_0$  that consists of a nematic layer of a thickness  $L$ , sandwiched between two substrates of thickness  $d$ . We considered perpendicular incidence of the light (for simplicity) and assumed that absorption takes place only inside the nematic and is governed by the law:

$$I(z) = I_0 e^{-\alpha_{\perp}(z-d)}, \quad d \leq z \leq L + d. \quad (5.35)$$

Since we deal with the plane-wave approximation the following one-dimensional steady-state heat conductivity equations in the nematic and substrates can be written:

$$\kappa_s \partial_z^2 T = 0, \quad 0 \leq z \leq d \text{ or } L + d \leq z \leq L + 2d \quad (5.36)$$

$$\kappa_{\parallel} \partial_z^2 T = -\alpha_{\perp} I(z), \quad d \leq z \leq L + d,$$

where  $\kappa_{\parallel}$  is the parallel component of the heat conductivity tensor of the nematic and  $\kappa_s$  is the heat conductivity of the substrates. The solutions of Eqs. (5.36) are given by:

$$T_{s1} = C_1 z + T_0, \quad 0 \leq z \leq d \quad (5.37)$$

$$T_N = -\frac{I(z)}{\alpha_{\perp} \kappa_{\parallel}} + C_2 z + C_3, \quad d \leq z \leq L + d$$

$$T_{s2} = C_4 z + T_0, \quad L + d \leq z \leq L + 2d,$$

where  $T_{s1}$  ( $T_{s2}$ ) and  $T_N$  are the temperatures inside the first (second) substrates and nematic respectively. The unknown constants  $C_1, \dots, C_4$  can then be found from the

usual boundary conditions that are given by continuity conditions of the temperature and the heat flow at the substrate-nematic interfaces ( $z = d$  and  $z = L + d$ ):

$$T_{s1}|_{z=d} = T_N|_{z=d}, \quad \kappa_s \partial_z T_{s1}|_{z=d} = \kappa_{||} \partial_z T_N|_{z=d} \quad (5.38)$$

$$T_N|_{z=L+d} = T_{s2}|_{z=L+d}, \quad \kappa_{||} \partial_z T_N|_{z=L+d} = \kappa_s \partial_z T_{s2}|_{z=L+d}.$$

For the values of heat conductivities for the nematic we used  $\kappa_{||} = 3.0 \cdot 10^{-3} \text{ W}/^\circ\text{C cm}$  and for the glass substrates  $\kappa_{gl} = 1.1 \cdot 10^{-2} \text{ W}/^\circ\text{C cm}$  from [18]. The calculations were also performed for sapphire substrates ( $\kappa_{sap} = 0.4 \text{ W}/^\circ\text{C cm}$ ). We found that for the range of intensities  $I = 30 - 100 \text{ W}/\text{cm}^2$  the temperature difference inside the nematic is no more than a few Kelvins. In such a temperature range, the material parameters do not change very much so taking them to be constant across the layer is usually justified.

## 5.7 Discussion

Finally we remark on the behavior of the system in the nonlinear regime above the Hopf bifurcation. The system without transverse degrees of freedom has been studied previously, and various regimes of complex behavior have been discovered. The secondary bifurcation studied here marks the transition to simple periodic oscillations in the system without transverse degrees of freedom, which is the first step towards complex behavior. In models [33, 34] and simulations [70], a gluing bifurcation was found above the secondary Hopf bifurcation, which is a homoclinic bifurcation that restores the symmetry broken by the Fréedericksz transition. This gluing bifurcation was recently observed experimentally [36]. After this first gluing, complex nonlinear behavior and eventually chaos was observed in both theory, simulation and experiment [27].

The behavior of the system in the vicinity of the gluing bifurcation, can, however, be radically different from what was observed in the experiment [36]. In the spatially restricted system (i.e. the director oscillation induced by a narrow beam as observed in the experiments) one should observe stochastic behavior in the vicinity of the first gluing only as a consequence of experimental noise. It has been shown, however, [71, 72] that any spatially extended system, which possesses a homogeneous limit cycle (which is stable with respect to homogeneous perturbations) becomes unstable as it approaches a homoclinic bifurcation. This instability is either a phase instability, or a finite-wavelength period-doubling instability. On these grounds one can expect to observe very complicated behavior (probably spatio-temporal chaos) in our system already at

the threshold intensity of the first gluing. This then would be true deterministic chaos, not merely stochasticity due to noise, as opposed to the spatially restricted case.

We have found the threshold of the LIFT for the homeotropic state and the threshold of the secondary instability of the stationary distorted state in a nematic LC, including the dye-doped case, for different incidence angles of the light. In particular we have demonstrated that the stationary distorted state loses stability in an inhomogeneous Hopf bifurcation with some nonzero critical wavenumber that leads to the formation of travelling waves in the plane of the layer.

Our result that  $(q_c, p_c) \neq 0$  demonstrates a general feature of Hopf bifurcations in spatially extended systems with broken reflection symmetry, as is the case in the LIFT-distorted state. Except for special cases, like those where the reflection symmetry can be restored by going into a moving frame, the neutral surface exhibits the signature of the broken symmetry. Consequently, at  $q_c = p_c = 0$  the neutral surface does in general not have a stationary point, except maybe in special cases, like  $K_1 = K_2 = K_3$ . This general feature was apparently first noted in the context of reaction-diffusion systems [73, 74].

# Summary

I have presented in this thesis a theoretical study of some dynamical phenomena and orientational transitions induced by intense light in homeotropically oriented nematic layers. A large number of experiments has been performed in such systems and various interesting dynamical regimes have been identified. However, systematic theories capable of describing the observed phenomena have been derived for some cases only. In other cases oversimplified models exist with limited applicability.

In Chapter 2 I considered the case of a circularly polarized plane light wave incident perpendicularly on the layer. I have constructed a theory that is capable of describing the observed regimes of director motion and the transitions between them in detail [43, 46]. The first instability is the Fréedericksz transition from the homeotropic state to a small-amplitude reoriented state with uniform director precession around the layer normal. With increasing light intensity, this state destabilizes via a supercritical Hopf bifurcation and a new frequency in the time Fourier spectra of the dynamical variables appears. This regime is quasiperiodic and corresponds to a precession and nutation of the director. As the intensity increases further, this state disappears at a certain critical value where the period of nutation becomes infinite. There a strongly hysteretic transition to a state with large reorientation occurs via a homoclinic bifurcation. The homoclinic orbit involved is of the simplest type where a limit cycle collides with a saddle point having one unstable direction. The new state corresponds to a uniform precession of the director, however, with very large period and with large reorientation. I have also investigated the influence of an additional static electric field on the dynamical scenario described above.

In Chapter 3 the treatment is generalized to the case of elliptically polarized light. The complete bifurcation diagram with the light intensity and the ellipticity as control parameters has been calculated in the region where rotating states exist. I have shown [40] that for a fairly narrow region of ellipticities close to circular polarization the first periodic rotating state loses its stability in a supercritical Hopf bifurcation. I have found that with increasing light intensity at different ellipticities different sequences of transitions all finally lead to a state with large director distortion as the intensity is increased. The nature of this largely distorted state, as well as intermediate regimes vary with ellipticity. Some of the regimes that appear at lower intensities were studied

previously, both experimentally and theoretically, but a complete picture up to the largely distorted regime was missing.

In the theoretical treatments developed in the Chapters above, as in all other treatments, the velocity field induced by the director motion (backflow) has been neglected. In Chapter 4 I have investigated the influence of backflow on the dynamical scenario described in Chapter 2 and have shown that the backflow leads to substantial quantitative changes. It turns out that the regime of nonuniform precession shifts to higher light intensities and exists in a larger interval. I have also found unanticipated spatial oscillations of the backflow across the layer for the state with large director distortion [54]. This is a signature of the interference pattern of the light within the layer. Actually, in the theory presented, for the first time, a light-induced dynamical phenomenon has been derived from the full nematodynamic equations. Thus, for the first time, full quantitative comparison with experiments using a transversally extended laser light could be done.

Also, in all previous theoretical treatments involving plane wave incident light, it was assumed that the director distortion does not depend on the coordinates in the plane of the layer, i.e. one dealt with a one dimensional situation. In Chapter 5 I have studied the instabilities induced by a linearly polarized ordinary light wave incident at a small oblique angle allowing for spatial variations of the director in the plane of the layer and including the case of a dye-doped nematic. It was previously known that for sufficiently small angles of incidence the homeotropic state loses stability in a stationary, homogeneous pitchfork bifurcation. I have shown that the resulting stationary distorted state loses stability via a secondary Hopf bifurcation to spatially inhomogeneous state (nonzero critical wavenumber) that leads to the formation of travelling waves in the plane of the layer [55]. The wavelength of these waves depend on the angle of incidence and the ratios of the elastic constants. It is typically several times larger than the thickness of the layer.

In conclusion one can state that, while there now exist systematic theories which give qualitative predictions for experiments, quantitative agreement has not yet been achieved. The most important reason for this is probably that the beam width used in experiments is of the order of the thickness of the layer, whereas in the theoretical treatments an infinite plane wave is assumed. Thus, either the finite lateral extension of the laser should be included in the theory or transversally extended lasers have to be used in the experiments. The former is a difficult task, especially when flow is also included. For the latter extremely powerful lasers are needed, unless appropriately dye-doped nematic liquid crystals are used. Another interesting problem that could be approached in the future is the case when the light intensity is periodically modulated.

# Appendix A

## Representation of the light propagation in terms of ordinary and extraordinary waves

In this Appendix an approach where the light propagation is represented by means of ordinary and extraordinary light is presented. This representation is used for the perpendicular incidence ( $s_0 = 0$ ). In this case Eqs. (1.17) from the Introduction can be rewritten as follows:

$$\begin{pmatrix} \partial_z H_y \\ -\partial_z H_x \end{pmatrix} = ik_0 \mathbf{M} \begin{pmatrix} E_x \\ E_y \end{pmatrix}, \quad \begin{pmatrix} \partial_z E_x \\ -\partial_z E_y \end{pmatrix} = ik_0 \begin{pmatrix} H_y \\ -H_x \end{pmatrix}, \quad (\text{A.1})$$

where

$$\mathbf{M} = \begin{pmatrix} \varepsilon_{xx} - \frac{\varepsilon_{xz}^2}{\varepsilon_{zz}} & \varepsilon_{xy} - \frac{\varepsilon_{xz}\varepsilon_{yz}}{\varepsilon_{zz}} \\ \varepsilon_{xy} - \frac{\varepsilon_{xz}\varepsilon_{yz}}{\varepsilon_{zz}} & \varepsilon_{yy} - \frac{\varepsilon_{yz}^2}{\varepsilon_{zz}} \end{pmatrix}. \quad (\text{A.2})$$

We can easily derive the second-order ODE for the electric field (the wave equation) from Eqs. (A.1):

$$\frac{\partial^2 \mathbf{l}}{\partial z^2} = -k_0^2 \mathbf{M} \mathbf{l}, \quad (\text{A.3})$$

where

$$\mathbf{l} = \begin{pmatrix} E_x \\ E_y \end{pmatrix}. \quad (\text{A.4})$$

The  $z$  component of the electric field can be found from the following relation [see Eq. (1.16)]:

$$E_z = -\frac{\varepsilon_{xz}E_x + \varepsilon_{yz}E_y}{\varepsilon_{zz}}. \quad (\text{A.5})$$

We write the director in terms of the usual spherical angles  $\mathbf{n}=(\sin \Theta \cos \Phi, \sin \Theta \sin \Phi, \cos \Theta)$ . We then perform a transformation from the basis  $(\mathbf{e}_x, \mathbf{e}_y)$  into the local basis  $(\mathbf{e}_o, \mathbf{e}_e^\perp)$  where the matrix  $\mathbf{M}$  has diagonal form [75]. In this new coordinate system the field components are the amplitudes of the ordinary  $E_o$  and transversal part of the extraordinary  $E_e^\perp$  waves [note that  $\mathbf{E}_e^\perp = \mathbf{E}_e - (\mathbf{E}_e \mathbf{e}_z) \mathbf{e}_z$ ] in the  $(\mathbf{x}, \mathbf{y})$  plane, respectively, related to  $E_x, E_y$  as follows:

$$\boldsymbol{\psi} = \mathbf{O} \mathbf{l}, \quad (\text{A.6})$$

where

$$\mathbf{O} = \begin{pmatrix} -\sin \Phi & \cos \Phi \\ \cos \Phi & \sin \Phi \end{pmatrix} \quad \text{and} \quad \boldsymbol{\psi} = \begin{pmatrix} E_o \\ E_e^\perp \end{pmatrix}. \quad (\text{A.7})$$

The matrix  $\mathbf{O}$  represents the matrix describing rotation by the angle  $\Phi$  in the  $(\mathbf{x}, \mathbf{y})$  plane as is shown in Fig. A.1.

The transversal part of the electric field can be expressed in terms of the two bases as follows:

$$\mathbf{E}^\perp = E_x \mathbf{e}_x + E_y \mathbf{e}_y = E_e^\perp \mathbf{e}_e^\perp + E_o \mathbf{e}_o. \quad (\text{A.8})$$

Note that in each plane  $z = \text{const}$ , the electric fields  $\mathbf{E}_e, \mathbf{E}_o$  and the electric displacements  $\mathbf{D}_e$  and  $\mathbf{D}_o$  of the extraordinary and ordinary waves are directed as is depicted in Fig. A.2.

In the  $(\mathbf{e}_o, \mathbf{e}_e^\perp)$  representation the matrix  $\mathbf{M}$  has the following form:

$$\tilde{\mathbf{M}} = \mathbf{O} \mathbf{M} \mathbf{O}^{-1} = \begin{pmatrix} \lambda_o & 0 \\ 0 & \lambda_e \end{pmatrix}, \quad (\text{A.9})$$

where

$$\lambda_o = \varepsilon_\perp, \quad \lambda_e = \frac{\varepsilon_\perp(\varepsilon_a + \varepsilon_\perp)}{\varepsilon_\perp + \varepsilon_a \cos^2 \Theta}. \quad (\text{A.10})$$

Taking into account that  $\mathbf{l}$  is related to  $\boldsymbol{\psi}$  [see Eq. (A.6)] as

$$\mathbf{l} = \mathbf{O}^{-1} \boldsymbol{\psi} \quad (\text{A.11})$$

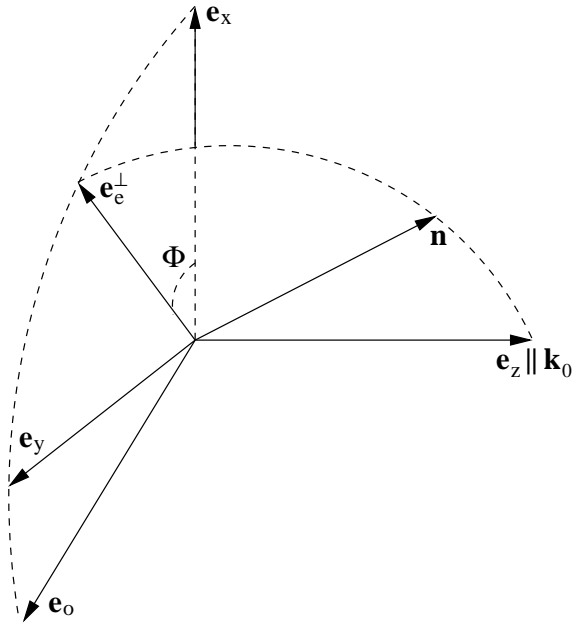


**Figure A.1.** Directions of the director  $\mathbf{n}$  and of the basis vectors  $\mathbf{e}_x$ ,  $\mathbf{e}_y$ ,  $\mathbf{e}_o$  and  $\mathbf{e}_e^\perp$ . The wave vector  $\mathbf{k}_0$  is directed along the propagation direction  $z$ .

and substituting this expression into Eq. (A.3) the following equation for  $\psi$  can be derived:

$$\partial_z^2 \psi = \partial_z^2 [\mathbf{O}] \mathbf{O}^{-1} \psi + 2\partial_z [\mathbf{O}] \partial_z [\mathbf{O}^{-1}] \psi + 2\partial_z [\mathbf{O}] \mathbf{O}^{-1} \partial_z \psi - k_0^2 \tilde{\mathbf{M}} \psi. \quad (\text{A.12})$$

Now we can use the fact that  $k_0 \gg 1/L$  and drop the first two terms on the r.h.s. of Eq. (A.12). On the other hand we have to keep the rest because when applying the  $z$  derivative on  $\psi$  the large factor  $k_0$  appears. Such an approximation corresponds to the Geometric Optics Approximation. Finally Eq. (A.12) reduces to:

$$\partial_z^2 \psi = 2\partial_z [\mathbf{O}] \mathbf{O}^{-1} \partial_z \psi - k_0^2 \tilde{\mathbf{M}} \psi. \quad (\text{A.13})$$

We look for solutions of Eq. (A.13) in the following form:

$$E_o = A_o(z) \mathbf{e}^{ik_0 \sqrt{\lambda_o} z}, \quad E_e^\perp = A_e(z) \mathbf{e}^{ik_0 \int_0^z dz' \sqrt{\lambda_e(z')}} , \quad (\text{A.14})$$

where  $A_o$ ,  $A_e$  are amplitudes that vary slowly with  $z$  on the scale  $k_0^{-1}$ . Straightforward calculations give from Eq. (A.13) the following equations for  $A_o$ ,  $A_e$ :

$$\begin{cases} \partial_z A_o = -(\partial_z \Phi) \sqrt{\frac{\lambda_e}{\lambda_o}} \mathbf{e}^{i\alpha(z)} A_e \\ \partial_z A_e = -\frac{(\partial_z \lambda_e) A_e}{4\lambda_e} + (\partial_z \Phi) \sqrt{\frac{\lambda_o}{\lambda_e}} \mathbf{e}^{-i\alpha(z)} A_o \end{cases} \quad (\text{A.15})$$

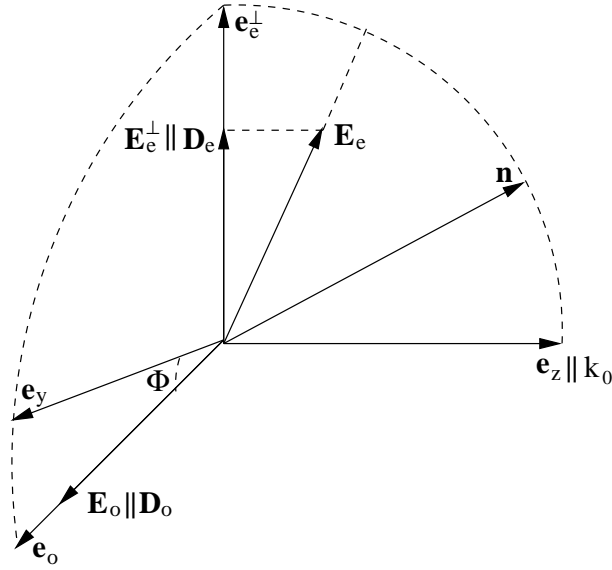


**Figure A.2.** Directions of the director  $\mathbf{n}$  and of the field  $\mathbf{E}_o$ ,  $\mathbf{D}_o$ ,  $\mathbf{E}_e$  and  $\mathbf{D}_e$ . The vectors  $\mathbf{E}_e$ ,  $\mathbf{D}_e$ ,  $\mathbf{n}$  and  $\mathbf{k}_0$  are coplanar.

where  $\alpha(z)$  is the phase delay between the ordinary and extraordinary waves induced by the nematic slice of a thickness  $z$  given as:

$$\alpha(z) = k_0 \int_0^z (\sqrt{\lambda_e} - \sqrt{\lambda_o}) dz. \quad (\text{A.16})$$

Without loss of generality, we may choose the  $x$  axis along the major axis of the polarization ellipse of the incident light. In this case the boundary conditions for the amplitudes  $A_o$ ,  $A_e$  at  $z = 0$  are given by:

$$\begin{aligned} |A_{o0}|^2 &= \frac{E_0^2}{2} (1 - \cos 2\Phi|_{z=0} \cos 2\chi), \quad |A_{e0}|^2 = \frac{E_0^2}{2} (1 + \cos 2\Phi|_{z=0} \cos 2\chi) \\ A_{e0} A_{o0}^* &= -\frac{E_0^2}{2} (\sin 2\Phi|_{z=0} \cos 2\chi + i \sin 2\chi), \end{aligned} \quad (\text{A.17})$$

where the ellipticity angle  $\chi$  ( $-\pi/4 \leq \chi \leq \pi/4$ ) [76] characterizes the polarization state of the incident light. The case  $\chi = 0$  [ $\chi = \pm\pi/4$ ] corresponds to linearly [circularly] polarized light while intermediate values refer to elliptical polarization. Since the sign of  $\chi$  determines the handedness of the polarization and hence the sense of rotation of the director around the  $z$ -axis, it is sufficient to consider only positive values of  $\chi$  related to the major  $b$  and minor  $a$  axis of the ellipse as:

$$\tan \chi = \frac{b}{a}. \quad (\text{A.18})$$

The following relations can be shown from Eqs. (A.6, A.14):

$$|E_x|^2 = \cos^2 \Phi |A_e|^2 - \sin 2\Phi \operatorname{Re} [A_e A_o^* e^{i\alpha(z)}] + \sin^2 \Phi |A_o|^2, \quad (\text{A.19})$$

$$|E_y|^2 = \cos^2 \Phi |A_o|^2 + \sin 2\Phi \operatorname{Re} [A_e A_o^* e^{i\alpha(z)}] + \sin^2 \Phi |A_e|^2$$

$$E_x E_y^* + E_x^* E_y = \sin 2\Phi (|A_e|^2 - |A_o|^2) + 2 \cos 2\Phi \operatorname{Re} [A_e A_o^* e^{-i\alpha(z)}] .$$



# Appendix B

## Director equations in $(\theta, \varphi)$ representation

We substitute the director from (5.1) into Eqs. (1.6,1.7) to derive a set of two PDEs for  $\theta, \varphi$ . The equation derived from Eq. (1.6) contains the time derivative on  $\theta$  only:

$$\begin{aligned} \gamma_1 \partial_t \theta &= \frac{(K_1 - K_3)}{2} \sin 2\theta \cos^2 \varphi (\partial_z \theta)^2 + \sin 2\varphi (K_2 - K_1 + (K_1 - K_3) \cos^2 \theta) \partial_z \varphi \partial_z \theta - \\ &\frac{\sin 2\theta}{2} [(K_2 - K_1 + 2(K_2 - K_3) \cos^2 \theta) \cos^2 \varphi - K_2] (\partial_z \varphi)^2 - \\ &[(K_2 - K_1 + (K_1 - K_3) \cos^2 \theta) \cos^2 \varphi - K_2] \partial_z^2 \theta + \frac{K_1 - K_2}{4} \sin 2\theta \sin 2\varphi \partial_z^2 \varphi \quad (\text{B.1}) \\ &+ \frac{\xi_{eff}}{16\pi} \left\{ \sin 2\theta [E_x E_x^* - E_z E_z^* - \frac{\sin 2\varphi}{2} (E_y^* E_z + E_y E_z^*)] + \right. \\ &\left. \cos 2\theta [\sin \varphi (E_x^* E_y + E_x E_y^*) + (E_x^* E_z + E_x E_z^*) \cos \varphi] - \sin 2\theta \sin^2 \varphi (E_y E_y^* - E_z E_z^*) \right\} \end{aligned}$$

Multiplying Eq. (1.6) by  $\sin \theta \sin \varphi$  and Eq. (1.7) by  $\cos \theta$  and adding them the PDE for  $\varphi$  can be derived:

$$\begin{aligned}
\gamma_1 \cos^2 \theta \partial_t \varphi &= \frac{\sin 2\varphi}{2} \cos^2 \theta [(K_1 + K_3 - 2K_2)(\partial_z \theta)^2 + (K_1 - K_2 + (K_2 - K_3) \cos^2 \theta)(\partial_z \varphi)^2] + \\
&\sin 2\theta [(K_1 - K_2 + 2(K_2 - K_3) \cos^2 \theta) \cos^2 \varphi - K_1] \partial_z \varphi \partial_z \theta + (K_1 - K_2) \frac{\sin 2\varphi}{4} \sin 2\theta \partial_z^2 \theta - \\
&\cos^2 \theta [(K_1 - K_2 + (K_2 - K_3) \cos^2 \theta) \cos^2 \varphi - K_1] \partial_z^2 \varphi \tag{B.2} \\
&+ \frac{\xi_{eff}}{16\pi} \left\{ \frac{\sin 2\theta}{2} [\cos \varphi (E_x^* E_y + E_x E_y^*) - \sin \varphi (E_x^* E_z + E_x E_z^*)] + \cos^2 \theta [\cos 2\varphi (E_y^* E_z + E_y E_z^*) + \right. \\
&\left. \sin 2\varphi (E_y E_y^* - E_z E_z^*) \right\}
\end{aligned}$$

# Appendix C

## Matrix elements $\Lambda_{ij}$ for the linear stability analysis of the basic state

We can split the matrix elements  $\Lambda_{ij}$  introduced in Eqs. (5.19) into two parts

$$\Lambda_{ij} = \Lambda_{ij}^{pure} + \Lambda_{ij}^{abs}, \quad i, j = 1, 2,$$

where  $\Lambda_{ij}^{pure}$  do not depend on absorption and thus describe the case of a pure LC without dye doping and  $\Lambda_{ij}^{abs}$  that is due to absorption effect only. Introducing  $\beta = k_{Im}L$  [see Eq. (5.4)] and keeping in  $\Lambda_{ij}^{abs}$  the linear terms in  $\gamma_a, \gamma_{\perp}$  only the following relations can be proved:

$$\begin{aligned} \Lambda_{11}^{pure} &= -1 + \frac{\rho}{1 - \kappa^2} \left[ 1 - \frac{2\kappa \sin \pi \kappa}{\pi(1 - \kappa^2)} \right], \quad \Lambda_{12}^{pure} = -\frac{4\rho \kappa \sin \pi \kappa}{\pi(4 - \kappa^2)(1 - \kappa^2)} \\ \Lambda_{22}^{pure} &= -4 + \frac{4\rho}{4 - \kappa^2} \left[ 1 + \frac{2\kappa \sin \pi \kappa}{\pi(4 - \kappa^2)} \right], \quad \Lambda_{21}^{pure} = -\Lambda_{12}^{pure} \\ \Lambda_{11}^{abs} &= \frac{\rho}{\pi^2(1 - \kappa^2)^3} \left\{ 2\pi(1 - \kappa^2)(2\beta + \pi\xi\kappa)\kappa \sin \pi \kappa + 2\kappa(1 + \cos \pi \kappa) \times \right. \\ &\quad \left. [\pi\psi(1 - \kappa^2) - 4\kappa(\beta + \pi\xi\kappa)] - \pi^2\beta(1 - \kappa^2)^2 \right\} \\ \Lambda_{22}^{abs} &= -\frac{4\rho}{\pi^2(4 - \kappa^2)^3} \left\{ 2\pi(4 - \kappa^2)(2\beta + \pi\xi\kappa)\kappa \sin \pi \kappa - 2\kappa(1 - \cos \pi \kappa) \times \right. \\ &\quad \left. [\pi\psi(4 - \kappa^2) - 4\kappa(\beta + \pi\xi\kappa)] + \pi^2\beta(4 - \kappa^2)^2 \right\} \end{aligned} \quad (C.1)$$

$$\Lambda_{12}^{abs} = \frac{4\rho\kappa(2\beta + \pi\xi\kappa) \sin \pi\kappa}{\pi(4 - \kappa^2)(1 - \kappa^2)} + \frac{4\rho}{9\pi^2(4 - \kappa^2)^2(1 - \kappa^2)^2} \left\{ 9\kappa[\pi(\psi + 4\xi)\kappa^4 + 4\kappa^3\beta \right. \\ \left. - 5\pi(\psi + 2\xi)\kappa^2 - 16\kappa\beta + 4\pi\psi] \cos \pi\kappa - 6\pi(\psi + 2\xi)\kappa^7 - 32\beta\kappa^6 + \right. \\ \left. 15\pi(3\psi + 4\xi)\kappa^5 + 228\beta\kappa^4 - 3\pi(33\psi + 34\xi)\kappa^3 - 432\beta\kappa^2 + 60\pi\psi\kappa + 128\beta \right\} \quad (C.2)$$

$$\Lambda_{21}^{abs} = -\Lambda_{12}^{abs} - \frac{16\beta\rho(27\kappa^2 \cos \pi\kappa + 10\kappa^6 - 84\kappa^4 + 165\kappa^2 - 64)}{9\pi^2(4 - \kappa^2)^2(1 - \kappa^2)^2}.$$

To derive an approximate value for the Takens-Bogdanov point where  $\det(\Lambda) = Tr(\Lambda) = 0$  we may perform an expansion of  $\Lambda_{ij}$  with respect to  $\kappa$  using the fact that  $\kappa^4 \ll 1$ . Eventually one finds for the Takens-Bogdanov point  $(\kappa_{TB}, \rho_{TB})$ :

$$\left[ \frac{13}{8}\pi^2 + 5\beta \left( \frac{116}{9} - \frac{11\pi^2}{8} \right) \right] \kappa_{TB}^4 - \frac{545}{9}\pi\psi\kappa_{TB}^3 + [19\pi^2 - \beta(25\pi^2 - 160)]\kappa_{TB}^2 - \\ 40\pi\psi\kappa_{TB} - 6\pi^2 = 0, \quad (C.3)$$

$$\rho_{TB} = \frac{20}{8 - \kappa_{TB}^2} \left[ 1 - \frac{16\psi\kappa_{TB}}{\pi(8 - \kappa_{TB}^2)} - \frac{(\kappa_{TB}^2(7\pi^2 - 64) - 8\pi^2)\beta}{\pi^2(8 - \kappa_{TB}^2)} \right].$$

## Appendix D

# Matrix representation for the light propagation (Oldano formalism)

We can split  $D$  (see (1.19)) describing the light propagation in the medium into two parts:  $D = D_0 + D_z(z)$ .  $D_0$  does not depend on  $z$  and refers to the basic state (without reorientation) and  $D_z$  contains the rest. The matrices  $D_0, D_z(z)$  are given by [using the expression (1.11) for the dielectric tensor]:

$$D_0 = \begin{pmatrix} 0 & 1 - \frac{s_0^2}{e_\perp + e_a} & 0 & 0 \\ e_\perp & 0 & 0 & 0 \\ 0 & 0 & 0 & 1 \\ 0 & 0 & e_\perp - s_0^2 & 0 \end{pmatrix} \quad (D.1)$$

and

$$D_z = \frac{1}{e_\perp + e_a n_z^2} \begin{pmatrix} -e_a n_x n_z s_0 & -\frac{e_a(1 - n_z^2)s_0^2}{e_a + e_\perp} & -e_a n_y n_z s_0 & 0 \\ e_a e_\perp n_x^2 & -e_a n_x n_z s_0 & e_a e_\perp n_x n_y & 0 \\ 0 & 0 & 0 & 0 \\ e_a e_\perp n_x n_y & -e_a n_y n_z s_0 & e_a e_\perp n_y^2 & 0 \end{pmatrix}, \quad (D.2)$$

where  $e_a = \varepsilon_a + i\gamma_a$  and  $e_\perp = \varepsilon_\perp + i\gamma_\perp$ .

Note that  $D_z$  vanishes if  $\mathbf{n} = (0, 0, 1)$ . We have the following relations between the matrix elements:  $(D_z)_{11} = (D_z)_{22}$ ,  $(D_z)_{23} = (D_z)_{41}$  and  $(D_z)_{13} = (D_z)_{42}$ .

We may substitute the representation of the director (5.1) to get an expression for  $D_z$  in terms of the angles.

It is convenient to introduce a representation in terms of eigenfunctions of  $D_0$ . The eigenvalue problem

$$D_0 \bar{\alpha}_i = a_i \bar{\alpha}_i \quad (D.3)$$

is solved by the eigenvalues

$$\begin{aligned} a_2 = -a_1 &= \sqrt{e_\perp - s_0^2}, \\ a_4 = -a_3 &= \sqrt{\frac{(e_\perp + e_a - s_0^2)e_\perp}{e_\perp + e_a}} \end{aligned} \quad (D.4)$$

and eigenvectors

$$\bar{\alpha}_{1,2} = \begin{pmatrix} 0 \\ 0 \\ \mp \frac{1}{a_2} \\ 1 \end{pmatrix}, \quad \bar{\alpha}_{3,4} = \begin{pmatrix} \mp \frac{a_4}{e_\perp} \\ 1 \\ 0 \\ 0 \end{pmatrix}. \quad (D.5)$$

We introduce the metric tensor

$$\mathbf{M} = \begin{pmatrix} 0 & 1 & 0 & 0 \\ 1 & 0 & 0 & 0 \\ 0 & 0 & 0 & 1 \\ 0 & 0 & 1 & 0 \end{pmatrix} \quad (D.6)$$

to define a scalar product between these vectors. With such a scalar product the eigenvectors are orthogonal to one another:

$$\bar{\alpha}_i^T \mathbf{M} \bar{\alpha}_j = \delta_{ij} N_i, \quad (D.7)$$

where  $N_i$  is the "norm" of vector  $\bar{\alpha}_i$ . One has:

$$N_{1,2} = \mp \frac{2}{\sqrt{e_\perp - s_0^2}}, \quad N_{3,4} = \mp 2 \sqrt{\frac{e_\perp + e_a - s_0^2}{e_\perp(e_\perp + e_a)}}, \quad (D.8)$$

The matrix  $D_0$  is expressed by means of the vectors  $\bar{\alpha}_i$  as:

$$D_0 = \sum_i \frac{a_i}{N_i} \bar{\alpha}_i \bar{\alpha}_i^T M. \quad (D.9)$$

The four vectors  $\bar{\alpha}_i$  give the polarization of four "proper" waves that propagate inside the layer without changing their state of polarization in the case of homeotropic alignment. The eigenvalues of  $a_i$  give the indices of refraction of these waves. Two of these vectors  $\bar{\alpha}_1$  ( $\bar{\alpha}_2$ ) correspond to backward (forward) propagating ordinary waves and the other two  $\bar{\alpha}_3$  ( $\bar{\alpha}_4$ ) correspond to backward (forward) propagating extraordinary waves. The contribution of the backward waves ( $\bar{\alpha}_1$  and  $\bar{\alpha}_3$ ) is negligibly small because the dielectric properties of the nematic change slowly on the spatial scale of the wavelength.

Thus we may expand  $\bar{\Psi}(z)$  as follows:

$$\bar{\Psi}(z) = b_2(z) e^{ik_0 a_2 z} \bar{\alpha}_2 + b_4(z) e^{ik_0 a_4 z} \bar{\alpha}_4. \quad (D.10)$$

Substituting (D.10) into Eq. (1.17) and multiplying the right and left hand sides by  $M \bar{\alpha}_k^T$  [taking into account the normalization condition (D.7)] the following equations for  $b_2$  and  $b_4$  can be derived:

$$\frac{db_k}{dz} = \frac{ik_0}{N_k} \sum_{j=2,4} P_{kj}(z) b_j e^{-ik_0(a_k - a_j)z}, \quad k = 2, 4, \quad (D.11)$$

where the matrix elements of  $D_z$  with respect to the eigenvectors  $\bar{\alpha}_2$  and  $\bar{\alpha}_4$

$$P_{kj}(z) = \bar{\alpha}_k^T M D_z(z) \bar{\alpha}_j \quad (D.12)$$

are given by:

$$\begin{aligned} P_{24} &= P_{42} = \frac{e_a n_y (a_4 n_x - s_0 n_z)}{a_2 (e_{\perp} + e_a n_z^2)}, \quad P_{22} = \frac{e_a e_{\perp} n_y^2}{a_2^2 (e_{\perp} + e_a n_z^2)}, \\ P_{44} &= \frac{e_a n_x a_4 (a_4 n_x - 2s_0 n_z)}{e_{\perp} (e_{\perp} + e_a n_z^2)} - \frac{e_a s_0^2 (1 - n_z^2)}{(e_a + e_{\perp}) (e_{\perp} + e_a n_z^2)}. \end{aligned} \quad (D.13)$$

From the definition of  $\bar{\Psi}(z)$ , Eq. (1.18), together with (D.10) and (1.16) the following relations can then be easily shown:

$$\begin{aligned} E_x &= \frac{b_4(z) a_4}{e_{\perp}} e^{ik_0 a_4 z}, \quad E_y = \frac{b_2(z)}{a_2} e^{ik_0 a_2 z}, \\ E_z &= -\frac{1}{\varepsilon_{zz}} \left( \left[ \frac{s_0 e_{\perp}}{a_4} + \varepsilon_{xz} \right] E_x + \varepsilon_{yz} E_y \right). \end{aligned} \quad (D.14)$$



# Bibliography

- [1] N. V. Tabiryan, A. V. Sukhov, and B. Y. Zel'dovich, *Mol. Cryst. Liquid Cryst.* **136**, 1 (1985).
- [2] F. Simoni, *Nonlinear optical properties of liquid crystals* (World Scientific, Singapore, 1997).
- [3] E. Santamato, B. Daino, M. Romagnoli, M. Settembre, and Y.R. Shen, *Phys. Rev. Lett.* **57**, 2423 (1986).
- [4] E. Santamato, M. Romagnoli, M. Settembre, B. Daino, and Y.R. Shen, *Phys. Rev. Lett.* **61**, 113 (1988).
- [5] L. Marrucci, G. Abbate, S. Ferraiuolo, P. Maddalena, and E.Santamato, *Phys. Rev. A* **46**, 4859 (1992).
- [6] R. A. Beth, *Phys. Rev.* **50**, 115 (1936).
- [7] J. D. Jackson, *Classical electrodynamics* (Wiley, New York, 1962).
- [8] L. Allen, M. W. Beijersbergen, R. J. C. Spreeuw, and J. P. Woerdmann, *Phys. Rev. A* **45**, 8185 (1992).
- [9] E. Brasselet, B. Doyon, T.V. Galstian and L. J. Dube, *Phys. Rev. E* **69**, 021701 (2004).
- [10] A. Vella, A. Setaro, B. Piccirillo, and E. Santamato, *Phys. Rev. E* **67**, 051704 (2003).
- [11] B. Piccirillo, A. Vella, and E. Santamato, *Phys. Rev. E* **69**, 021702 (2004).
- [12] E. Brasselet, B. Doyon, T.V. Galstian and L. J. Dube, *Phys. Lett. A* **299**, 212 (2002).

- [13] E. Brasselet, B. Doyon, T.V. Galstian and L. J. Dube, Phys. Rev. E **67**, 031706 (2003).
- [14] E. Santamato, G. Abbate, P. Maddalena, L. Marrucci and Y. R. Shen, Phys. Rev. Lett. **64**, 1377 (1990).
- [15] A. Vella, B. Piccirillo, and E. Santamato, Phys. Rev. E **65**, 031706 (2002).
- [16] A. Buka and L. Kramer, *Pattern formation in liquid crystals* (Springer, Berlin, 1995).
- [17] I. Janossy, A. Lloyd, and B. S. Wherrett, Mol. Cryst. Liq. Cryst. **179**, 1 (1990).
- [18] I. Janossy and T. Kosa, Mol. Cryst. Liq. Cryst. **207**, 189 (1991).
- [19] I. Janossy, J. Nonlin. Opt. Phys. Mat. **8**, 361 (1999).
- [20] I. Janossy and A. Lloyd, Mol. Cryst. Liq. Cryst. **203**, 77 (1991).
- [21] I. Janossy, Phys. Rev. E **49**, 2957 (1994).
- [22] L. Marrucci, D. Paparo, P. Maddalena, E. Massera, E. Prudnikova and E. Santamato, J. Chem. Phys. **107**, 9783 (1997).
- [23] A. S. Zolot'ko, V. F. Kitaeva, N. Kroo, N. N. Sobolev, A. P. Sukhorukov, and L. Czillag, Sov. Phys. JETP **32**, 158 (1980).
- [24] S. D. Durbin, S. M. Arakelian, and Y. R. Shen, Opt. Lett. **6**, 411 (1981).
- [25] A. S. Zolot'ko, V. F. Kitaeva, N. Kroo, N. N. Sobolev, A. P. Sukhorukov, V. A. Troshkin and L. Czillag, Sov. Phys. JETP **60**, 488 (1984).
- [26] V. F. Kitaeva, N. Kroo, N. N. Sobolev, A. P. Sukhorukov, V. Yu. Fedorovich and L. Czillag, Sov. Phys. JETP **62**, 520 (1985).
- [27] G. Cipparrone, V. Carbone, C. Versace, C. Umeton, R. Bartolino and F. Simoni, Phys. Rev. E **47**, 3741 (1993).
- [28] V. Carbone, G. Cipparrone, C. Versace, C. Umeton and R. Bartolino, Mol. Cryst. Liq. Cryst. Sci. Technol., Sec A **251**, 167 (1994).
- [29] V. Carbone, G. Cipparrone, C. Versace, C. Umeton and R. Bartolino, Phys. Rev. E **54**, 6948 (1996).

- 
- [30] C. Versace, V. Carbone, G. Cipparrone, C. Umeton and R. Bartolino, *Mol. Cryst. Liq. Cryst. Sci. Technol., Sec A* **290**, 267 (1996).
- [31] A. S. Zolot'ko, V. F. Kitaeva, N. N. Sobolev, V. Y. Fedorovich, A. P. Sukhorukov, N. Kroo, and L. Csillag, *Liq. Cryst.* **15**, 787 (1993).
- [32] V. Carbone, G. Cipparrone, and G. Russo, *Opt. Commun.* **173**, 1 (2000).
- [33] G. Demeter and L. Kramer, *Phys. Rev. Lett.* **83**, 4744 (1999).
- [34] G. Demeter, *Phys. Rev. E* **61**, 6678 (2000).
- [35] G. Russo, V. Carbone, and G. Cipparrone, *Phys. Rev. E* **62**, 5036 (2000).
- [36] V. Carbone, G. Cipparrone, and G. Russo, *Phys. Rev. E* **63**, 051701 (2001).
- [37] P. G. de Gennes and J. Prost, *The physics of liquid crystals* (Clarendon press, Oxford, 1993).
- [38] D. W. Berreman, *J. Opt. Soc. Am.* **62**, 502 (1972).
- [39] M. Abramowitz and I. A. Stegun, *Handbook of Mathematical Functions* (Dover, New York, 1970).
- [40] D. O. Krimer and L. Kramer; E. Brasselet, T.V. Galstian and L. J. Dube, submitted to *J. Opt. Soc. Am. B* (2004).
- [41] L. Marrucci, D. Paparo, M. R. Vetrano, M. Colicchio, E. Santamato and G. Viscardi, *J. Chem. Phys.* **113**, 10361 (2000).
- [42] G. Cipparrone, D. Duca, C. Versace, C. Umeton and N. V. Tabiryan, *Mol. Cryst. Liq. Cryst.* **266**, 263 (1995).
- [43] E. Brasselet, T.V. Galstian and L. J. Dube; D. O. Krimer and L. Kramer, submitted to *J. Opt. Soc. Am. B* (2004).
- [44] E. Brasselet and T. Galstian, *Opt. Commun.* **186**, 291 (2000).
- [45] I. C. Khoo, T. H. Liu, and P. Y. Yan, *J. Opt. Soc. Am. B* **4**, 115 (1987).
- [46] D. O. Krimer, G. Demeter, and L. Kramer, *MCLC in press*, (2004).
- [47] P. Glendinning, *Stability, instability and chaos* (Cambridge University press, Cambridge, 1996).
- [48] H. J. Deuling, *Mol. Cryst. Liq. Cryst.* **19**, 123 (1972).

- [49] A. Barone and G. Patern, *Physics and applications of the Josephson effect* (Wiley, New York, 1982).
- [50] P. L. Garcia-Ybarra, J. C. Antoranz, V. Sankovitch, and J. L. Castillo, *Phys. Rev. E* **49**, 5225 (1994).
- [51] J. von Stamm, U. Gerdt, Th. Buzug, and G. Pfister, *Phys. Rev. E* **54**, 4938 (1996).
- [52] L. P. Shil'nikov, *Math. USSR Sb.* **6**, 443 (1963).
- [53] T. Peacock and T. Mullin, *J. Fluid Mech.* **432**, 369 (2001).
- [54] D. O. Krimer, G. Demeter, and L. Kramer, to be published .
- [55] D. O. Krimer, G. Demeter, and L. Kramer, *Phys. Rev. E* **66**, 031707 (2002).
- [56] B. Y. Zel'dovich and N. Tabiryan, *Sov. Phys. JETP* **55**, 656 (1982).
- [57] J. L. Ericksen, *Arch. Ration. Mech. Analysis* **4**, 231 (1960).
- [58] F. M. Leslie, *Quart. J. Mech. Appl. Math.* **19**, 357 (1966).
- [59] M. Treiber, Ph.D. thesis, Bayreuth, 1996.
- [60] O. Parodi, *J. Phys. (Paris)* **31**, 581 (1970).
- [61] E. Guyon, R. Meyer, and J. Salan, *Mol. Cryst. Liquid Cryst.* **54**, 261 (1979).
- [62] D. W. Berreman, *J. Appl. Phys.* **46**, 3746 (1975).
- [63] C. Z. van Doorn, *J. Phys. (France)* **36 C1**, 261 (1975).
- [64] C. Z. van Doorn, *J. Appl. Phys.* **46**, 3738 (1975).
- [65] N. J. Smith, M. D. Tillin, and J. R. Sambles, *Phys. Rev. Lett.* **88**, 088301 (2002).
- [66] S. A. Jewell and J. R. Sambles, *Appl. Phys. Lett.* **84**, 46 (2004).
- [67] B. L. Winkler, H. Richter, I. Rehberg, W. Zimmermann, L. Kramer and A. Buka, *Phys. Rev. A* **43**, 1940 (1991).
- [68] N.V. Tabiryan, A.L. Tabiryan-Murazyan, V. Carbone, G. Cipparrone, C. Umeton, C. Versace and T. Tschudi, *Optics Comm.* **154**, 70 (1998).
- [69] C. Oldano, *Phys. Rev. A* **40**, 6014 (1989).

- [70] G. Demeter and L. Kramer, Phys. Rev. E **64**, 020701 (2001).
- [71] P. Couillet, E. Risler, and N. Vandenberghe, J. Stat. Phys. **101**, 521 (2000).
- [72] M. Argentina, P. Couillet, and E. Risler, Phys. Rev. Lett **86**, 807 (2001).
- [73] A. B. Rovinsky and M. Menzinger, Phys. Rev. Lett. **69**, 1193 (1991).
- [74] A. B. Rovinsky and M. Menzinger, Phys. Rev. Lett. **70**, 778 (1993).
- [75] E. Santamato and Y. R. Shen, J. Opt. Soc. Am. A **4**, 356 (1987).
- [76] C. Brosseau, *Fundamentals of polarized light: a statistical optics approach* (Wiley, New York, 1998).



# Acknowledgments

First of all I would like to express my special thanks to my supervisor Professor Lorenz Kramer who has instructed me during my research work. He not only advised me in an extremely helpful manner but also took the trouble to teach me spending a lot of his time. Moreover he has always given me the freedom to make the final decision about the direction to go. I am also very grateful for getting a chance to participate in different international meetings.

I would like to express my gratitude to Gabor Demeter who was actually my second supervisor and coauthor. I am grateful for stimulating discussions of different problems and an effective collaboration during my research. It was really nice to work with him.

I would like to thank my coauthor Etienne Brasselet for informing me of his newest experimental results continuously and for supplying the experimental figures for Chapters 2, 3.

Thanks to Aleksei Krekhov who helped me to adapt to the local atmosphere when I came for the first time to Bayreuth a couple of years ago. He is also credited with helping me to solve some technical problems during my work.

Finally I would like to say thanks to my colleagues Ildar Nassiboullaev and Pavel Akimov for helping me to solve some annoying problems with TEX when writing the manuscript.

Last but certainly not least I would like to express gratitude to my wife Oksana Krimer who always supported me and created a very warm atmosphere at home when I was doing my work and writing this thesis.